Title
Learning from Nature: An investigation of an impact-resistant system on the woodpecker head as a non-traumatic brain injury animal model

Author
Jung, Jae-Young

Publication Date
2019

Peer reviewed|Thesis/dissertation

UNIVERSITY OF CALIFORNIA SAN DIEGO

Learning from Nature: An investigation of an impact-resistant system on the woodpecker head as a non-traumatic brain injury animal model

A dissertation submitted in partial satisfaction of the
requirements for the degree of Doctor of Philosophy

in

Materials Science and Engineering with a Specialization in Multi-scale Biology

by

Jae-Young Jung

Committee in charge:

Professor Joanna McKittrick, Chair
Professor Shengqiang Cai
Professor Mark Ellisman
Professor David Kisailus
Professor Robert Sah

2019

The Dissertation of Jae-Young Jung is approved, and is acceptable in quality and form for publication on microfilm and electronically:

Chair

University of California San Diego

2019

TABLE OF CONTENTS

SIGNATURE PAGE iii

TABLE OF CONTENTS iv

LIST OF FIGURES viii

LIST OF TABLES xii

ACKNOWLEDGEMENTS xiii

VITA xvii

ABSTRACT OF DISSERTATION xxiii

CHAPTER 1: INTRODUCTION 1

1.1 Impact-resistant biological materials 1

1.1.1 Basic principles of impact mechanics and its associated variables 4

1.1.2 Fracture toughness and work of fracture of a material 4

1.1.3 Representative organisms and tissues of impact-resistant biological materials 8

1.1.4 Mineralized vs. non-mineralized materials 8

1.1.5 Offensive vs. defensive 9

1.1.6 Active vs. passive 10

1.2 Mollusk shells (abalone shell: nacre) 11

1.3 The dactyl club of a mantis shrimp 13

1.4 Bone and antlers 15

1.5 Teeth 16

1.6 Wood 18

1.7 Horns and hooves of tetrapod mammals (keratin) 20

CHAPTER 2: THE WOODPECKER HEAD 23

2.1 Introduction 23

2.2 Multi-scale hierarchical structure 25

2.3 Multi-phase of materials 26

2.4 Multi-properties: mechanical impedance mismatch 28

CHAPTER 3: STRUCTURAL ANALYSIS OF THE TONGUE AND HYOID APPARATUS IN A WOODPECKER 30

3.1 Introduction 30

3.2.1 Sample collection and preparation 35

3.2.2 X-ray Micro-computed tomography (μ-CT) and three-dimensional reconstruction 35

3.2.3 Microscopic evaluation and chemical composition 36

3.2.4 Nanoindentation 38

3.2.5 Statistical analysis 39

3.3 Results and Discussion 40

3.3.1 Macroscale structure 40

3.3.2 Microscale structure 42

3.3.3 Nanoindentation 52

3.4 Structure-Mechanical Properties Relationship 57

3.5 Conclusions 60

CHAPTER 4: A COMPARATIVE ANALYSIS OF THE AVIAN SKULL: WOODPECKERS AND CHICKENS 61

4.1 Introduction.. 61

4.2 Materials and Methods 63

4.2.1 Sample collection and preparation.. 63

4.2.2 Micro-computed tomography (μ-CT)... 64

4.2.3 Microstructure and chemical composition.. 65

4.2.4 Mechanical characterization by nanoindentation.. 66

4.3 Results and Discussions.. 66

4.3.1 Macroscale structure 66

4.3.2 Microscale structure.. 69

4.3.3 Microstructure and chemical composition.. 74

4.3.4 Mechanical properties... 76

4.4 Conclusions... 79

CHAPTER 5: A NATURAL STRESS DEFLECTOR ON THE HEAD? MECHANICAL AND FUNCTIONAL EVALUATION OF THE WOODPECKER SKULL BONES 82

5.1 Introduction... 82

5.2 Experimental and computational approach 85

5.3 Results and Discussions.. 91

5.4 Conclusions... 99

5.5 Future work.. 101

5.6 Experimental Section... 102

5.7 Supporting Information 104

5.7.1 Some suggested evolutionized structural and skeletal features on woodpeckers . 104

5.7.2 Previous studies of biomechanical analysis of the woodpecker’s pecking........... 105

5.7.3 The effect of the frontal overhang on vibration from the impact testing.............. 107

5.7.4 A time-lapse high-speed camera analysis of impact testing and natural frequency calculation.. 108

5.7.5 The effect of the frontal overhang on von Mises stress and in-plane principal stress from the FEA simulation 110

5.7.6 Experimental materials and methods 112

CHAPTER 6: SUMMARY.. 119

6.1 Motivation and hypothesis.. 119

6.2 Summary... 119

CHAPTER 7: BIOINSPIRED DESIGNS AND APPLICATIONS 122

CHAPTER 8: FUTURE DIRECTION 126

8.1 As an impact-resistant material and structures 126

8.2 As a testing system on the brain injury to replace current animal injury models......... 127

REFERENCES 129

LIST OF FIGURES

Figure 1.1. (A) Effect of mineralization on the work of fracture (WOF) and bending strength. (B) Property and structural gradients across antler, tooth, horn, and hoof. Images taken from [4]...... 2

Figure 1.2. Diagram of the eight most common biological structural design elements, taken from [5]. 3

Figure 1.3. A plot of fracture toughness over the Young's modulus of natural and synthetic materials [15]. 5

Figure 1.4. Representative organisms and tissues known to be impact-resistant biological materials. (A) Smashing of a mantis shrimp with its dactyl club on a crustacean shell [31], (B) bighorn sheep horns [32], (C) horse hooves [33], and (D) woodpecker head [34]. 8

Figure 1.5. A hierarchical structure of abalone shell as a representative example of the mollusk shells, taken from [69]. The mesolayers (left bottom) showed a tablet pullout toughening mechanism as following with the growth layers (middle), which are combined by mineral bridges (top right) and chitin fibril network (bottom right). 13

Figure 1.6. Peacock mantis shrimp use a pair of large raptorial appendages (A, white arrow) to strike hard objects with such high speeds that cavitation bubbles form between the appendage and striking surface, taken from [20] . (B–I) The dactyl heel (h) of the raptorial appendage strikes a snail (s) that is loosely wired to a stick. Images recorded at 0.2 ms intervals. Scale bar, 1 cm.. . 14

Figure 1.7. Hierarchical structure of antlers. Antlers are composed of compact bone as the outer layer and cancellous (trabecular or spongy) bone in the interior. The compact bone consists of osteons, which are concentric lamellae surrounding a central blood vessel. Each lamella has oriented type I collagen fibrils with a mineral (carbonated apatite) interspersed between 15

Figure 1.8. A schematic illustration of the human teeth structure, taken from [80]. 17

Figure 1.9. Various applications of impact resistant wood. (a) Louisville Slugger made of white ash [94], (b) USS Constitution ("Old Ironsides") made of white and southern live oak [95], (c) Degtyaryov hand-held machine gun stock made of walnut [96], (d) bowling alley flooring made of pine [97], (e) Ancient Greek trireme made of cedar [98]. 20

Figure 1.10. Hierarchical structure comparison of horn and hoof: (a) Hierarchical structure of horn from macro- to nano-structure. Tubular and laminated structure is showed in the micro- scale; (b) Tubules and intertubular materials in hoof wall. Keratinized cell arrangement changing from tubular to intertubular matrix. 21

Figure 2.1. The beaks of woodpeckers. (a) Photos of the upper and lower beaks of a male red-bellied woodpecker and (b) a schematic of the transverse cross-sectional view, adapted from [110]. 24

Figure 2.2. Examples of multi-scale hierarchical bone structures of the woodpecker head. (a-c) The skull bone of a great-spotted woodpecker adapted from [109, 119], (d-h) the beak bone of a

red-bellied woodpecker adapted from [41], and (i and j) the hyoid bone of a woodpecker adapted from [117] and [120]. 25

Figure 2.3. Mechanical properties of the woodpecker head. (a) Reduced elastic modulus of the lower beak rhamphotheca at different locations, adapted from [110]. (b) A comparison between the peak stress curve of viscoelastic bar model from a simplified finite element analysis (left) and the measured Young's moduli along the different locations (right, numbered). 29

Figure 3.1. Bones in the bird hyoid apparatus. (a) Photograph (dorsal view) of the hyoid bones of a domestic chicken (*Gallus gallus*). Taken from [51]. (b) Schematic diagram of the dorsal view showing the paraglossal, the basihyal, the urohyal bone, and the paired ceratobranchial and epibranchial bones in a domestic chicken. Adapted from [3]. 32

Figure 3.2. (a) Photograph of an acorn woodpecker. (b) The dissected hyoid apparatus. (c) The dried and sectioned samples of the hyoid apparatus in transverse and longitudinal planes. Magnified photographs of the three joint locations in the hyoid apparatus between (d) the lingual apex and body, (e) the lingual body and root, and (f) the lingual root and the hyoid horn. 40

Figure 3.3. Micro-computed tomography images of the head structure of an acorn woodpecker at different orientations. (a) Left lateral view, (b) dorsal view, (c) ventral view, and (d) lateral view of the hyoid bones. A color scale is shown to indicate the gradient in color (that is associated with mineral density) from the highest density in red to lowest density in dark blue. 41

Figure 3.4. Micro-computed tomography images of the hyoid apparatus of an acorn woodpecker, colored for clarity. (a) Left lateral view segmented 3D models. A: paraglossal bone (yellow), B: basihyal bone (blue), C: ceratobranchial bone (green), D: epibranchial bone (red), E: Saddle-shaped joint, F: Y-shaped joint, and G: Circular joint. 43

Figure 3.5. (a) Orthoslice images of the hyoid bone with reconstructed 3D models from micro-computed tomography data. (b) Plot of the measured cross-sectional area at each location. (c) Transverse cross-sectional images at each location showing the shape of hyoid bone along its length. Scale bar: 500 µm. 45

Figure 3.6. (a) Photograph of dissected hyoid apparatus highlighting the imaged locations on the lingual apex. Scanning electron micrographs on the dorsal surface, (b) low magnification and (c) high magnification with the outline of two keratin scales (white dotted lines), and (d) energy dispersive X-ray spectroscopy results. Scanning electron micrographs on the cross-section 48

Figure 3.7. (a) Photograph of dissected hyoid apparatus highlighting the imaged locations on the lingual body. (b-c) Scanning electron micrographs and (d) energy dispersive X-ray spectroscopy results of the dorsal surface. Scanning electron micrographs (e-g) on the longitudinal-section and (h) on the cross-section displaying four different muscles 51

Figure 3.8. Cross-sectional images of the basihyal (BH), ceratobranchial (CB), epibranchial (EB) bones: (a, c, e) Optical micrographs (OM) of each bone, (b, d, f) back-scattered electron (BSE) micrographs with (g,h) the magnified images of the CB bone, and (i, j, k), nanoindentation (modulus) maps overlaid on schematic illustrations of bone regions. 52

Figure 3.9. Bar charts of (a) the Young's modulus and (b) hardness of each bone. The solid-filled bars represent the average value of the stiff bone region and the dash-filled bars represent the average value of the compliant bone region. PG: paraglossal bone (yellow). BH: basihyal bone (blue). CB: ceratobranchial bone (green). EB-1 to EB-3: epibranchial bone (red). 53

Figure 4.1. Head anatomy of an acorn woodpecker (*Melanerpes formicivorus*) from micro-computed tomography. (a) Sagittal-section view and (b) a transparent three-dimensional reconstructed image of the upper and lower beaks (light blue: the upper beak rhamphotheca, yellow: the lower beak rhamphotheca, red: the upper beak bone, and green: the lower beak bone). 68

Figure 4.2. Skull bone structures in (a) domestic chicken (*Gallus gallus*) adapted from [165] and (b) acorn woodpecker (*Melanerpes formicivorus*) adapted from [173]. A dorsal (top), lateral (middle), and ventral (bottom) view reconstructed from micro-computed tomography. Note that X-ray intensity scale is not same between (a) and (b). 69

Figure 4.3. comparison of transverse-cross section view of the skull bone structures in (a) domestic chicken and (b) acorn woodpecker. The frontal bone (left) and the parietal bone (right). The bone morphometry quantification data is given in Table 4.1. The quantification was done at the indicated white rectangle regions on each image. 70

Figure 4.4. Optical and back-scattered scanning electron micrographs of transverse-cross section view of the skull bone structure in (a) domestic chicken and (b) acorn woodpecker. The white rectangles represent the area of higher magnification micrographs of back-scattered scanning electron micrographs. 74

Figure 4.5. Young's moduli from nanoindentation testing of the skull bone in domestic chicken (green) and acorn woodpecker (red). Comparisons where no statistically significant difference was observed are marked with an "ns" symbol. Otherwise, asterisk (*) symbols are marked when $p < 0.05$. 77

Figure 4.6. Schematic diagram of the summarized main findings. Note that F and P are the frontal and parietal bone, respectively. E is the Young's modulus. Blue lines represent relative values of each bone. Blue circles represent the simplified shape of cell type; a closed circle for closed cell, an opened circle for an open cell. 78

Figure 5.1. An example of how a biological observation becomes a scientific design and experiment. A representative anatomical adaption of the skull bone based on the relationship between food source and pecking behavior in woodpeckers, showing (a) two representative species chosen from nine different woodpecker species reported by Burt [182]. 88

Figure 5.2. An illustration of experimental and computational test design of an impact test using 3D printed woodpecker skull models. (a) Lateral (top) and ventral (bottom) views of the 3D reconstructed skull models with its anatomy. Each arrow indicates the palatine and jugal bone, respectively. (b) A photo of an impact test drop tower (left),... 90

Figure 5.3. Experimental results of the impact testing with 3D printed skull models. (a) Measured acceleration on the skull bone near the brain in an impact speed of 3 m/s for three-axes. (b) The

effect of different impact speeds at 1, 2, and 3 m/s on the accelerations at the X-axis. Note that an inset plot shows the linear regression line of acceleration at a 7 ms^{-1} (A_7). 92

Figure 5.4. Computational results of the impact testing with 3D meshed skull models. (a) Five natural frequency modes associated with the vibration of the skull. (b) A representative result of Ricker's pulse analyses at node 1 and 2. (c) The sagittal-section view of the skull model and the plots of von Mises stress at four nodes. 95

Figure 5.5. Nine different woodpeckers reported by Burt [182] and highlighted by Bock [54], showing different anatomical adaptation on the skull bone based on the relationship between food source and pecking behavior. Note that the upper most species, three-toed woodpecker, showed a portion of food in its stomach over 83% from tree larvae; 105

Figure 5.6. Measured acceleration on the skull bone near the brain in an impact speed of 3 m/s. (a) X-axis, (b) Y-axis, (c) Z-axis, and (d) indication of each direction with a photograph of accelerometer attached skull model. Note that the t_1 is the time duration of the first peak on the Model 1 (no overhang) and t_2 is on the Model 2 (with overhang). 107

Figure 5.7. Motion tracking of the beak tip of a 3D printed skull model along the center line to find a pattern of vibration. (a) Time-lapse images captured with a high-speed camera at 0. 57 ms, 3.14 ms, and 6.00 ms, respectively. (b) A plot of the distance from the centerline of the 3D printed beak tip during impact up to 6 ms. 109

Figure 5.8. A comparison of the effect of the frontal overhang in two skull models. (a-d) von Mises stress levels over time. (e-h) In-plane principal stress over time at different locations of each model in an impact speed of 7 m/s. Model 1: No overhang model, Model 2: with overhang model. Note that node locations (1-4) are identical as in Figure 5.2c. 111

Figure 7.1. Examples of bioinspired design of the woodpecker head. (a) A simplified pecking motion of woodpeckers and (b) its empirical characterization of the sponge bone as a shock-absorbing device, adapted from [133]. Note that (1) microglasses, (2) aluminum enclosure, (3) vibration exciter, (4) power amplifier and signal generator, (5) reference accelerometer 122

Figure 7.2. (a) A schematic representation of the jugular vein of human and its intracranial venous system with an image of the QC30 jugular vein compression device, adapted from [208]. (b) Ultrasonography images of the jugular vein without (left) and with collar (right), indicating that a significant increase in the internal jugular vein dilation after collar wearing trials................... 123

Figure 7.3. A schematic illustration of the design and development process of the woodpecker tongue inspired remote actuator made of shape memory alloy and carbon nanotube/polymer composite fibers, taken from [210]. 124

LIST OF TABLES

Table 1.1. The physical variables of representative organisms and tissues. Note that G: gradient, L: layered, H: helical, F: fibrous, T: tubular, C: cellular structure is found in the materials.......... 6

Table 3.1. Dimension, shape, and mechanical properties of each of the hyoid bones. See Figure 3.5a for bone locations... 59

Table 4.1. Two- and three- dimensional bone morphometry results in a chicken and woodpecker. Note that the brain weight is the median value of its average range taken from [179]. The measured values were presented as the mean with a standard deviation (S.D.). 81

Table 5.1. Main variables for mechanical and materials properties, and finite element analysis parameters used in the dynamic impact simulation. 115

ACKNOWLEDGEMENTS

I would like to first gratefully acknowledge my advisor, Dr. Joanna McKittrick, for her passionate and academic guidance and support for my Ph.D. study. I met her in early 2013 for the first time and she accepted me to join her group immediately, she has provided me countless opportunities to develop my research idea in biological materials science as well as to collaborate with other people in different disciplines. She has a passion and ceaseless curiosity on “Mother Nature” and its evolutionary offsprings, she has largely influenced on my thoughts and attitudes toward our Nature and its academic value. I have learned so many things from her, it is not possible to mention all of them here; however, the most important lessons from her are how she leads a research project, how she teaches responsibility to students, and how a person as a principal investigator can be open and respect everyone in other disciplines. She carefully listened to different ideas and try to respect all of them. She gave me a chance to fail even she already knew the things would not be easy. This will be a life-long lesson for me to work with and mentor other people in my future career in various interdisciplinary disciplines.

I would also like to thank my committee members, Drs. Shengqiang Cai, Robert Sah, Mark Ellisman, and David Kisailus for their kind suggestions and support. Even he has not been in my dissertation committee, Dr. Marc Meyers has helped and supported me as a co-mentor of the UCSD Interfaces Training program in multiple publications as well as grant proposals. I am grateful to all of my coauthors, collaborators, and colleagues who have contributed to the successful publication of my research work, including Dr. Steven Naleway, Dr. Sung Sik Hur, Nicholas Yaraghi, Steven Herrera, Dr. Vincent Sherman, Dr. Eric Bushong, Andrei Pissarenko, Adwait Trikanad, Dr. David Restrepo, Dr. Frances Su, Dr. Andrew Marquez, Damian Gonzalez, Dr. Pablo Zavattieri, and Dr. Shu Chien. I have to express my gratitude to my undergraduate research assistants, Yajur Maker, Kathryn Kang, Gracia Innocentia, Damian Gonzalez for their help and active participation in my research projects.

I would like to thank all of my lab mates at the McKittrick lab, Dr. Jae-Ik Choi, Dr. Michael Porter, Dr. Steven Naleway, Dr. Michael Frank, Dr. Wei Huang, Dr. Frances Su, (and future doctors) Jungmin Ha, Keisuke Matsushita, Sean Garner, Isaac Cabrera, and at the Meyers lab, Dr. Shiteng Zhao, Dr. Bin Wang, Dr. Tarah Sullivan, Dr. Vincent Sherman, Dr. Andrew Marquez, Dr. Wen Yang, (future doctors) Haocheng Quan, Zezhou Li, Audrey Velasco-Hogan, and Dr. Po-Yu Chen. I am so lucky to being here at UCSD with them, they kept inspired me to try a different approach and gave me numerous ideas and helpful discussions when I have some weird research data and/or situations. I am grateful to Dr. Ekaterina "Katya" Evdokimenko, Dr. Charlie Chu, Dr. Steve Roberts, Esther Cory, Dr. Michael Tolley, Christopher Cassidy for their help and collaboration.

Finally, I would like to give special thanks and love to my wife, Sosun "Jessica" Ha, without her selfless accompany and support, this work would be impossible. I would like to also thank my parents for their endless support during whole my life and my another parent for their support and underpinning during my Ph.D. years. Again, I am so lucky to have both parents in my life.

This work presented in this dissertation was supported by a Multi-University Research Initiative through the Air Force Office of Scientific Research of the United States (AFOSR-FA9550-15-1-0009) and a National Science Foundation Biomaterials Grant (1507978). Some of the work described here was carried out using shared research resources at the National Center for Microscopy and Imaging Research (NCMIR) at UCSD supported by the NIH under award number P41 GM103412. The authors also would like to acknowledge the digimorph.org (Dr. Jessica A.

Maisano) and NSF grant IIS-0208675 to T. Rowe (for woodpeckers) and NSF grant DBI-0743460 to B. Dumont (for chicken) for sharing the raw CT data. This work was performed in part at the San Diego Nanotechnology Infrastructure (SDNI) of UCSD, a member of the National Nanotechnology Coordinated Infrastructure, which is supported by the National Science Foundation (Grant ECCS-1542148).

Chapter 1, in part, is currently being prepared for submission for publication of the material. Wei Huang, David Restrepo, Pablo Zavattieri, Jae-Young Jung, Zengqian Liu, Robert O. Ritchie, Joanna McKittrick, and David Kisailus. The dissertation author was the primary investigator and author of this material.

Chapter 2, in part, is currently being prepared for submission for publication of the material. Wei Huang, David Restrepo, Pablo Zavattieri, Jae-Young Jung, Zengqian Liu, Robert O. Ritchie, Joanna McKittrick, and David Kisailus. The dissertation author was the primary investigator and author of this material.

Chapter 3, in full, is a reprint of the material as it appears in Acta Biomaterilia. Jae-Young Jung, Steven Naleway, Nicholas Yaraghi, Steven Hererra, Vincent Sherman, Eric Bushong, Mark Ellisman, David Kisailus, and Joanna McKittrick, 2016. The dissertation author was the primary investigator and author of this paper.

Chapter 4, in full, is a reprint of the material as it appears in Journal of the Mechanical Behavior of Biomedical Materials. Jae-Young Jung, Andrei Pissarenko, Nicholas Yaraghi, Steven Naleway, David Kisailus, Marc Meyers, and Joanna McKittrick, 2018. The dissertation author was the primary investigator and author of this paper.

Chapter 5, in full, is a reprint of the material as it appears in Advanced Theory and Simulation. Jae-Young Jung, Andrei Pissarenko, Adwait Trikanad, David Restrepo, Frances Su,

Andrew Marquez, Damian Gonzalez, Steven Naleway, Pablo Zavattieri, and Joanna McKittrick, 2019. The dissertation author was the primary investigator and author of this paper.

VITA

2019 Ph.D. Materials Science and Engineering with a Specialization in Multi-scale Biology

University of California San Diego, La Jolla, CA

Dissertation: "Learning from Nature: An investigation of an impact-resistant system on the woodpecker head as a non-traumatic brain injury animal model"

Advisor: Professor Joanna McKittrick

The UCSD Interfaces Program Co-mentor: Professor Marc A. Meyers

2008 M.E. Chemical Engineering

Dankook University, Yongin, Republic of Korea

Advisor: Professor Woo-Kul Lee

2006 B.E. Chemical Engineering

Dankook University, Seoul, Republic of Korea

PUBLICATIONS

Jung J-Y, Naleway SE, Maker YN, Kang KY, Lee JH, Hur SS, Chien S, McKittrick J, 3D printed templating of extrinsic freeze-casting for macro-micro porous biomaterials, ACS Biomaterials Science and Engineering, In revision.

Jung J-Y, Pissarenko A, Trikanad AA, Restrepo D, Su FY, Marquez A, Gonzalez D, Naleway SE, Zavattieri P, McKittrick J, A natural stress deflector on the head? Mechanical and functional evaluation of the woodpecker skull bones, Advanced Theory and Simulations, 2019;1800152.

Sato KN, Adnersoon AJ, Day JM, Taylor JR, Frank MB, Jung J-Y, McKittrick J, Levin LA, Response of sea urchin fitness traits to environmental gradients across the southern California oxygen minimum zone, Frontiers in Marine Science, 2018;5:258.

Jung J-Y, Pissarenko A, Yaraghi NA, Naleway SE, Kisailus D, Meyers MA, McKittrick J, A comparative analysis of the avian skull: Woodpeckers and chickens, Journal of the Mechanical Behavior of Biomedical Materials 2018:84, 273-280. DOI: doi.org/10.1016/j.jmbbm.2018.05.001.

Huang W, Zaheri A, Jung J-Y, Espinosa HD, McKittrick J. Hierarchical Structure and Compressive Deformation Mechanisms of Bighorn Sheep (Ovis canadensis) Horn, Acta Biomaterialia 2017:64, 1-14. DOI: doi.org/10.1016/j.actbio.2017.09.043.

Huang W, Hongjamrassilp W, Jung J-Y, Hastings PA, Lubarda VA, McKittrick J. Structure and mechanical implications of the pectoral fin skeleton in the Longnose Skate (Chondrichthyes, Batoidea), Acta Biomaterialia 2017:51, 393-407. DOI: dx.doi.org/10.1016/j.actbio.2017.01.026.

Yaraghi NA, Guarín-Zapata N, Grunenfelder LK, Hintsala E, Bhowmick S, Hiller JM, Betts M, Principe EL, Jung J-Y, Sheppard L, Wuhrer R, McKittrick J, Zavattieri PD, Kisailus D. A Sinusoidally-Architected Helicoidal Biocomposite. Advanced Materials 2016;28:6835-6844 DOI: 10.1002/adma.201600786.

Jung J-Y, Naleway SE, Yaraghi NA, Herrera S, Sherman VR, Bushong EA, Ellisman MH, Kisailus D, McKittrick J. Structural analysis of the tongue and hyoid apparatus in a woodpecker. Acta Biomaterialia 2016;37:1-13. DOI: 10.1016/j.actbio.2016.03.030.

Frank MB, Naleway SE, Wirth TS, Jung J-Y, Cheung CL, Loera FB, Medina S, Sato KN, Taylor JRA, McKittrick J. A Protocol for Bioinspired Design: A Ground Sampler Based on Sea Urchin Jaws. Journal of Visualized Experiments 2016; 110:e53554. DOI: 10.3791/53554.

Kim TK, Rustomji CS, Cho H-M, Chun D, Jung J-Y, Caldwell E, Kim Y, Han JH, Jin S. Multi-wall carbon nanotube-embedded lithium cobalt phosphate composites with reduced resistance for high-voltage lithium-ion batteries. Electronic Materials Letters 2016;12:147-55. DOI: 10.1007/s13391-015-5310-8.

Chu Y, Meyers A MA, Wang B, Yang W, Jung J-Y, Coimbra CFM. A Sustainable Substitute for Ivory: the Jarina Seed from the Amazon. Scientific Reports 2015;5:14387. DOI: 10.1038/srep14387.

Kim TK, Moon J, VanSaders B, Chun D, Gardner CJ, Jung J-Y, Wang G, Chen R, Liu Z, Qiao Y, Jin S. Si boride-coated Si nanoparticles with improved thermal oxidation resistance. Nano Energy 2014;9:32-40. DOI: 10.1016/j.nanoen.2014.06.021.

Jung J-Y, Hirata GA, Gundiah G, Derenzo S, Wrasidlo W, Kesari S, Makale MT, McKittrick J. Identification and development of nanoscintillators for biotechnology applications. Journal of Luminescence 2014;154:569-77. DOI: 10.1016/j.jlumin.2014.05.040.

Jung J-Y, Kwon S-J, Han H-S, Yang GF, Lee J-Y, Yang S-J, Cho S-Y, Cha P-R, Kim Y-Y, Kim Y-C, Seok H-K, Ahn J-P. Rapid In Vitro Corrosion Induced by Crack-Like Pathway in Biodegradable Mg-10% Ca Alloy. Microscopy and Microanalysis 2013;19:210-4. DOI: 10.1017/S1431927613012683.

Cho SY, Chae S-W, Choi KW, Seok HK, Kim YC, Jung J-Y, Yang SJ, Kwon GJ, Kim JT, Assad M. Biocompatibility and strength retention of biodegradable Mg-Ca-Zn alloy bone implants. Journal of Biomedical Materials Research Part B-Applied Biomaterials 2013;101B:201-12. DOI: 10.1002/jbm.b.32813.

Cha P-R, Han H-S, Yang G-F, Kim Y-C, Hong K-H, Lee S-C, Jung J-Y, Ahn J-P, Kim Y-Y, Cho S-Y, Byun JY, Lee K-S, Yang S-J, Seok H-K. Biodegradability engineering of biodegradable Mg alloys: Tailoring the electrochemical properties and microstructure of constituent phases. Scientific Reports 2013;3. DOI: 10.1038/srep02367.

Jung J-Y, Kwon S-J, Han H-S, Lee J-Y, Ahn J-P, Yang S-J, Cho S-Y, Cha P-R, Kim Y-C, Seok H-K. In vivo corrosion mechanism by elemental interdiffusion of biodegradable Mg-Ca alloy. Journal of Biomedical Materials Research Part B-Applied Biomaterials 2012;100B:2251-60. DOI: 10.1002/jbm.b.32795.

Cho SY, Chae S-W, Choi KW, Seok HK, Han HS, Yang SJ, Kim YY, Kim JT, Jung J-Y, Assad M. Load-bearing capacity and biological allowable limit of biodegradable metal based on degradation rate in vivo. Journal of Biomedical Materials Research Part B-Applied Biomaterials 2012;100B:1535-44. DOI: 10.1002/jbm.b.32722.

Jung J-Y, Hong Y-J, Choi YS, Jeong S, Lee W-K. A new method for the preparation of bioactive calcium phosphate films hybridized with 1-alpha,25-dihydroxyvitamin D3. Journal of Materials Science-Materials in Medicine 2009;20:2441-53. DOI: 10.1007/s10856-009-3817-y.

Choi YS, Hong YJ, Hur J, Kim MY, Jung J-Y, Lee W-K, Jeong S. Bone nodule formation of MG63 cells is increased by the interplay of signaling pathways cultured on vitamin D3-entrapped calcium phosphate films. Animal Cells and Systems 2009;13:363-70. DOI: 10.1080/19768354.2009.9647231.

Jung J-Y, Han J, Choi S-M, Lee W-K. Variation of characteristics of nonstoichiometric apatite induced by sodium salt. Journal of the Korean Industrial and Engineering Chemistry 2008;19:326-31. Link.

Shin H-Y, Jung J-Y, Kim S-W, Lee W-K. XPS analysis on chemical properties of calcium phosphate thin films and osteoblastic HOS cell responses. Journal of Industrial and Engineering Chemistry 2006;12:476-83. Link.

Jung J-Y, Kwon M-D, Lee W-K. Study on the physicochemical variation of the surface of calcium phosphate thin film dependent on multiple treatments. Journal of Advanced Science and Technology 2006;2.

PRESENTATIONS

(Invited) Jung J-Y. Learning from Nature: An impact-resistant system on the woodpecker head as a non-traumatic brain injury animal model. Hosted by the UCSD MAE, UC San Diego, La Jolla, CA, USA, Jan 2019.

(Invited) Jung J-Y. Avoiding brain injury: A model study of the woodpecker head. Weekly lunch seminar invited by the Center for functional MRI, School of Medicine, UC San Diego, La Jolla, CA, USA, May 2017.

(Invited) McKittrick J, Naleway SE, Frank MB, Jung J-Y, Su F. Preparation and Characterization of Ceramic Scaffolds, 2017 TMS Annual Meeting & Exhibition, San Diego, CA, USA, February 2017

Jung J-Y, Pissarenko A, Naleway SE, Kang KY, Yaraghi NA, Bushong EA, Ellisman MH, Kisalius D, Meyers MA, McKittrick J. Avoiding brain injury: A structural role of the frontal overhang on the skull bone of woodpeckers, 2017 TMS Annual Meeting & Exhibition, San Diego, CA, USA, February 2017

Matsushita AK, Gonzalez D, Frank MB, Jung J-Y, McKittrick J. Microstructural origins of the dynamic behavior of wood and bioinspired designs, 2017 TMS Annual Meeting & Exhibition, San Diego, CA, USA, February 2017

Maker YN, Jung J-Y, Kang KY, Frank MB, McKittrick J. Development of 3D Template Freeze Casted Hydroxyapatite/Magnesium Alloy Biodegradable Implants, 2017 TMS Annual Meeting & Exhibition, San Diego, CA, USA, February 2017

Jung JY, Pissarenko A, Naleway SE, Kang KY, Yaraghi NA, Bushong EA, Ellisman MH, Kisalius D, Meyers MA, McKittrick J. Avoiding brain injury: Structural role of the frontal overhang on the skull bone of woodpeckers, NIH NIBIB Site Visit, 2016 Interfaces Graduate Training Program, UC San Diego, La Jolla, CA, USA, November 2016

Jung JY, Pissarenko A, Naleway SE, Kang KY, Yaraghi NA, Maker YN, Siu SH, Sherman VR, Kisalius D, Meyers MA, McKittrick J. Avoiding Brain Injury: A Comparative Analysis of the Woodpecker Skull, CaliBaja Center for Resilient Materials & Systems Research Summit, Jacobs School of Engineering, UC San Diego, La Jolla, CA, USA, October 2016

Jung J-Y, Avoiding Brain Injury: A Comparative Analysis of the Woodpecker Skull, 2016 Interfaces Research Symposium supported by the NIBIB at NIH and UC San Diego, La Jolla Shores Hotel, La Jolla, CA, USA, July 2016 (Best Quick Talk Presentation Award)

(Invited) Naleway SE, Frank MB, Jung J-Y, Su F, Meyers MA, McKittrick J. Mimicking Biomineralization through Freeze Casting for Bioinspired Materials, 25th AACGE Western Section Conference on Crystal Growth & Epitaxy, Stanford Sierra Camp, Fallen Leaf Lake, CA, USA, June 2016

Jung J-Y, Pissarenko A, Naleway SE, Kang KY, Yaraghi NA, Maker YN, Siu SH, Sherman VR, Kisailus D, Meyers MA, and McKittrick J, Avoiding brain injury: A comparative analysis of the woodpecker skull, Research Expo 2016, Jacobs School of Engineering, UC San Diego, La Jolla, CA, USA, April 2016 (Best Literature Review Award)

Jung J-Y, Naleway S, Sherman V, Kang K, Yaraghi N, Bushong E, Ellisman M, Kisalius D, McKittrick J, Comparative analysis of the woodpecker skull, MRS 2016 Spring, Phoenix, AZ, USA, March 2016

Yaraghi NA, Guarin N, Suksangpanya N, Grunenfelder L, Jung J-Y, Davies M, Jochum T, Hiller J, Betts M, Principe E, Lefebvre J, Wuhrer R, Sheppard L, McKittrick J, Zavattieri PD, Kisailus D, Structural features and toughening mechanisms of the stomatopod dactyl club exocuticle, MRS 2016 Spring, Phoenix, AZ, USA, March 2016

Naleway SE, Jung J-Y, Hur SS, Maker YN, Kang KY, Ix M, Chien S, Meyers M, McKittrick J, 3D printed templating of freeze casting for hierarchical mimetic bone, MRS 2016 Spring, Phoenix, AZ, USA, March 2016

Naleway SE, Gludovatz B, Hosseini MS, Jung J-Y, Schaible E, Ritchie RO, Zavattieri PD, Meyers M, McKittrick J, Why be rigid: Structural analysis of the boxfish carapace, MRS 2016 Spring, Phoenix, AZ, USA, March 2016

Frank MB, Naleway SE, Sato KN, Herrera SA, Gao W, Jung J-Y, Siu SH, Ng J, Torres I, Ismail A, Levin LA, Espinosa HD, Kisailus D, McKittrick J, Mechanical and microstructural properties of Sea Urchin teeth at various ocean depths, MRS 2016 Spring, Phoenix, AZ, USA, March 2016

Frank M, Naleway S, Jung J-Y, McKittrick J, Mars urchin: A bioinspired sediment sampler based on the mouthpiece of a sea urchin, 6th International Conference on Mechanics of Biomaterials and Tissues, Waikoloa, HI, USA, December 2015

Jung J-Y, Naleway S, Yaraghi N, Sherman V, Bushong E, Ellisman M, Kisalius D, McKittrick J, Structural analysis of the tongue and hyoid apparatus of a woodpecker, 6th International Conference on Mechanics of Biomaterials and Tissues Waikoloa, HI, USA December 2015

(Invited) Jung J-Y, Naleway S, McKittrick J, Bioinspired materials investigation and development of biomaterials, Advanced Analysis Center, Korea Institute of Science and Technology, Seoul, South Korea, September 2015

Jung J-Y, Investigation of impact resistant biological materials: The woodpecker, UCSD Interfaces Training Program Student Seminar, La Jolla, CA, USA, May 2015

Jung J-Y, Sherman V, Naleway S, Bushong E, Cory E, Taylor J, Sah R, Ellisman M, Meyers M, McKittrick J, Structural analysis of the woodpecker tongue and hyoid apparatus, UCSD Engineering Expo 2015, La Jolla, CA, USA, April 2015

Frank M, Naleway S, Jung J-Y, Huang W, Cheung C, Loera F, Medina S, Wirth T, Sato K, Taylor J, Levin L, McKittrick J, Microstructure and bio-inspiration application of Aristotle's Lantern, Urchins from the sea to mars UCSD Engineering Expo 2015, La Jolla, CA, USA, April 2015

(Invited) McKittrick J, Naleway S, Frank M, Jung J-Y, Biological materials science: Structures, mechanical properties and bioinspiration, Indian Institute of Science, Bangalore, India, February 2015

Jung J-Y, Frank M, Naleway S, McKittrick J, Bioinspired Materials UCSD Biomedical Engineering Society Lab Expo La Jolla, CA, USA, January 2015

Frank M, Naleway S, Jung J-Y, Su F, McKittrick J, Biological Material Investigations, UCSD Biomedical Engineering Society Lab Expo La Jolla, CA, USA, January 2015

Jung J-Y, Bushong EA, Sherman V, Cory E, Sah R, Ellisman MH, Meyers MA, McKittrick J, Structural analysis of the woodpecker tongue, 144th TMS Annual Meeting & Exhibition, Orlando, FL, USA, March 2015

Jung J-Y, Sherman V, Cory E, Sah R, Meyers M, McKittrick J, Micro- and nano-scale analysis of the woodpecker tongue, The 33rd annual Research Expo 2014 held by the Jacobs School of Engineering, La Jolla, CA, USA, April 2014

(Invited) Seok H-K, Jung J-Y, Kim Y-C, Lee K-E, Lee S-H, Yang S-J, Ahn J-P, Analysis technology of electron microscopy for cell, tissue, and biomaterials 2012 Fall Conference of the Korean Institute of Metals and Materials, Chang-Won, Republic of Korea, October 2012

Jung J-Y, Han H-S, Kim Y-C, Seok H-K, Ahn J-P, In vivo Inverse-preference corrosion phenomena between Mg2Ca(Zn) and primary Mg phase of Mg-Ca-Zn ternary alloy, 2012 Annual Meeting of Bio Medical Engineering Society, Atlanta, GA, USA, October 2012

(Invited) Jung J-Y, Han H-S, Kim Y-C, Seok H-K, Ahn J-P, Variable in vivo corrosion phenomena on Mg-Ca-Zn ternary alloy as biodegradable implant material, 4th Symposium on Biodegradable Metals, Maratea, Italy, August 2012

Jung J-Y, Kwon S-J, Ahn J-P, Han H-S, Lee J-Y, Kim Y-C, Seok H-K, Yang S-J, Kim Y-Y, Cho S-Y, SEM/FIB/TEM analysis of in vivo and in vitro corrosion mechanism and its corrosion product on Mg-Ca biodegradable metal alloy Korean Society of Microscopy, Chuncheon, Republic of Korea, November 2011

Jung J-Y, Kwon S-J, Ahn J-P, Yang S-J, Yang G-F, Kim Y-C, Kim Y-Y, Cho S-Y, Seok H-K, Visualization of in vivo corrosion mechanism of biodegradable Mg-10% Ca alloy, 3rd Symposium on Biodegradable Metals combined in THERMEC'2011, International Conference on Progressing and Manufacturing of Advanced Materials, Quebec, QC, Canada, August 2011

Jung J-Y, Lee J-Y, Kim Y-C, Yang S-J, Kim Y-Y, Cho S-Y, Cha P-R, Seok H-K, Ahn J-P, Tem study of in-vitro corrosion on biodegradable Mg-10% Ca binary alloy, 2nd Symposium on Biodegradable Metals, Maratea, Italy, August 2010

Jung J-Y, Kwon S-J, Yang G-F, Lee J-Y, Cho S-Y, Kim Y-C, Kim Y-Y, Cha P-R, Seok H-K, Ahn J-P, In vivo and in vitro corrosion mechanism study of biodegradable Mg-Ca binary alloy, The Korean Institute of Metals and Materials, Hoengseong-gun, Republic of Korea, April 2010

Jung J-Y, Lee W-K, Effect of immobilization of 1α,25-Dihydroxyvitamin D3 onto calcium phosphate thin films on the osteoblastic responses, 6th Combined Meeting of the Orthopaedic Research Societies, Honolulu, HI, USA, October 2007

Jung J-Y, Kwon M-D, Lee W-K, Effect of immobilized drug within calcium phosphate matrix on the differentiation of osteoblastic hos cells, International Association of Nanotechnology, San Francisco, CA, USA, June 2006

Jung J-Y, Kwon M-D, Kim S-H, Shin H-Y, Lee W-K, Effect of substitution of 1α,25-Dihydroxyvitamin D3 onto calcium phosphate thin film on the osteoblastic responses, Korean Society of Industrial and Engineering Chemistry, Jeonju, Republic of Korea, May 2006

ABSTRACT OF DISSERTATION

Learning from Nature: An investigation of an impact-resistant system on the woodpecker head as a non-traumatic brain injury animal model

by

Jae-Young Jung

Doctor of Philosophy in Materials Science and Engineering

with a Specialization in Multi-scale Biology

University of California San Diego, 2019

Professor Joanna McKittrick, Chair

Impact resistant structures and materials have been evolved in nature during millions of years of evolution. Some examples of energy absorbent biological materials have been recently reported; however, a better comprehensive understanding of impact-resistant biological materials is still required to compare their unique features: a degree of mineralization, specific mechanical behavior and/or loading condition of tissue/animal, and intentional (active) or indirect (passive) modification of the innate structure/material. The woodpecker head was chosen as a representative

impact-resistant material/structure found in nature because woodpeckers avoid brain injury while they peck at trees up to 20 Hz with speeds up to 7 m/s, undergoing decelerations up to 1,200 g.

The brain is one of the most important and complicated organs, but it is delicate and therefore needs to be protected from external forces. This makes the pecking behavior of the woodpecker so impressive, as they are not known to sustain any brain injury due to their anatomical adaptations (e.g., a specialized beak, skull bone, and hyoid bone). However, the relationship between the morphology of the woodpecker head and its mechanical function against damage from daily pecking habits remain an open question. The shape of the hyoid apparatus is unusual in woodpeckers and its structure and mechanical properties have not been reported in detail. Moreover, the shape and mechanical properties of the skull bone of woodpeckers is different from other non-pecking birds. Therefore, the research works throughout this dissertation aim to examine the anatomical structure, composition, and mechanical properties of the hyoid bone and the skull bone, and to find an interspecies variation of the skull bone morphology in woodpeckers eventually in order to determine its potential role in energy absorption and dissipation as an efficient protection of the brain. Aided by recent technical advancements, such as multiscale imaging tools (micro-computed tomography, optical and scanning electron microscopy), 3D printing, high-precision, miniaturized sensors, and computational simulation, these questions can be explored by applying new materials science concepts of bioinspiration and bioexploration to identify adapted structures/materials in a design that results from millions of years of evolution.

The hyoid apparatus has four distinct bone sections, with three joints between these sections. Nanoindentation results on cross-sectional regions of each bone reveal a previously unreported structure consisting of a stiff core and outer, more compliant shell with moduli of up to 27.4 GPa and 8.5 GPa, respectively. The bending resistance is low at the posterior section of the hyoid bones, indicating that this region has a high degree of flexibility to absorb impact. In the skull bone of woodpeckers compared to the chicken skull, two different strategies are found: the skull bone of the woodpecker shows a relatively small but uniform level of closed porosity, a higher degree of mineralization, and a higher cortical to skull bone ratio. From the 3D printing and computational simulation approach, two main features, including the beam-like bar structure of the jugal bone acting as the main stress deflector and the high natural frequency of the skull bone of woodpeckers can teach two lessons for potential materials development as well as engineering applications: 1) protection of a delicate internal organ occurs by redirection of the main stress pathway and 2) a large mismatch of the natural frequencies between the skull and brain avoids resonance and reduces the overall load experienced by the brain.

Lastly, bioinspired designs and engineering applications will be discussed using some case studies in biological materials for the development of protective devices or robots. This novel approach will provide a new insight to many researchers and engineers in materials science and mechanical engineering disciplines to teach how the natural materials have evolved to adapt its impact-resistant ability against different environments.

CHAPTER 1: INTRODUCTION

1.1 **Impact-resistant biological materials**

Biological materials are known to be lightweight and high-performance, being strong but tough. The study of biological materials aims to investigate natural materials (e.g., bone, feathers, and skin) through mechanical and structural characterization. Among these biological materials, research on impact-resistance or damage-tolerance are relatively rare because of lack of the knowledge. The abalone nacre is a good example of highly tough and strong biological material, possessing a brick-and-mortar structure which has multiple length scales as a hierarchical structure to yield an enhanced toughness by spreading damage over larger areas, therefore, many researchers have attempted to mimic it to develop energy-absorbent synthetic composite materials [1-3].

McKittrick *et al.* [4] described representative energy absorbent natural materials in mammals by comparing mineralized materials (i.e., bones, teeth, antler, and tusks) and non-mineralized materials (i.e., horn and hoof), highlighting the effect of mineralization on the work of fracture and bending strength, as shown in Figure 1.1a. The authors specifically emphasized that the relationships between structural and mechanical properties in terms of energy absorption mechanisms and suggested possible bioinspired design strategies including: implementation of tubules, a density gradient, Young's modulus gradient, and a two-phase composite (crystalline fibers with amorphous matrix) based on their findings of the effect of mineralization on the structure-property relationship as shown in Figure 1.1b.

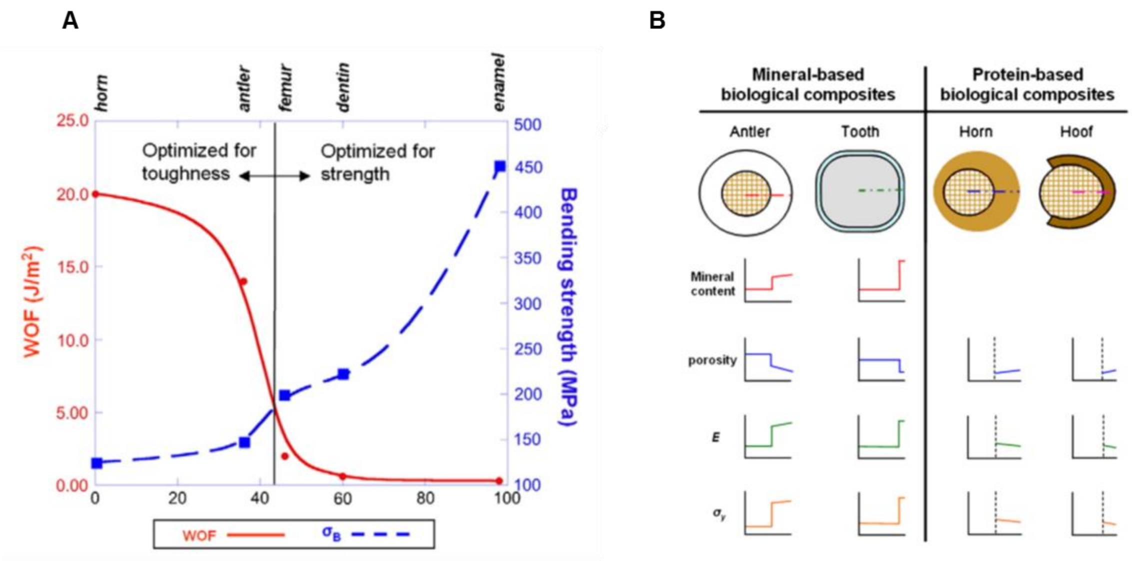

Figure 1.1. (A) Effect of mineralization on the work of fracture (WOF) and bending strength. (B) Property and structural gradients across antler, tooth, horn, and hoof. Images taken from [4].

On top of these suggestions, there are recent findings of structural design elements as shown in Figure 1.2 [5]: some structures are known to have good toughness among the eight suggested elements, as organized as below.

- Tubular structure: found in aligned and organized porous materials for energy dissipation and anti-crack propagation.

- Gradient structure: known to be materials which have property mismatch, for example, elastic modulus and/or relative density, to avoid interfacial stress buildup.

- Helical structure: commonly found in fibrous or composite materials to provide energy absorption capability, having multiple directions and in-plane isotropy.

- Layered structure: found in complex composite materials, having more interfaces between two-phase, which are commonly composed of soft, polymeric and brittle, ceramic materials.

- Cellular structure: known as foam structure, usually lightweight porous materials, offering deflected stress distribution in a specific direction to dissipate energy.

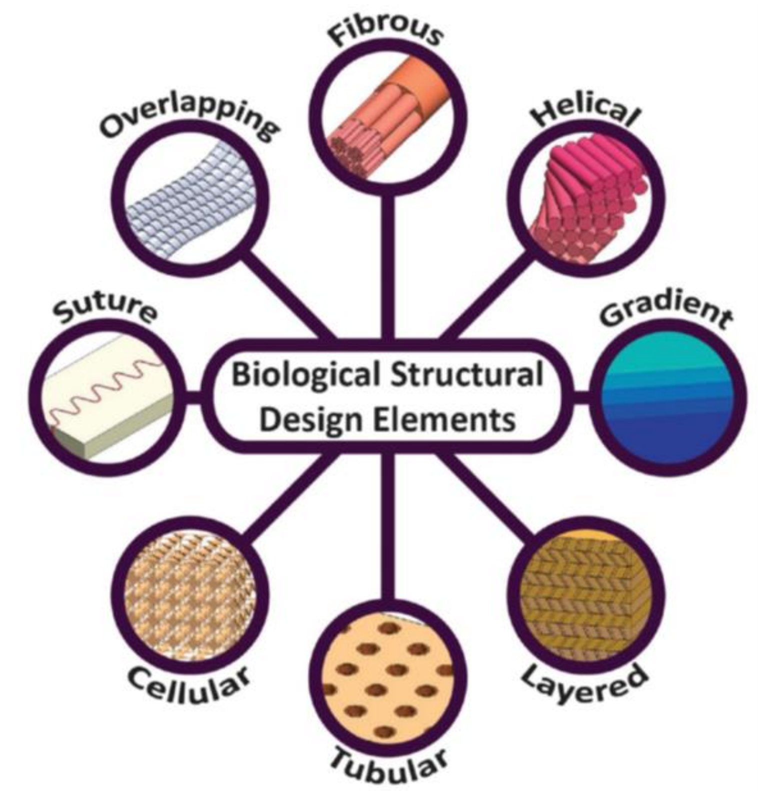

Figure 1.2. Diagram of the eight most common biological structural design elements, taken from [5].

In some cases, a structure can be identified by applying only a single structural element out of the eight elements, for example, horn has a tubular structure [6] or fish scale have a layered structure [7]; however, many cases are also associated to have at least two or, sometimes, three or higher number of structural elements at the same time: boxfish show not only a suture structure on its scute but also a helical fiber structure on its non-mineralized collagen matrix [8, 9]. These aforementioned structures will be further discussed in detail with some representative examples of living organisms found in Nature in this section in terms of impact-resistance and energy-absorbent capability.

1.1.1 Basic principles of impact mechanics and its associated variables

In physics, impact means a series of physical phenomena including the following phenomena: elastic, plastic, shock wave propagation, fracture, fragmentation, perforation, and spallation [10]. To explain this, the kinetic energy (E_k) needs to be introduced with a simple equation with the velocity (v) of a mass (m) and acceleration (a), defined as:

$$E_k = \frac{Fv^2}{2a} \tag{1.1}$$

where F is an impact force which is equal to a mass multiplies an acceleration. Therefore, the impact force and velocity, and acceleration are important variables to describe the impact mechanics.

1.1.2 Fracture toughness and work of fracture of a material

Toughness is the capacity of a material's energy absorption and plastic deformation without fracturing [11, 12]. It can be derived by integrating stress-strain curve from mechanical testing of a material. A tough material should be both strong and ductile to withstand both high stresses and strains.

Fracture toughness (K_c) is defined at a critical stress of a material with its crack propagation (σ_c) and crack length (a) as below:

$$K_c = Y\sigma_c\sqrt{\pi a} \tag{1.2}$$

where Y is a dimensionless variable associated with both crack and specimen sizes, geometries, and loading conditions. In a thickness, the plain strain fracture toughness (K_{Ic}), which is the plain strain toughness for mode I crack displacement (opening mode), also can be used frequently in materials science and fracture mechanics [13, 14].

Work of fracture (or work to fracture, W_f), which can be defined as the work required to break a solid to form two surfaces) is also frequently used to represent the amount of absorbed energy of a material over the measured surface area [11, 12, 14]. These two main variables for fracture mechanics will be discussed in detail in this dissertation later but the some representative examples are tabulated in Table 1.1 and as shown in Figure 1.3.

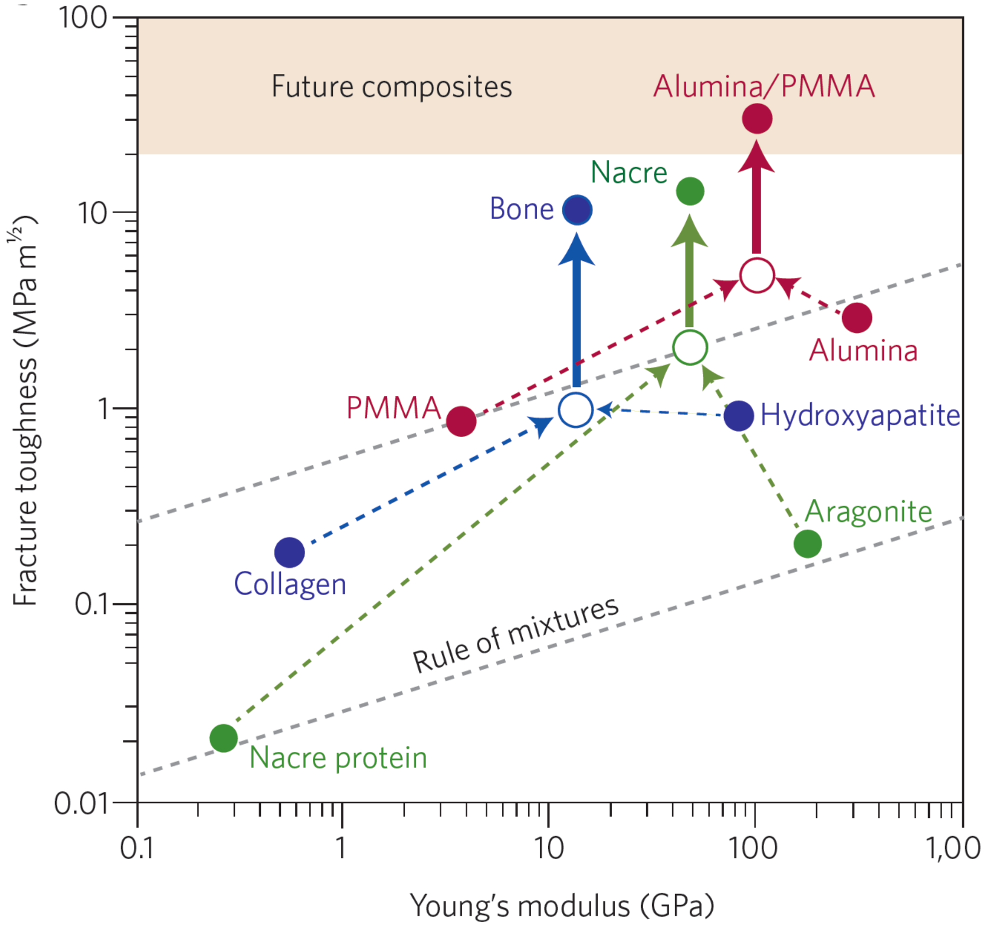

Figure 1.3. A plot of fracture toughness over the Young's modulus of natural and synthetic materials [15].

Table 1.1. The physical variables of representative organisms and tissues. Note that G: gradient, L: layered, H: helical, F: fibrous, T: tubular, C: cellular structure is found in the materials.

	Impact speed (m/s)	Max Force (N)	Deceleration force (1 $\boldsymbol{g}$ = 9.8 m/s^2)	Impact duration (ms)	Total body masses (g)	Impacted tissue masses (g)	Impact energy (J)	Work of fracture (KJ/m^2)	Fracture toughness ($MPa\cdot\sqrt{m}$)	Type of structural elements [5]
Mollusk shells (i.e., Abalone)	-	-	-	-	~ 830 [16]	-	-	12 [11]	10 [17, 18]	G, L
Smashing of the dactyl club of a mantis shrimp on a shell [19, 20]	23	700	10,600 $\boldsymbol{g}$ (104,000 m/s^2)	2.2	~ 55	5.5†	1.5	-	-	H, F, L, G
Bone (human femur) [18, 21]	3.9	~ 860	-	-	-	2,002	15	10 [11] (bovine)	2 – 8 [25]	F, T, C, G
Antlers [18, 22, 23]	11	-	-	-	-	-	-	~ 62 [11, 22]	~ 10 [24]	F, T, C, G
Teeth (Human) [18]	0.2 (biting)	~ 700	0.1 $\boldsymbol{g}$ (0.7 m/s^2)	-	-	11 g (max per tooth)	0.9-1.0 [25]	-	~ 8 (dentin), ~ 4 (enamel)	F, T, C
Wood (baseball bat, maple) [18, 26]	40	37,000	12,900 $\boldsymbol{g}$ (126,420 m/s^2)	0.7	a ball: 145 a bat: 940	1,085	4,300	30 (Oak plywood [11])	-	C
Banging of the horns of two bighorn sheep [27]	9	3,400	450 $\boldsymbol{g}$ (4,400 m/s^2)	20.0	~ 230,000	-	4,600	-	-	T, G
Running impact on hooves of a horse [28]	2.2	38,000	19 $\boldsymbol{g}$ - 76 $\boldsymbol{g}$ (188 ~ 746 m/s^2)	37.3	~ 500,000	-	4,800	22.8 [29]	-	T, G
Pecking of an acorn woodpecker [30]	7	72	1,200 $\boldsymbol{g}$ (11,800 m/s^2)	5.8	~ 60	~ 6 g (the mass of the head)	0.2	-	-	G, L, T

†Assumed it is a 10% of body mass

Table 1.1 describes the main variables of representative physical impacts found in biological materials. The range of impact speeds is from 0.2 m/s (the biting impact of the human teeth) to 40 m/s (hitting of a based ball and bat). The maximum impact forces are ranged from 72 N (woodpecker) to 38,000 N (running impact on hooves of a horse). Moreover, the deceleration (or acceleration) forces are collected from 0.1 g (teeth) to 12,900 g (a baseball and bat). When considering the size and mass, the impact energy is important variables for the impact-resistant materials found to range from 0.2 J in a woodpecker to 4,800 J in the hooves. In case of materials which cannot make an impact by itself, the work of fracture and fracture toughness are important, ranged from 10 KJ/m^2 (human femur bone) to 62 KJ/m^2 (antlers) and 2 MPa·$\sqrt{m}$ (human femur) to 10 MPa·$\sqrt{m}$ (abalone shells and antlers). Each type of structural element is noted at each case of material/impact system.

Due to the smaller body size and mass, the woodpecker shows the smallest impact energy (0.15 J). In addition, the woodpecker shows an impact speed of 7 m/s and the smallest maximum force of 72 N among the other examples in Table 1.1; however, it shows the highest deceleration among the selected animals and tissues. Possessing the highest deceleration implies that the woodpecker is particularly considered to be a high deceleration force-resistant, unlike other impact energy-resistant biological materials. Because of the systemic nature of the woodpecker head and its close relationship with the brain, which needs to be highly protected, the woodpecker head needs to be protective in different ways to protect its internal organ while the other impact-resistant materials in a limb or exoskeletons, which could be a not fatal to threat its life even when the tissues/organs are totally damaged. The dissertation will focus on how the woodpecker head is impact-tolerant to protect the brain as a systemic protective device by comparing other impact-resistant biological materials in Table 1.1.

1.1.3 **Representative organisms and tissues of impact-resistant biological materials**

Figure 1.4. Representative organisms and tissues known to be impact-resistant biological materials. (A) Smashing of a mantis shrimp with its dactyl club on a crustacean shell [31], (B) bighorn sheep horns [32], (C) horse hooves [33], and (D) woodpecker head [34].

Based on the above basic principles of impact mechanics, four different models are selected with the aforementioned important variables as shown in Figure 1.4.

1.1.4 **Mineralized vs. non-mineralized materials**

Nature has utilized some limited elements and materials for living organisms. Especially, to protect the skeletons and internal organs, many organisms used less than 20% of elements, for example, carbon, oxygen, nitrogen, sulfur, calcium, phosphorus, sodium, magnesium, iron, and chloride out of entire 92 naturally occurred elements on earth [13]. In this section, two main categories will be discussed to represent impact-resistant biological materials: mineralized vs. non-mineralized as shown in Figure 1.1b.

Mineralized materials are commonly found in forms of calcium phosphate or calcium carbonate [13, 35, 36]. The calcium phosphate compound is frequently substituted with other elements, for example, hydroxyl group (OH) is often substituted by F in the mammal teeth as the fluorapatite, $Ca_5(PO_4)_3F$ [37, 38] or Ca is substituted by Mg in the sea urchin teeth as calcium carbonate compounds (i.e., $Ca_xMg_{(1-x)}(PO)_4CO_3$) [39-41]. In some rare cases, magnetite (Fe_3O_4) can be reinforced as a structural element for stiff teeth in the chiton stylus [42-44].

Non-mineralized materials are typically composed of proteins or polysaccharides in animals and plants. For instance, stacked dead keratin cell layers are found as a protein in many animals, such as horn and hoof of mammals, beaks, claws, and bird feathers [6, 45-49]. Chitin (polysaccharide) also found in many animals (e.g., mantis shrimp dactyl club [50] or chitin tooth [42-44, 51]) but this is mainly composed of a derivative of glucose. Collagens are the most common proteins found in structural bones in many animals as either mineralized or non-mineralized and fibrillar or non-fibrillar form [52, 53].

1.1.5 **Offensive vs. defensive**

The woodpecker head is a good example of being considered as not only offensive (against tree) but defensive (to the brain) tools simultaneously since the beaks are used as an offensive excavating device for digging a hole at the surface of trees, while the skull bone plays an important role as a protective device for its brain. In detail, when woodpeckers peck against a tree, it must be an aggressive way to find the preys, for example, larvae or worms who have developed a hiding strategy to protect by themselves. With a 7 m/s of impact speed, a 1,200 ***g*** of deceleration force, and a sharp straight bill, pecking of woodpeckers is a threat that can effectively expose prey [30].

Woodpeckers can easily capture the prey with their highly elongated tongue (hyoid apparatus) [54]. Note that at the moment of impact, compressive stress waves propagate through the beak bone to dissipate the impact energy. An energy dissipation mechanism or a mitigation of the direct stress wave to the brain is essential to protect the woodpecker's brain. The more mineralized, thicker, and more porous skull bone structure of woodpeckers by implementing a comparative analysis with the skull bone of chickens, might be helpful to understand its potential mitigation mechanism but the more detailed strategies still need be further investigated.

Keratin materials can be found for both offensive and defensive purposes in animals. The most common offensive weapons are horns and claws. Horns in the Bovidae family are considered as weapons in intraspecific combats [27, 55]. Bighorn sheep hurl themselves with a speed of 20 miles per hour fighting with each other for dominance or mating rights by clashing their large curved horns. The maximum force during combat can reach 3,400 N, with an impact energy near 3,500 J [27]. The deceleration can be as high as 450g [56]. Most of the impact energy is absorbed by plastic deformation, which provides protection to the skull [57]. Keratin materials can also play defensive roles to protect internal structures. In equine hoof wall, which is made of keratin, it has been found that the tubular and lamellar structure in it can redirect crack propagation through it thus protecting the internal bony skeleton [58]. Pangolin scales are also keratin armors that can protect the body from penetration of predator's teeth [59, 60].

1.1.6 **Active vs. passive**

Animals use the adenosine triphosphate (ATP) molecule as the source of energy for motion and movement (defined as motility) by muscle contractions and connected skeletons [61]. This ATPs-related motion of animal is defined as an active mechanism in this review paper. The active mechanism can be also interactive because animal can decide to do a specific behavior or not, based on its experience, consequences, and/or environments. However, if a horse uses its hooves when it is running, this can be categorized as a passive mechanism, because animals just utilize their innate body parts or tissues, which is not able to control the growth rate or existence itself. Plants move by mechanical stimulation or sudden internal pressure change via either hydration or dehydration, which can be categorized as a passive motion. To summarize, the main differences of the two terms are depending on 1) if there is energy-related active motion or 2) if the creatures can make a decision to do a certain behavior or not. For example, the hammering of mantis shrimp dactyl club and the pecking of woodpecker's head is an example of an active mechanism because animals use their muscles and body to make the movement. They can stop this behavior if the behavior consumes too much energy or if they experienced any pain or negative consequences (although it is very rare or hard to observe). In addition, there is an interesting, combined active-passive mechanism; the hydration/dehydration of the bighorn sheep horns are basically phase transition of the particular dead tissue structures, not directly related to the ATP consumption in the body; however, the sheep can soak their horns into water to make it wet as a preparation of upcoming battle [62].

1.2 **Mollusk shells (abalone shell: nacre)**

An abalone shell has been investigated as a representative example of tough materials found in mollusk shells. It has a layered (lamellar) structure composed of mineral bridges (95 wt.% mineral content as the stacked cell-like mineral phase) and chitin fibril network (5 wt.% soft biopolymeric fibrous matrix of chitin fibers). As shown in Figure 1.5, its hierarchical sandwich-like structure is consisting of polygonal aragonite platelets (200 ~ 500 nm of thickness) and interlayer of the organic polymer (5~20 nm of thickness). At microscale, the size of mineral tiles is ranged from 8 to 12 μm with a thickness of 0.5 μm. Owing to this hierarchical structure from nanoscale to microscale, the fracture toughness of an abalone shell shows an higher order of magnitude (10 MPa$\sqrt{m}$) than that of aragonite (0.25 MPa$\sqrt{m}$) itself [15]. It could be not only protective from ocean wave that make an impact on the shells but also against many marine predators who attempt to attack their shells. Using a dog-bone shaped sample, the tensile strength of nacre was reported as 65 MPa when parallelly loaded to the plain of growth [63]. Also, the shear strength also found to be around 37 MPa (mean) with an average maximum shear strain of 0.3, which can be converted to 51 MPa when it considered a majority of failure through tile pull-out, not through tile fracture mechanism [63]. It was concluded that there are three main failure mechanisms at the tile interface: 1) a nanoscale mineral bridge fracture [64-66], 2) a friction-related toughening mechanism through its nanoasperties (a roughness at nanoscale) [67], and 3) a toughening from an organic-polymeric glue [68]. Lastly, a fracture through each of individual tiles is also found [63].

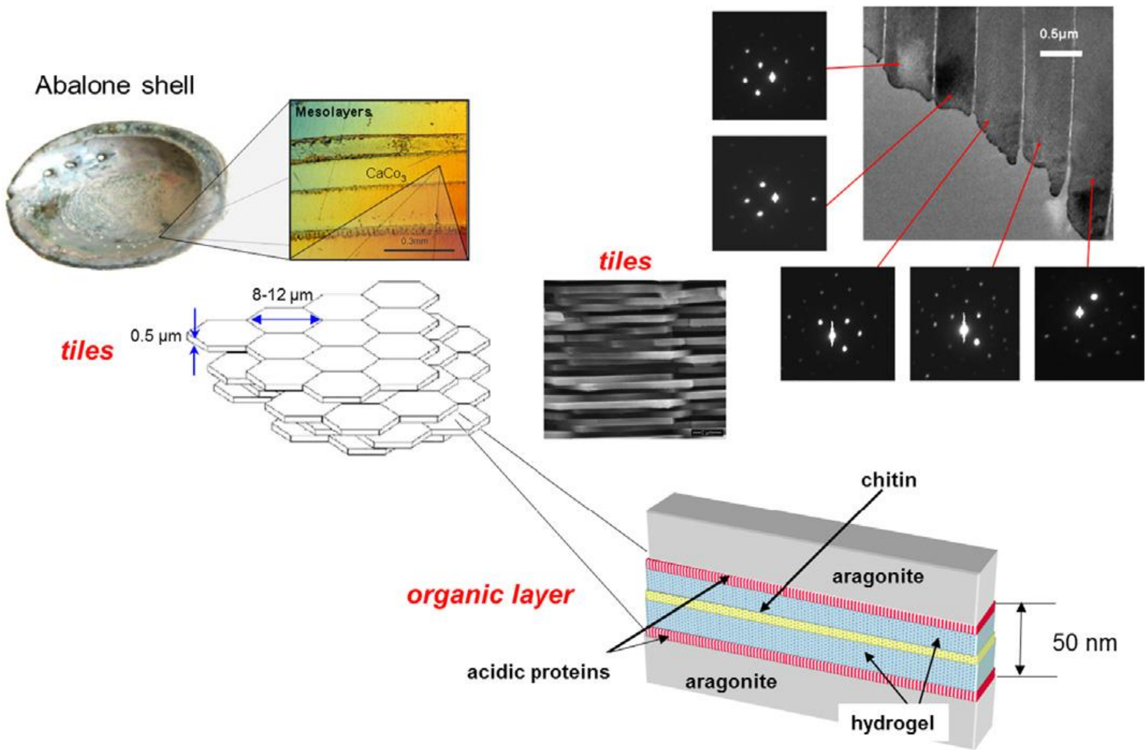

Figure 1.5. A hierarchical structure of abalone shell as a representative example of the mollusk shells, taken from [69]. The mesolayers (left bottom) showed a tablet pullout toughening mechanism as following with the growth layers (middle), which are combined by mineral bridges (top right) and chitin fibril network (bottom right). This is known to be a famous “brick and mortar” layered structure, taken from [69].

1.3 The dactyl club of a mantis shrimp

The nacreous layered structure aforementioned has known to be the toughest materials found in nature for a decade but it turned out that it can be also vulnerable, when it attacked by other aggressive marine organisms, for example, the mantis shrimp [50] as shown in Figure 1.4a and Figure 1.6a. How the mantis shrimp made a successful attack against the nacreous shells was to utilize its highly-mineralized dactyl club to make a high-speed (up to 23 m/s) and high-acceleration (104,000 m/s^2) impact [19, 20], as shown in Figure 1.6b-i as a time-series of an impact on a snail. It is surprised many researchers that the dactyl club can sustain without any catastrophic failure against the shells with multiple impacts. Soon after, materials scientists started to investigate impact-resistant or damage-tolerant materials in terms of the characterization of structural, mechanical, and chemical properties. As a result, Weaver et al. [50] found that the dactyl clubs has a multiscale hierarchical structure with a helicoidal chitin fibrillar structure (Figure 1.6j) in a specific impact region through the SEM fractography (Figure 1.6k) and the transverse cross-section image (Figure 1.6l). In addition, Yaraghi et al. [31] found that a fibrous herringbone-modified helicoidal architecture identified in its appendage provides improved stress distribution with enhanced energy absorption under the compressive loading when it is impacted through nanoscale toughening mechanisms using two different indentations: a conventional nano-indentation and *in-situ* transmission electron microscopy picoindentation.

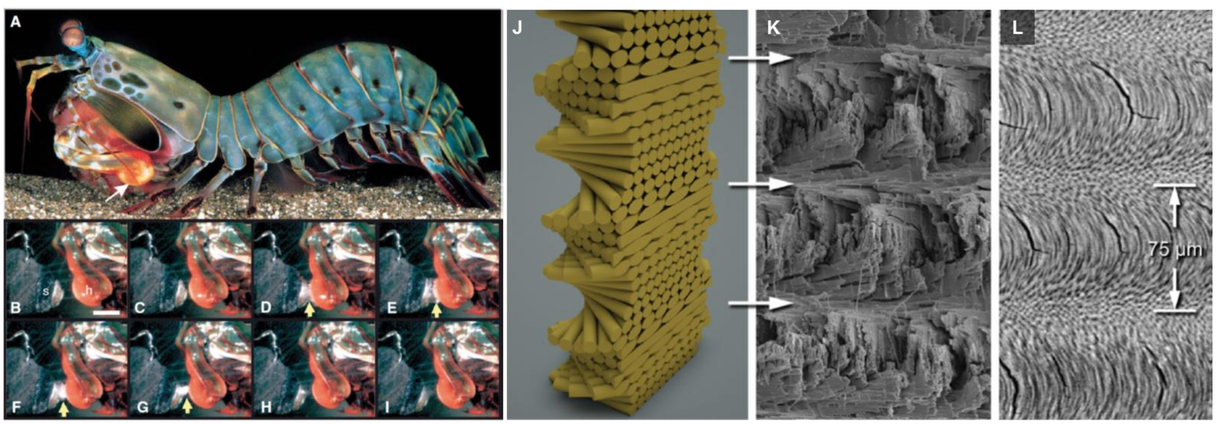

Figure 1.6. Peacock mantis shrimp use a pair of large raptorial appendages (A, white arrow) to strike hard objects with such high speeds that cavitation bubbles form between the appendage and striking surface, taken from [20] . (B–I) The dactyl heel (h) of the raptorial appendage strikes a snail (s) that is loosely wired to a stick. Images recorded at 0.2 ms intervals. Scale bar, 1 cm. Cavitation (yellow arrow) is visible between the dactyl heel and snail (D–G). Taken from [19]. Chitin fibril helicoidal structural motif within the periodic region (with periodicity: ~75 mm), taken from [70]. Comparisons between a generalized three-dimensional model of a helicoid (J) with an SEM fractograph (K) and a polished surface from a transverse cross-section (L).

1.4 Bone and antlers

Bone has been widely known to be one of the most important impact-resistant biological materials to support the body and protect the internal organs [71]. Bone is a highly mineralized composite with hydroxyapatite minerals ($Ca_{10}(PO4)_6(OH)_2$) and interconnected collagen fibrils to add toughness on top of its stiffness. The main chemical compositions are Ca, P, O, Mg, and C [13]. It has a multiscale hierarchical structure, at the macro-level, it is usually categorized as cortical (or compact) and cancellous (or trabecular, or sponge) bone. At the microscale, it is composed of stacks of osteons, Haversian canals, and small lacuna spaces. At the nanoscale level, the collagen molecules exists as a form of tropocollagen triple helix and interspersed between the hydroxyapatite mineral crystals [22]. The structure of the bone and antlers is almost same as shown in Figure 1.7.

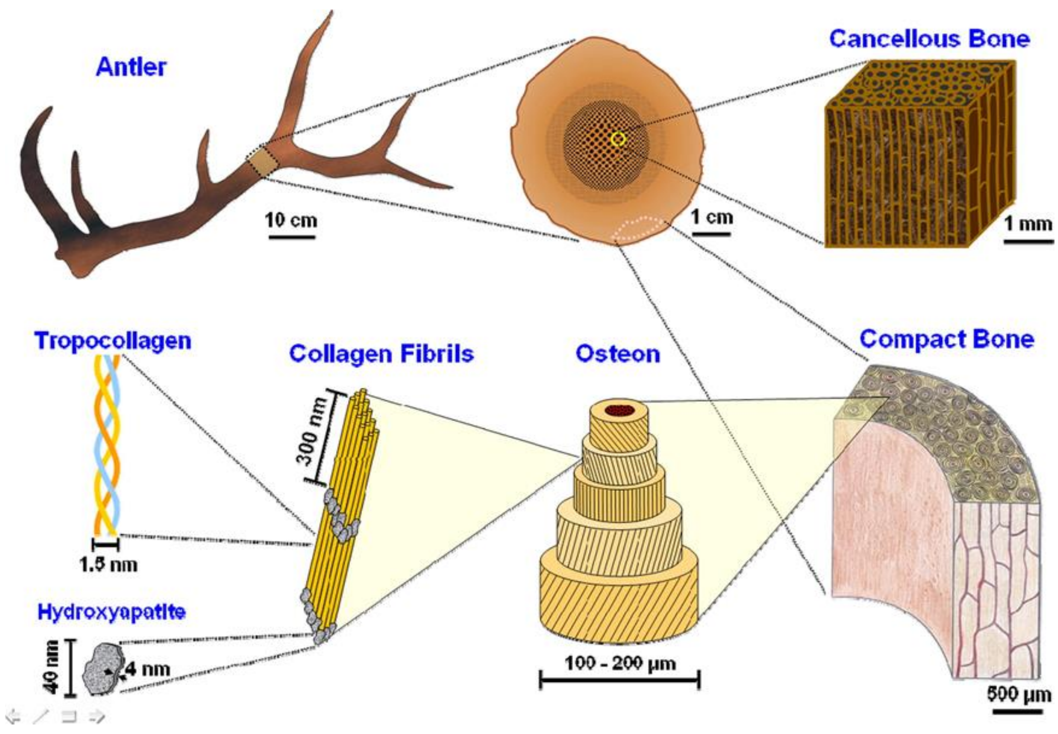

Figure 1.7. Hierarchical structure of antlers. Antlers are composed of compact bone as the outer layer and cancellous (trabecular or spongy) bone in the interior. The compact bone consists of osteons, which are concentric lamellae surrounding a central blood vessel. Each lamella has oriented type I collagen fibrils with a mineral (carbonated apatite) interspersed between or along them. The collagen fibrils are composed of tropocollagen, a helically arranged macromolecule. Taken from [22].

The mechanical properties of bone and antlers have been reported widely [22, 72-79]. Due to its multiscale hierarchical structure, it provides a stiffness and toughness at the same time. The reported fracture toughness of the bovine femur bone and the elk antler is reported as 1.8 ~ 6.4 $MPa\sqrt{m}$ and 1.8 ~ 10.3 $MPa\sqrt{m}$, respectively [24]. Because of the similar structure, it shows almost same toughening mechanism including crack deflection by osteons, uncracked ligament bridging, and a formation of microcracks but the antler shows a 50% higher fracture toughness than the bone because of the lower mineral content and different fracture surface properties [24].

1.5 **Teeth**

The teeth are well known classic biological materials which are composed of 1) the harder and stiffer enamel to be wear-resistant and 2) the more compliant and softer dentin to be protective and energy absorbent from the repeats of occlusal (biting) forces up to 1 kN in humans [80, 81]. A morphology of the fully developed human tooth structure is illustrated as shown in Figure 1.8; the outermost enamel has a mineral content of 96 wt% (hydroxyapatite) while the dentin has a 70 wt% of mineral content [82]. The dentin is coated and surrounded by the enamel and is also made up of the soft dentin-pulp complex. The enamel has a 95 GPa of the elastic modulus and a 3.5 GPa of the hardness, while the dentin has an 18 GPa of the elastic modulus and a 0.6 GPa of the hardness through Vickers micro-indentation tests [80]. These mechanical properties are due to the differences of the mineral content between two parts. In contrast, the measured fracture toughness of the enamel is ranged from 0.7 to 1.5 MPa$\sqrt{m}$ depends on the loading direction; however, that of the dentin is measured as ~ 3.1 MPa$\sqrt{m}$. Early studies on the teeth, before finding the dentin-enamel junction (DEJ) reported by Lin et al. [83], have only focused on the dentin's compliant material property; however, a study conducted by Imbeni et al. [82] has elucidated that its fracture toughness is also dominated by the co-existence of the dentin and the DEJ, which is the interface of the dental and enamel layers. The authors concluded that the measured fracture toughness of the dentin and DEJ is calculated as 0.154 KJ/m^2 (when K_c = 1.8 MPa$\sqrt{m}$) and 0.115 KJ/m^2 while that of the enamel is measured as 0.01 – 0.025 KJ/m^2. Therefore, the dentin and DEJ can be considered as the main regions to absorb impact energy by having different mechanisms. To be specific, the dentin has four distinct toughening mechanisms: 1) crack deflection, 2) crack bridging (by collagen fibers), (3) ligament bridging without cracks, and (4) microcracking [84]. The DEJ has a ~ 75% of fracture toughness by having a crack-arresting mechanism mainly due to the elastic mismatch [82]. Other adjacent tissues including alveolus bone socket, cementum, pulp, and periodontal ligament are present as shown in Figure 1.8.

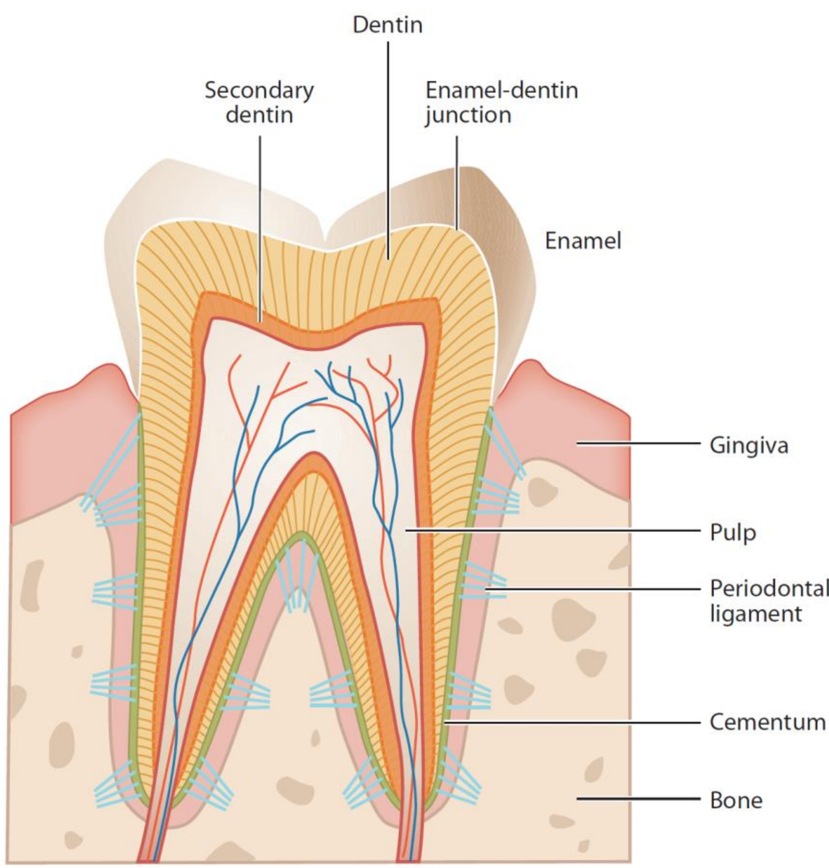

Figure 1.8. A schematic illustration of the human teeth structure, taken from [80].

1.6 **Wood**

In a tree's natural life, high winds are a persistent mechanical threat causing failure at wind speeds over approximately 25 m/s or ~400 kN·m of applied force [85]. Some trees in especially storm-prone regions such as Caribbean palm species have evolved passive adaptations including pronounced basal trunk swelling and trunk tapering combined with thick roots [86]. Trees can also grow or shed limbs in response to stress as an active response to loading (albeit at a longer time scale compared to animal behaviors). This is especially critical for a tree to survive winds as a larger canopy increases drag forces. With the proper canopy, however, a tree's branches can act as dynamic mass dampeners to mitigate harmonic and resonant swaying frequencies, minimizing the transfer of wind energy to the trunk and root system [85].

As an engineering material, the crushing stress, plateau stress, and modulus of elasticity of wood typically increase with strain rate, but wood's passive strengthening mechanisms are not yet well understood [87, 88]. That wood strength decreases with increased load duration was first described in the 1950s using the Madison curve, in which 1x1s in clear Douglas fir beams were subjected to constant loads ranging from 60 – 95% of the average failure load of static bending tests (time to failure = 5 minutes). An empirical relationship was derived between strength and load duration over a data set with loading times ranging from 10 years to less than a second [89]. The hyperbolic curve expressed in the below equation in which is the stress level (SL) as a percent of the ultimate strength in static loading and tf is time to failure (seconds):

$$SL = 1.83 + 108.4\, t_f^{-0.0464} \tag{1.3}$$

Recent studies using split Hopkinson pressure bar (SHPB) support the Madison curve even at load durations of tens of microseconds, with failure occurring at loads 230% of that of the static strength [88, 90]. Based on the dynamic crushing behavior of engineered cellular solids, the four commonly suggested strengthening mechanisms are: 1) strain rate sensitivity of the cell wall material, 2) micro-inertial effects of the cell wall, 3) the contribution of air trapped by the closed pores, and 4) shock wave effects [87, 91-93]. The relative importance and interaction of these factors are not yet known. Strengthening is observed at strain-rates below which micro-inertial and shock wave effects are negligible, for example, and few studies exist on the strain-rate sensitivity of the cell walls themselves.

Wood also represents impact-resistant biological materials as shown in Figure 1.9. It comprises non-mineralized biopolymers, but like bone, has hierarchical porosity and both soft and hard phases. Wood is distinguished from other plant materials by thickened cell walls of cellulose, hemicellulose, and lignin which allow it to efficiently bear the load and convey water and nutrients. While some trees have evolved to bear dynamic loading (as discussed later), impact resistance or toughness is primarily identified by millennia worth of human use rather than natural adaptations. In everything from baseball bats to gunstocks, wood from trees such as ash, walnut, maple, and others have been long prized for their impact resistance as shown in Figure 1.9. The translation of this accumulated cultural knowledge into rigorous engineering principles is still ongoing.

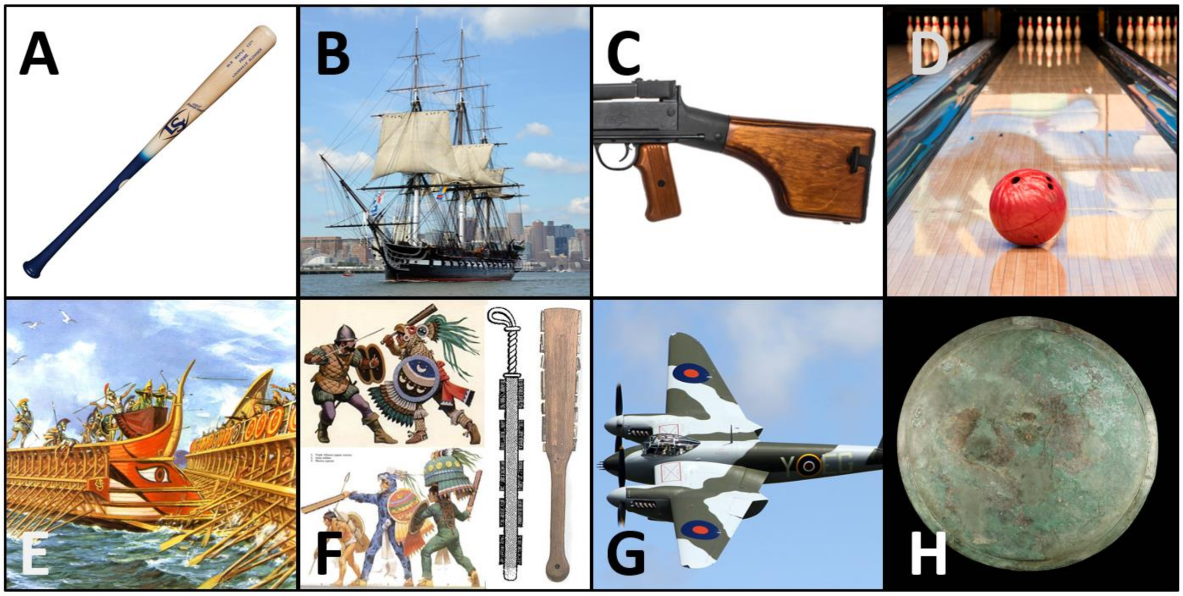

Figure 1.9. Various applications of impact resistant wood. (a) Louisville Slugger made of white ash [94], (b) USS Constitution ("Old Ironsides") made of white and southern live oak [95], (c) Degtyaryov hand-held machine gun stock made of walnut [96], (d) bowling alley flooring made of pine [97], (e) Ancient Greek trireme made of cedar [98], (f) Aztec broadsword (macuahuitl) made of southern live oak [99], (g) DH-98 "Mosquito" bomber made of plywood and balsa [100], and (h) Ancient Greek hoplon shield made of a poplar or willow core with 0.5 mm bronze cover [101].

1.7 **Horns and hooves of tetrapod mammals (keratin)**

In many cases, non-mineralized biopolymers are evolved in nature to reduce weight compared with the mineralized tissues. Although soft, these non-mineralized biopolymers are impact-resistant, such as keratin, cellulose, and chitosan. Keratin is a key structural protein produced in certain epithelial cells existing in hair, horns, hooves, feathers and skins. Keratin is a dead tissue that is not vascularized, which means it cannot be remolded or regrow once damaged. Most keratinized materials are made of polygonal cell tiles (tens of microns in diameter, several microns thick) that overlap laterally and are stacked on top of each other to form a relatively dense layer as shown in Figure 1.10. The average Young's modulus of bighorn sheep horn in ambient dry condition (~10 wt.% H_2O) is ~3.5 GPa, while ~1.5 GPa in fully hydrated condition (~30 wt.% H_2O) at an impact strain rate ~10^3 s^{-1} [98]. Keratin materials tend to be more ductile in hydrated states. Bighorn sheep horn can sustain ~60% tensile strain in a fully hydrated condition, but only less than ~5% in dry condition due to a brittle fracture [57, 102]. The fracture toughness of hoof shows a maximum value (22.8 KJ/m^2) at an intermediate hydration state, which is a two-fold increase over both dry and fully wet condition [29]. Thus, it can be found in terms of a good energy absorption or impact resistance, keratin materials should have an ideal water content, neither too dry nor too wet. Water can decrease the stiffness and strength of keratin materials dramatically but on the other hand, can increase the ductility. This is due to the water molecules break the hydrogen bonds in the amorphous matrix thus increase the protein mobility [45, 103].

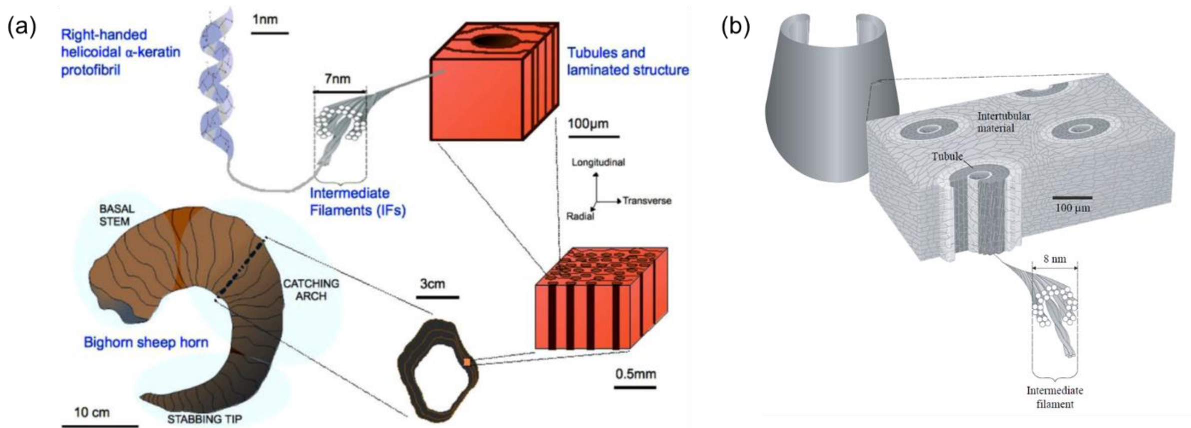

Figure 1.10. Hierarchical structure comparison of horn and hoof: (a) Hierarchical structure of horn from macro- to nano-structure. Tubular and laminated structure is showed in the micro- scale; (b) Tubules and intertubular materials in hoof wall. Keratinized cell arrangement changing from tubular to intertubular matrix. Intermediate filaments found in the keratinized cells. Figures adapted from [57, 58].

Horn and hoof show a similar hierarchical structure which has been considered playing an important role in both energy absorption and impact resistant as shown in Figure 1.10a [4, 104]. At the micro scale, tubules and the intertubular matrix consisting of lamellar stacked keratin cells have been observed in both horns and hooves in various studies as shown in Figure 1.10b [57, 105-107]. Elliptical tubules with average major axis 100 um and a minor axis 40 um were identified in bighorn sheep horn, playing anisotropic mechanical behavior in different directions [47, 57]. Tubule buckling and delamination occurred when the compressive load was applied parallel with the tubules, while tubule closure occurred when compressed in the perpendicular direction. The tubules served as a reinforced structure that enhance the stiffness as well as the strength in the longitudinal direction, which is parallel to the tubules in both tensile and compressive tests, while the closure of tubules in radial direction helps absorbing more energy [57].

Chapter 1, in part, is currently being prepared for submission for publication of the material. Wei Huang, David Restrepo, Pablo Zavattieri, Jae-Young Jung, Zengqian Liu, Robert O. Ritchie, Joanna McKittrick, and David Kisailus. The dissertation author was the primary investigator and author of this material.

CHAPTER 2: THE WOODPECKER HEAD

2.1 Introduction

On top of the previous studies and the knowledge about impact-resistant biological materials reviewed and introduced in Chapter 1, the following chapter will discuss how the woodpeckers avoid brain injury further in detail, focusing on structural and mechanical properties of the hyoid apparatus, the skull bone, and the interspecies variation of the skull bone in woodpeckers and its potential effect on the energy dissipation.

The woodpecker head is composed of two types of materials: hard and soft tissues. For the hard tissue, it refers to a mineralized composite material with collagen and other organic polymers, mainly found in the bones. The woodpecker skull bone [108, 109], the upper and lower beak bone [46, 110-114], and the hyoid bone [115-117] were discussed in previous studies. In addition, a keratinized sheath (called the rhamphotheca) is found in the upper and lower beak [46, 110-113].

In the woodpecker head, there are both mineralized and non-mineralized materials. The beak and skull bones are highly mineralized to get enough stiffness to support the skeletal structure and to protect internal organs. For example, the skull bone wraps around the brain, which is one of the most important organs in living animals. The degree of mineralization may vary on applied local stresses and/or forces. If the applied forces or stresses are relatively high, then, it implemented the higher degree of mineralization on the materials by depositing more Ca. Specifically, the cortical bones of the woodpecker beaks have higher Young's moduli up to 30 GPa [110] but the trabeculae bone has lower Young's moduli from 0.5 ~ 10 GPa [118].

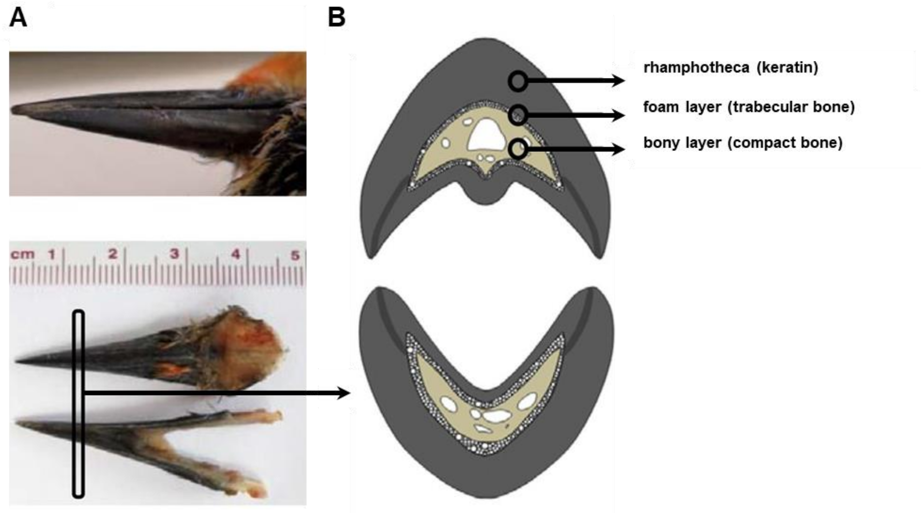

Figure 2.1. The beaks of woodpeckers. (a) Photos of the upper and lower beaks of a male red-bellied woodpecker and (b) a schematic of the transverse cross-sectional view, adapted from [110].

Within the woodpecker head, some examples of mineralized materials are the skull bone, upper and lower beak bone, and hyoid bone. These structures are mainly composed of minerals (hydroxyapatite), mineralized structural proteins (type I collagen), and water (and/or gas). The mineralization is the most important strategy to protect animal's weak internal organs and tissues from external forces or piercing objects. In contrast to the bones, the rhamphotheca is only composed of a single phase protein, β-keratin [110, 111]. As non-mineralized materials, the keratinized outer sheath of the upper and lower beak, and the sheath of hyoid apparatus are compliant than the mineralized, structural bones. In the beaks, the keratinized rhamphotheca can be considered as the first material to get an impact force because of its anatomical location as shown in Figure 2.1a. Therefore, this material needs to be stiff enough to make a hole at the tree trunk but tough (damage-resistant) enough to avoid any catastrophic failures or internal cracks.

The pecking motion of woodpeckers is also obtained by the contraction and retraction of the neck and body muscles, which actively consume energy synthesized by living organisms. This active motion can be consciously modulated by an interactive control decided by woodpeckers. On top of that, as the viscoelastic materials, the muscles can directly help convert the stored kinetic energy from its head to the dampened elastic energy on the beaks after a few seconds of the moment of impact.

2.2 Multi-scale hierarchical structure

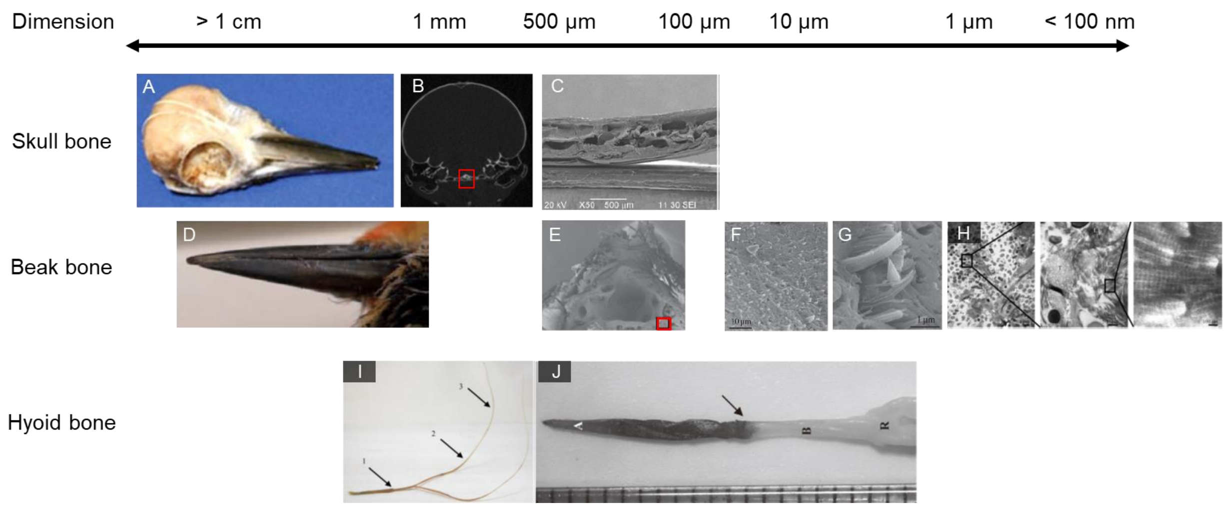

Figure 2.2. Examples of multi-scale hierarchical bone structures of the woodpecker head. (a-c) The skull bone of a great-spotted woodpecker adapted from [109, 119], (d-h) the beak bone of a red-bellied woodpecker adapted from [41], and (i and j) the hyoid bone of a woodpecker adapted from [117] and [120].

The structures of skull bone, beak bone, and hyoid bone of woodpeckers presented as shown in Figure 2.2. As it was discussed earlier, the woodpecker skull bone shows a sandwich-like double wall layered structure (Figure 2.2a-c) [113].

The beak bones of woodpeckers show a multi-scale hierarchical structure like other structural bones. These structural bones show a dense and highly mineralized outer frame as well as a lighter and network-like woven foam structure inside to make blood and body fluids. Similar to those of structural bones in mammals, Figure 2.1 and Figure 2.2d-h show the structure of the beak bone of woodpeckers [110]. At macroscale, it showed a foam-like thin, woven sponge bone inside and a thick, dense cortical core bone outside (Figure 2.2d). It also shows a typical osteon structure, which is stacked layers of lamellae bone. At the microscale, micro pores from lacuna space in the matrix of osteons and mineralized collagen bundles are visible [110]. At the nanoscale, it shows a typical 67 nm of collagen gap band, which is a symbol of type I collagen found in structural bones as shown in Figure 2.2h (right most) [52].

The hyoid apparatus is common in mammals and avian species but the long and elongated hyoid apparatus (the aspect ratio of cross-sectional area to the diameter can be reached up to 3.89 [117] can be only found in woodpeckers and hummingbirds, as shown in Figure 2.2i. The hyoid apparatus is composed of the core bones inside and the keratinized outer sheath at the tip (Figure 2.2j).

The rhamphotheca of the woodpeckers utilizes a multi-scale hierarchical structure at different length scales although it is made of a single-phase protein. At macroscale, black-colored keratinized sheath fully covers the internal core bone structures. At the microscale, the individual dead keratin cell stacks build up along the impact direction (perpendicular to the dead keratin cell layer stacks). At the nanoscale, different wavy suture structures can be found in different avian species with a definition of waviness (the ratio of height to width), for example, 1 for the beaks of woodpeckers while 0.3 and 0.05 for the chicken and toucan beaks, respectively [110]. In the beak rhamphotheca, interestingly, no pores are found at any length scales. This is a somewhat unique aspect of keratin structures found in avian beaks compared to the other keratinized materials, for example, the horns and hooves of a tetrapod

2.3 **Multi-phase of materials**

The bones in the woodpecker heads are composed of typical bone materials: mineral, protein, and water/air. Using a combination of these three phases, the head can successfully support its skeleton and protect the internal organs. Unlike other structural bones, the skull bone of birds and some mammals utilize the air as its filler of inside space of bones to reduce the total body weight to maintain its flight ability or to save the energy. In some woodpecker studies, there are some reports that the skull bone of woodpeckers demonstrates that it has a sandwich-like double layer structure [121], filled with the air, so-called, pneumatic bone, which commonly found in birds and mammals. This meant that the skull bone has already specially designed structures to protect the most important organs in our body. On top of that, due to the woodpecker's pecking habit, the additionally optimized proportion between the pneumatic bone, to reduce the weight, and the compact bone, to support its skeleton, is required. The properties can be identified using a bone morphometry analysis by measuring the tissue volume/bone volume to quantify the porosity as well as the relative density, relative stiffness. Beak bones are similar to other typical structural bones that show a dense, highly mineralized compact bone as well as a small portion of a woven network-like trabecular bone. Lee et al. [110] described the area fraction of each phase/material to calculate the aggregate hardness and modulus as a similar concept of bone morphometry analysis. The authors described the structure-property relationship by applying the area fraction with a common concept of the rule of mixture. In the rhamphotheca, the keratin is a single component material of the beak and the hyoid bone. It has only two phases, keratin matrix/fibers and the air (or void space). The fraction of keratin and void space determined the porosity of the materials, which is an important characteristic of impact-resistant materials to absorb energy.

There is a certain meta-phase at the interfaces between the mineralized bone tissue and non-mineralized keratinized layers in the avian beaks. This is very similar to the example of dentin and enamel junction found in the mammal tooth reported by Imbeni et al. [122]. The authors found that the existence of the dentin-enamel junction (DEJ) at the interface between the dentin and outer enamel coating create a pathway of cracks when it went through the tougher material phase (e.g., the mantle dentin adjacent to the interface). Because of the phase differences between the mammal tooth and the avian beaks due to the lack of mineralization in the keratinous materials in the avian beak, a similar crack arresting mechanism might be happening at the interface between the bone and keratinous materials. This is an interesting topic that needs to be further investigated in the future.

2.4 Multi-properties: mechanical impedance mismatch

Individual mechanical properties of each part of the woodpecker heads are quite versatile because of its complex multi-scale structures as well as its multi-phase of different material constituents. For example, the beaks of woodpeckers are not only consisting of different materials (e.g., a mineralized bone tissue and a keratinized rhamphotheca as shown in Figure 2.1b) but also different mechanical properties on its beak as shown in Figure 2.3a [110]. The Young's moduli and microhardness of the beak bones were 30.2 GPa and 0.64 GPa, respectively, while those of the beak rhamphotheca were 8.7 GPa and 0.32 GPa, respectively, [110]. Moreover, the beak showed three different layers, such as the bony layer (the stiffest), the rhamphotheca layer (the most compliant), and the foam layer (in between). The author measured the Young's moduli of the rhamphotheca layer as a range of 7.6 ~ 9.8 GPa, these values are much lower than the Young's moduli of the bony layer [110]. The gradient of this mechanical property between the adjacent two different materials helps to dissipate internal stress [5].

The elastic modulus of the skull bones was reported by Wang et al. as a 0.31 GPa through a numerical estimation, but the experimental results (Figure 2.3b) generally tend to show the higher range from 4.0 ~ 8.4 GPa through a tensile test and 8.6 ~ 11.0 GPa through a nanoindentation test, respectively [109, 114]. The measured Young's moduli at different locations of the woodpecker skull bone and the benefit of having gradient material properties were identified by Wu et al. [123] by applying a model of stress wave propagation in a viscoelastic bar, concluding that having this variation makes the peak stress on the skull bone remained minimized at the location nearby the brain as shown in Figure 2.3b and Figure 2.3c [123].

The mechanical impedance mismatch can be also found in the hyoid bone in woodpeckers. The first measured Young's modulus of the hyoid bone through a tensile test reported by Zhou et al. was 1.3 ~ 3.7 GPa [117]. The combination of two gradient directions in the transverse and longitudinal cross-section can be beneficial; Lee et al. [115] also reported that the geometric effect of the hyoid apparatus and the hyoid bone can mitigate the stress wave propagation by utilizing the adjacent muscle tissues as making lateral displacement mainly due to the viscoelastic dampening effect (Figure 2.3d-f).

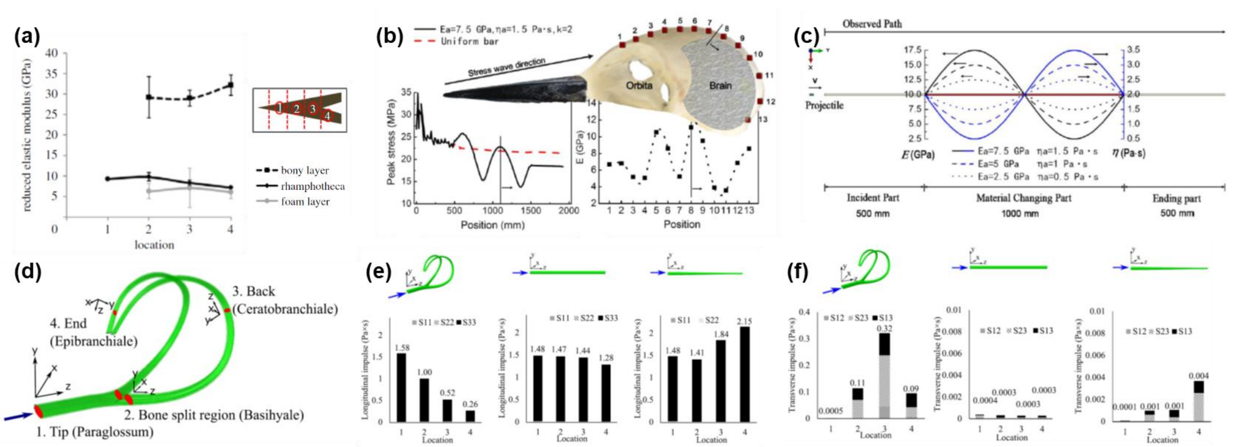

Figure 2.3. Mechanical properties of the woodpecker head. (a) Reduced elastic modulus of the lower beak rhamphotheca at different locations, adapted from [110]. (b) A comparison between the peak stress curve of viscoelastic bar model from a simplified finite element analysis (left) and the measured Young's moduli along the different locations (right, numbered), adapted from [123]. (c) A model of stress wave propagation in a simplified viscoelastic bar, taken from [123]. (d) The model geometry of the hyoid apparatus for a finite element analysis on impact analysis (ref), (e) the plots of the longitudinal impulse of each normal stress component at each location (1-4), and (f) the plots of the transverse impulse of each shear stress component at each location (1-4), adapted from [115].

Chapter 2, in part, is currently being prepared for submission for publication of the material. Wei Huang, David Restrepo, Pablo Zavattieri, Jae-Young Jung, Zengqian Liu, Robert O. Ritchie, Joanna McKittrick, and David Kisailus. The dissertation author was the primary investigator and author of this material.

CHAPTER 3: STRUCTURAL ANALYSIS OF THE TONGUE AND HYOID APPARATUS IN A WOODPECKER

3.1 Introduction

Woodpeckers (family *Picidae*) are found in forested areas worldwide, except in Australia and surrounding areas. They feed by pecking (tapping or drumming) into wood and using their tongue to extract insects or sap. They have strong tail feathers, which are used as a lever during pecking and zygodactyl feet that help them balance. The extreme conditions during pecking include head speeds up to 7 m/s, a deceleration up to 1,200 g and pecking rates of 20 times per second, which occur without sustaining concussions or brain damage [30].

One adaptation in woodpeckers is the unusual structure of its hyoid apparatus [124]. The hyoid apparatus in birds consists of the tongue bones along with associated connective tissues (cartilage, and soft tissues such as muscles, dermis and epidermis). The primary function of the hyoid apparatus is to anchor and allow for the extension of the tongue [125]. However, considering the extreme conditions experienced by the entire head during pecking, this structure must be capable of effectively dissipating energy to avoid failure.

In most birds, the hyoid apparatus consists of five distinct bones: the paraglossal, basihyal, urohyal, paired ceratobranchial, and paired epibranchial (Figure 3.1a-c, for a domestic chicken (*Gallus gallus*)) [125]. Between the different bones, there are joints that provide for the motion required during feeding. In contrast to the chicken, the structure of the hyoid apparatus in a red-bellied woodpecker (*Melanerpes carolinus*, shown in Figure 3.1d), is elongated and wraps around the skull from the rostral (toward the beak) to the caudal (toward the terminal end). In the woodpecker the epibranchial bones are much longer than in most other birds (as seen by comparing Figure 3.1c and e), terminating in the supraorbital ridge between the orbits (eyes), as opposed to the occipital bone (base of the cranium) [30, 54, 119, 126]. In Figure 3.1c and e, the epibranchial bones make up 37% and 61% of the entire length of the hyoid bones in chickens and woodpeckers, respectively. These measured ratios show that the length of the epibranchial bone in woodpeckers is relatively much longer than in chickens.

The urohyal bone is absent in woodpeckers. Bock [54] found that the hyoid apparatus had a bony core structure, which was surrounded by muscles. Figure 3.1e depicts a lateral view, where the bones are identified along with the joints that exist between the paraglossal-basihyal, basihyal-ceratobranchial, and ceratobranchial-epibranchial bones. Bock [54] also described anatomical features (i.e., different cross-sectional shapes of the bones along with their positions), but did not investigate their functional or structural relationships. The structural role and function of the urohyal bone in parrots was briefly introduced by Homberger [127] as an attachment point to support adjacent tissues (larynx, cartilage, ligament and muscle). However, it is unclear why this particular bone is absent in the woodpecker.

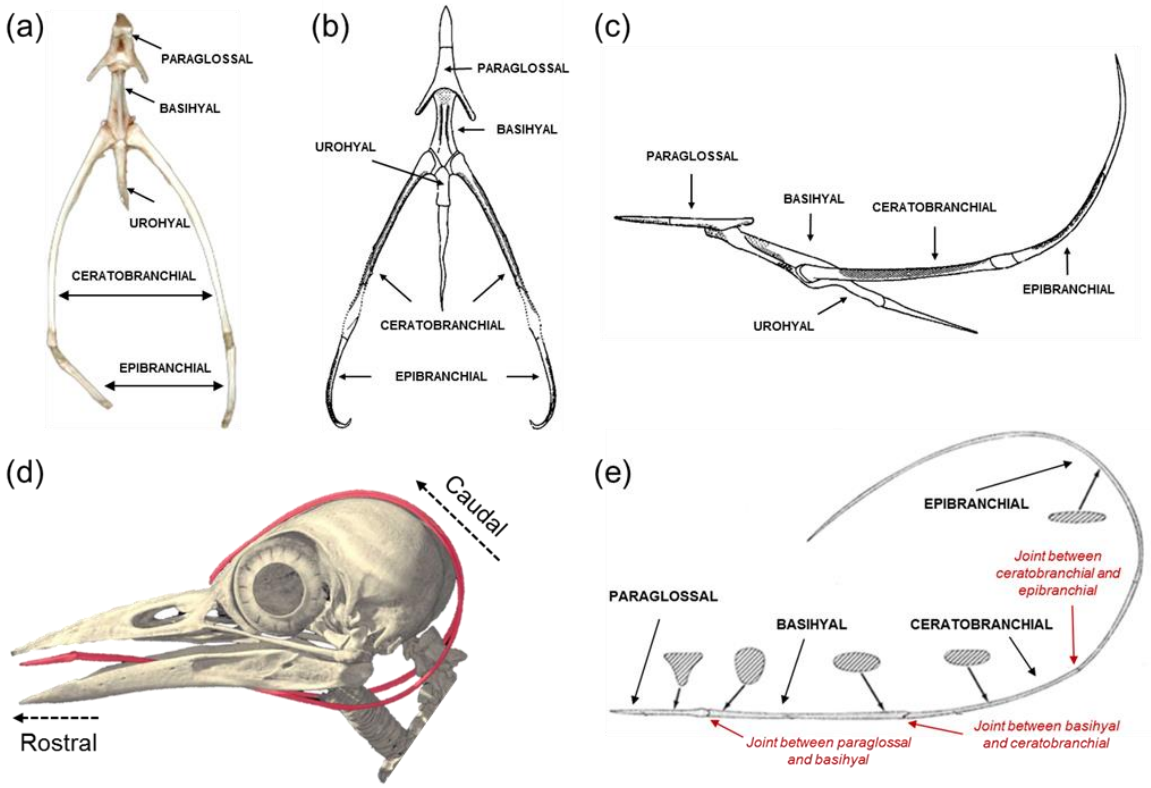

Figure 3.1. Bones in the bird hyoid apparatus. (a) Photograph (dorsal view) of the hyoid bones of a domestic chicken (*Gallus gallus*). Taken from [51]. (b) Schematic diagram of the dorsal view showing the paraglossal, the basihyal, the urohyal bone, and the paired ceratobranchial and epibranchial bones in a domestic chicken. Adapted from [3]. (c) Lateral view of the hyoid bones of a chicken. Adapted from [3]. (d) Lateral view of a red-bellied woodpecker (*Melanerpes carolinus*) skull with the hyoid apparatus colored in red. Taken from [52]. **(e)** Lateral view of the hyoid bones of a red-bellied woodpecker that highlights the bones and joints. The change in cross-section of the bones along the length is indicated. Adapted from [5]. Note: the epibranchial bone is ~1/3 of the total length of the hyoid bone in chickens, but is ~2/3 of the total length in woodpeckers. Scale bars were not provided in the references for (c) and (e).

The woodpecker's unique ability to avoid traumatic brain injury has led researchers to investigate energy absorbing mechanisms in its skull. As has been demonstrated for metallic biomaterials [128], investigations of the relationship between structure and mechanical properties can provide insight into the holistic nature of materials. To this end, several anatomical features have been attributed to energy absorption, including a small brain size and mass when compared to surface area, the short impact duration of pecking and the small volume of cranial fluid [30, 121, 129]. Strong neck muscles provide protection from injury caused by rotational forces [129]. A previous study of the relationship between structure and mechanical properties of the beak of woodpeckers revealed that the lower porosity found in the bony layer strengthens the beak for pecking [110]. In addition, the sponge-like bone structure within the upper beak and the more plate-like cranial bones (both absent in non-pecking birds) may also contribute to the energy absorption [119, 129, 130]. A quantitative bone morphometry analysis of woodpecker skull bones was conducted by Wang *et al.* [109], suggesting that this structural parametric analysis might be useful for comparative study of different species of birds. In a comprehensive review paper [131], the mechanisms that provide impact resistance to the woodpecker's head were discussed, that include woodpecker-inspired shock-absorbing applications. However, information on the hierarchical structure of the hyoid apparatus is not yet understood.

Reports on the potential ability of the hyoid apparatus to withstand impact have focused upon its potential to aid the skull in avoiding brain injuries and have relied upon numerical and finite element analyses [116, 119, 130, 132-134]. Oda *et al.* [132] determined that the presence of the hyoid bones may lower the compressive and tensile stresses in the brain up to 40% during pecking. Wang *et al.* [119] suggested that the three most important factors for shock absorption are: 1) the macro/micro structures of the head, including the hyoid apparatus, 2) the uneven plate-like trabecular bones in the cranium, and 3) the unequal lengths of the upper and lower beak. The hyoid bone was also suggested to play the role of a 'seat belt' after impact [119]. Yoon *et al.* [133] mimicked the head for application in devices that experience high-***g*** and high-frequency mechanical forces by using a simplified mechanical vibration model that simulated the head as a damper and spring. They reported that the woodpecker-inspired shock-absorbing system showed a 1% failure rate at 60,000 ***g***'s, compared to a hard resin shock-absorbing system, which showed 26% of failure. Zhu *et al.* [134] performed a numerical study for the impact response of the head and reported that stress waves propagated from the upper bill to the posterior of the skull. It was concluded that the stress wave was decreased by two structural features: 1) having the skull wrapped with the hyoid apparatus and 2) the viscoelastic energy absorption of the biological tissues. In addition, the function of the hyoid bone was computationally assessed by Liu *et al.* [116] who found that there was 30% less deformation of the whole head with the hyoid bones than without them. They concluded that the hyoid bone and muscle contributed together to increase the rigidity of the whole head, reducing the deformation and oscillation of the skull.

When solely considering the hyoid apparatus, initial mechanical properties were reported and based on tensile tests including both bone and soft tissues [117]. It was determined that the elastic modulus and tensile strength were 1.3 GPa and 76.0 MPa, respectively, at the joint between the paraglossal and basihyal bone [117]. In the epibranchial bone, the elastic modulus and tensile strength were 3.7 GPa and 92.0 MPa at the rostral position and 1.7 GPa and 131.0 MPa in the midsection [117]. The higher modulus and lower strength of the rostral end of the epibranchial bone compared to the midsection were attributed to the amount of soft tissue surrounding the bone. Because the diameter of the hyoid apparatus is relatively constant along the epibranchial bone, it is possible that there is a thinner sheath of soft tissue surrounding the bone at the rostral end and a thicker sheath at the midsection, which would result in an increased bone diameter at the rostral end compared to the midsection.

The interpretation of the results of the previous studies [116, 117, 119, 132-134] on the hyoid apparatus used the term “hyoid bone” instead of “hyoid apparatus” (or sometimes “lingual apparatus” [125]). As a result, the previously acquired mechanical properties and numerical simulation results on the “hyoid bone” were based on the properties of bulk hyoid apparatus. Here, we distinguish the difference between the individual hyoid bones and the hyoid apparatus.

The objective of this study is to specifically analyze the morphological and structural features and associated mechanical properties of the hyoid bones of acorn woodpeckers (*Melanerpes formicivorus*) to examine the structure/mechanical property relationships that allow it to avoid failure during the extreme conditions of pecking. Livingston [124] observed that the woodpecker tongue showed fascinating aspects of adaptable design in nature by linking structure and function. By using sophisticated analytical techniques, the structure of the woodpecker hyoid apparatus can be more accurately assessed. The results of this study have implications for the design of engineered structures, such as impact-absorbing protective headgear for athletes and the military.

3.2 Experimental

3.2.1 Sample collection and preparation

This study was conducted under the approval of animal care and use program by Institutional Animal Care and Use Committee (IACUC) at University of California, San Diego (Tissue Permit Number: T14068).

Three adult acorn woodpeckers were donated soon after death from a northern California ranch. These were immediately frozen and kept in a frozen state during transportation to the lab. All samples were stored in a freezer at -20˚C. The woodpeckers were gradually thawed at room temperature for 30 min before performing other tests. All tests were performed under ambient conditions (25˚C, 60% relative humidity).

3.2.2 X-ray Micro-computed tomography (μ-CT) and three-dimensional reconstruction

The whole birds were scanned by X-ray micro-computed tomography (μ-CT, SkyScan 1076, Bruker microCT, Kontich, Belgium) with a rotation step of 0.7º, an exposure time of 1600 ms, a 100kV acceleration voltage, and an isotropic voxel size of 36.00 μm. The heads were scanned with an isotropic voxel size of 9.06 μm, while the other scan parameters were the same as for the whole birds. In addition, high-resolution μ-CT (HR-μCT, MicroXCT-200, Xradia, Pleasanton, CA) was used for imaging small pieces (5mm x 5 mm x 2 mm) of each hyoid bone with a 0.916 μm voxel size at a 40kV acceleration voltage. The rotation angle and tilt increment were 360° and 0.2°, respectively. The images and three-dimensional reconstructed models were developed using the software programs CTvox and Dataviewer (Bruker microCT, Kontich, Belgium) and XMReconstructor (Xradia, Pleasanton, CA). Image J software (National Institutes of Health, Bethesda, MD) was used upon orthoslice images of the heads to calculate the cross-sectional area and dimensions of the hyoid bone at varying positions along its length. Each dimension was measured at least six times and the mean values were calculated.

Each hyoid bone was selected for visualization and analyzed using Amira software (FEI Visualization Sciences Group, Burlington, MA). After the reconstruction, cross-sectional dimensions were determined by creating triangle mesh models saving them into the extension format of the virtual reality modeling language.

3.2.3 **Microscopic evaluation and chemical composition**

Two birds were thawed for dissection and subsequent excision of the hyoid apparatus. Each was submerged immediately into a 2.5 vol.% glutaraldehyde solution for 24 hours for tissue fixation. After that, they were dehydrated in increasing concentrations of ethanol: 30%, 50%, 70%, 90%, and 100% (vol.%) for 10 min each and then dried by a critical point dryer (Autosamdri 815A, Tousimis, Rockville, MD). After the dehydration process, the hyoid apparatus was cut along the transverse and longitudinal planes and divided into several pieces. Two separate sets of samples were prepared for the microstructural analysis and the nanoindentation test from each piece. Samples for the nanoindentation test were embedded in an epoxy resin and cured overnight at room temperature. Embedded samples were cut into smaller pieces using a jeweler's saw and both sides were polished using a series of SiC paper with average particle sizes of 35 µm and 15.3 µm, followed by fine polishing with an alumina powder media down to 0.05 µm to provide a mirror finish. Optical micrographs were obtained by a light microscope (VHX1000, Keyence, Osaka, Japan) to visualize the color and shape of each tissue without any staining. These samples were used for nanoindentation tests first and then sputter coated with iridium (K575X, Emitech, Fall River, MA) at 85µA for 10 sec. Samples for the microstructural analysis were also coated with iridium without epoxy. Scanning electron microscopy (SEM) and energy dispersive X-ray spectroscopy (EDS) were performed (XL30 UHR-SEM, FEI Company, Hillsboro, OR and Inca, Oxford, Abingdon, Oxfordshire, UK) at 15keV for the prepared samples individually. Another SEM device (XL30 ESEM, FEI Company, Hillsboro, OR) with a back-scattered electron (BSE) detector was utilized to highlight atomic mass contrast within the tissues. In addition, the elemental composition was acquired from the cross-sections near the nanoindentation sites to investigate the relationship between mineral stoichiometry (i.e., calcium to phosphorus ratio (Ca/P) and mechanical properties. The EDS spectra at each indent were obtained at least three times to determine the average and standard deviation.

A dried sample from the lingual apex and body were tested separately as a whole piece by thermogravimetric analysis (TGA) (SDT Q600 TGA, TA Instruments, New Castle, DE) at a ramp rate of 10˚C/min and a range of 20~600˚C, following a previously reported procedure [135] to determine the amount of water, mineral, and protein. A polished cross-sectional sample of the lingual apex was analyzed by Fourier transform infrared (FTIR) spectroscopy (Equinox 55, Bruker Optics, Billerica, MA). The spectral range was 400-4000 cm^{-1} with a 4 cm^{-1} resolution. The scan number was 1024 in reflection mode. The background signal was collected in transmission mode through air.

3.2.4 **Nanoindentation**

The hardness and elastic modulus were acquired by nanoindentation (TI 950 TriboIndenter, Hysitron, Minneapolis, MN) with a diamond cube corner tip on polished cross-sectional pieces of four different hyoid bones. Indentation mapping was carried out with displacement controlled indents to a maximum depth of 500 nm. A trapezoidal load function consisting of a 5 s loading segment, a 2 s hold, and a 5 s unloading segment was used. Indents were arranged in square arrays, spaced either 20 or 30 μm apart. A fused quartz standard sample from Hysitron was used to calibrate the tip area function for the diamond cube corner tip. The tests were performed at least ten times for each sample and the average value and standard deviation were calculated. The hardness (H) is given by:

$$H = \frac{P_{\text{max}}}{A_c} \tag{3.1}$$

where P_{max} is the maximum load (in N) and the A_{c} is the projected area of the indenter at peak load computed from the area function, $A_{\text{c}} = F(h_{\text{c}})$, where h_{c} is the contact depth [136]. For a cube corner tip indenter, the area function $A_{\text{c}} = 2.598h_{\text{c}}^2$. The slope of the initial unloading load-displacement curve, $S = \frac{dP}{dh}$, was used to calculate h_{c}:

$$h_{\text{c}} = h_{\text{max}} - \frac{3P_{\text{max}}}{4S} \tag{3.2}$$

where h_{max} is the maximum displacement. The reduced elastic modulus, E_{r}, is given by:

$$E_{\text{r}} = \frac{\sqrt{2}}{2}\frac{S}{\sqrt{A_{\text{c}}}} \tag{3.3}$$

The Young's modulus, E, was obtained from:

$$\frac{1}{E_{\mathrm{r}}} = \frac{1 - v^2}{E} + \frac{1 - v_{\mathrm{i}}^2}{E_{\mathrm{i}}}, \tag{3.4}$$

where E_{i} and v_{i} are the Young's modulus (1,140 GPa) and Poisson's ratio (0.07) of the indenter [137] and v is the Poisson's ratio of the tested sample (taken as 0.3) [138]. The test sites (basihyal, ceratobranchial and epibranchial) were determined after confirming the macro/micro structure of these bones and all indents were performed on the transverse cross-sections. Details of nanoindentation test specimens are listed in Table 3.1.

3.2.5 **Statistical analysis**

One-way ANOVA analyses were used to identify statistically significant differences of the Young's moduli among the different hyoid bones [139]. In addition, a multiple comparison test was conducted by Tukey's least significant difference procedure, which is valid if the preliminary test (the one-way ANOVA F-test) shows a significant difference [140]. A paired sample t-test was used to compare statistically significant differences of the Young's moduli between the two different bone regions for each hyoid bone. The criterion for statistical significance was $p < 0.05$ for both the ANOVA and the t-test.

3.3 **Results and Discussion**

3.3.1 **Macroscale structure**

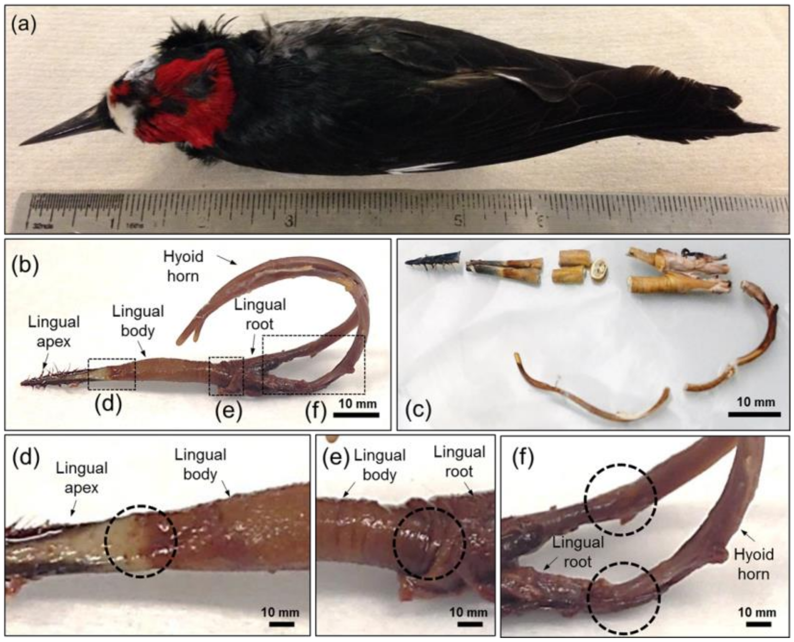

Figure 3.2. (a) Photograph of an acorn woodpecker. (b) The dissected hyoid apparatus. (c) The dried and sectioned samples of the hyoid apparatus in transverse and longitudinal planes. Magnified photographs of the three joint locations in the hyoid apparatus between (d) the lingual apex and body, (e) the lingual body and root, and (f) the lingual root and the hyoid horn.

Figure 3.2a shows a photograph of an acorn woodpecker with an overall length and width of ~216 x 51 mm and a head length, width and height of 57.8 x 15.4 x 27.9 mm. Figure 3.2b shows a photograph of the dissected hyoid apparatus. The hyoid apparatus is composed of four different regions: the lingual apex, lingual body, lingual root, and hyoid horns, which are connected along its sagittal plane from rostral to caudal positions [141]. The paraglossal and basihyal bones are located inside the lingual apex and body, respectively. The caudal end of basihyal bone, the rostral end of ceratobranchial bones, and their connecting joint are located at the lingual root. The hyoid horns contain the ceratobranchial and epibranchial bones along with their joint. Figure 3.2c shows dried and sectioned pieces that were used for further analysis. The barbed tips at the lingual apex are clearly visible in Figure 3.2b and c (black). The lingual body has the largest diameter. Figure

3.2d-f show the magnified images of the interfaces between the lingual apex and body (Figure 3.2d), the lingual body and root (Figure 3.2e), and the lingual root and hyoid horn (Figure 3.2f), which surround the three joints in the hyoid apparatus.

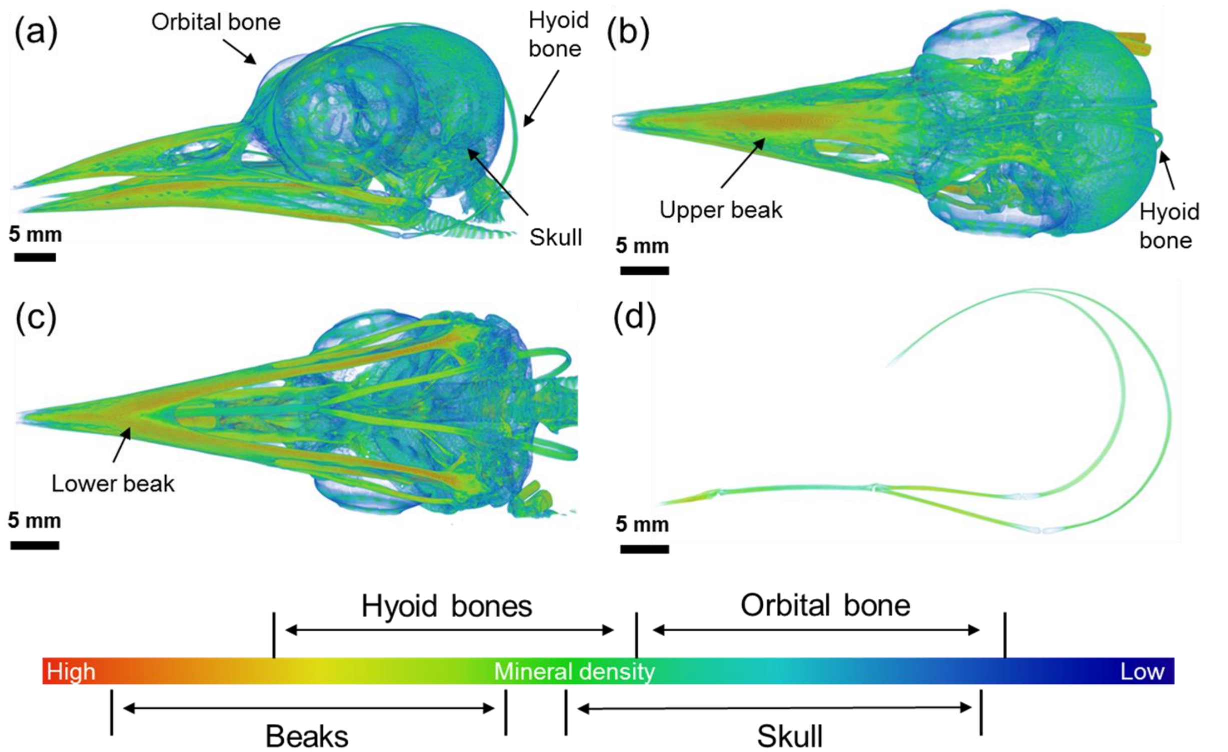

Figure 3.3. Micro-computed tomography images of the head structure of an acorn woodpecker at different orientations. (a) Left lateral view, (b) dorsal view, (c) ventral view, and (d) lateral view of the hyoid bones. A color scale is shown to indicate the gradient in color (that is associated with mineral density) from the highest density in red to lowest density in dark blue. This shows that the hyoid bones are relatively denser than the skull.

Figure 3.3 shows μ-CT reconstructed images of the head. The hyoid bone wraps around the head, from the rostral end at the beak to the supraorbital ridge between the two orbits. Some woodpeckers with long probing tongues have even more elongated hyoid horns that can pass through the right nasal cavity and upper jaw (as is the case for the European woodpecker (*Picus viridis*)) or can circle the right orbital bone (as is the case for the North American hairy woodpecker (*Picoides villosus*)) [54]. The acorn woodpecker's hyoid horns are less elongated than these two species, which is likely due to a specialization for either drilling or probing functions [54].

The color distribution in Figure 3.3 reflects the X-ray intensity profile based on the normalized material density, ranging from the highest density (red), middle-range density (higher $\rightarrow$ lower: yellow $\rightarrow$ green $\rightarrow$ light blue) to the lowest density (dark blue). The density is correlated with the amount of mineral: red having the highest mineral content and dark blue having the lowest. Figure 3.3a illustrates that the inner part of the upper (maxilla) and lower (mandible) beak showing the highest mineralized area, which are the bones in the beak. The hyoid bones show mid-range of densities (Figure 3.3a-d). The skull and orbital bones have low to mid-range densities (Figure 3.3a-c). An interesting point is that the beak and hyoid bones have a higher mineral density than the cranial bones. The beak bone is more mineralized, which should lead to a relative increase in strength and stiffness. This could be to reinforce the beak and hyoid apparatus during the impacts from pecking. The mineral density of the hyoid bones varies along their sagittal plane, having a slightly higher mineral density in the paraglossal and ceratobranchial bones than in the basihyal and epibranchial bones. X-ray transparent regions are found between the bones, indicating the presence of soft material in the joints; these observations are discussed later.

3.3.2 **Microscale structure**

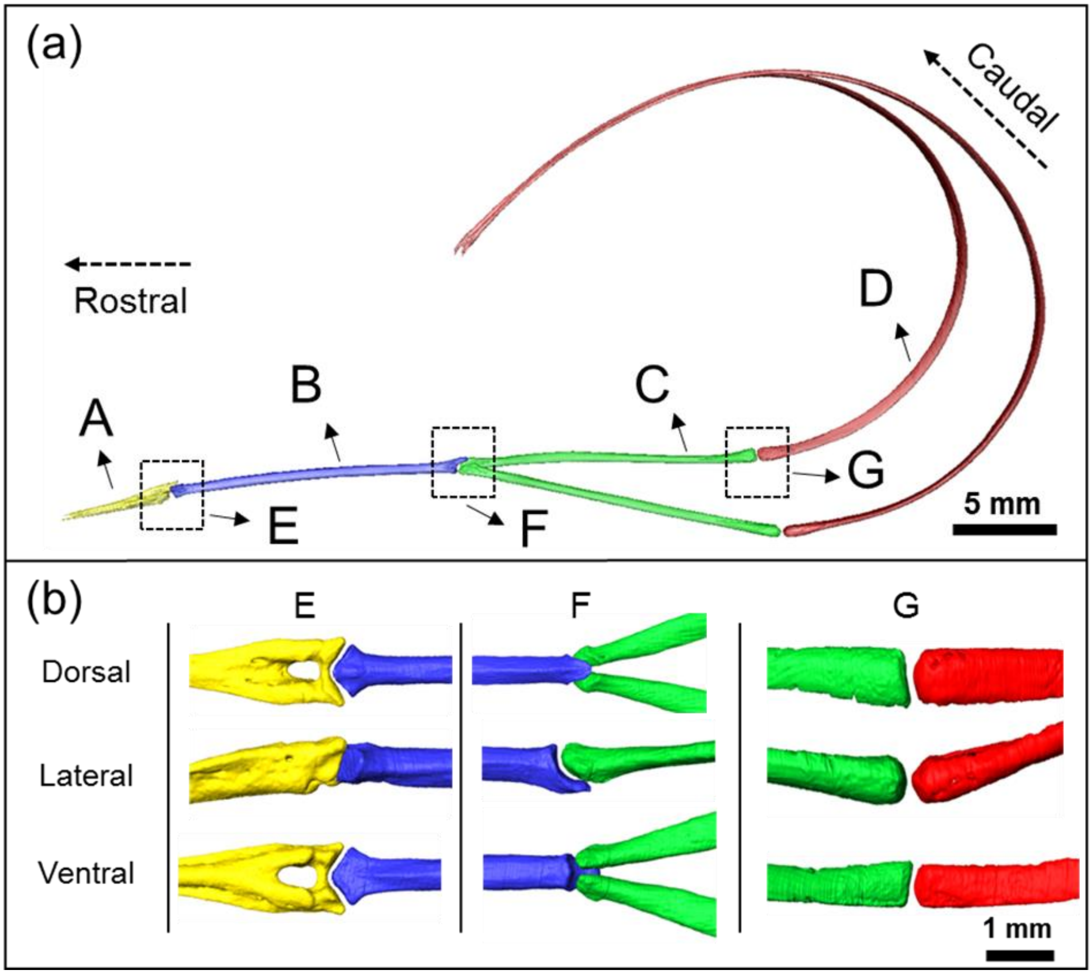

Figure 3.4. Micro-computed tomography images of the hyoid apparatus of an acorn woodpecker, colored for clarity. (a) Left lateral view segmented 3D models. A: paraglossal bone (yellow), B: basihyal bone (blue), C: ceratobranchial bone (green), D: epibranchial bone (red), E: Saddle-shaped joint, F: Y-shaped joint, and G: Circular joint. (b) Expanded view (dorsal, lateral and ventral) of the three joints showing that each has a distinct structure associated with different articulations and functions.

The four main components of the hyoid bone are shown in Figure 3.4a (A-D) reconstructed from the µ-CT images and colorized for better visualization. At the interfaces of the four components, there are three joints (E-G). The paraglossal bone (A in Figure 3.4a, yellow) is in the lingual apex, the basihyal bone (B in Figure 3.4a, blue) is in the lingual body, and the ceratobranchial bone (C in Figure 3.4a, green) is near the lingual root. The epibranchial bone (D in Figure 3.4a, red), is connected to the ceratobranchial bone. The shape of the rostral part of the paraglossal bone appears to have a saddle-like structure. It also has a small elliptical hole (0.5 x

0.8 mm) in the caudal end. The hole in the paraglossal bone has been suggested as a pathway for a gland that secretes a sticky mucous, which is used as a glue to capture insects (Figure 3.4b) [54].

In general, the structure of a joint determines the direction and distance of movement [142]. Joint E (Figure 3.4b) is located between the paraglossal and basihyal bones. Bock [54] suggested that this saddle-shaped joint maximizes rotational movement of the tip of the tongue with a wide angle, allowing the paraglossal bone to move in various directions relative to the basihyal bone. The basihyal bone is connected with a Y-shaped joint (F in Figure 3.4b) to the two ceratobranchial bones. Each branch reaches the third joint (G in Figure 3.4b), which connects to the epibranchial bone. The morphology of the Y-shaped joint (F in Figure 3.4b) suggests that it can facilitate rotation in a single plane. The third joint (G in Figure 3.4b) appears circular, indicating that it may be more movable compared to the joints E and F since it does not have axial constraints.

Comparing the joints of the hyoid apparatus to the well-studied joints in human anatomy allows for better understanding of their articulation. The saddle-shaped joint (E) can be considered as a biaxial joint, which in humans consists of articulating concave and convex surfaces [142]. Joint E has a similar shape to the human metacarpal joint, which is movable in two planes (sagittal and frontal), suggesting the motion of joint E will be protraction and retraction along the sagittal plane, allowing for circular movement. The Y-shaped joint (F) is similar to a uniaxial pivot joint between the atlas vertebra in humans where motion is limited only to rotation in a single plane [142]. The third circular joint (G) is similar to the hip joint in humans, allowing multi-axial movement [142].

Figure 3.5a shows orthoslice images superimposed upon the reconstructed 3D model from μ-CT data of the hyoid bone along the long axis. The three joints are excluded because of their complex structure and shape. The cross-sectional area was calculated for the solid bony parts.

Figure 3.5b shows a plot of the cross-sectional area as a function of position. The plot represents two types of measurements: the cross-sectional area of a single bone (solid-filled symbols) and the

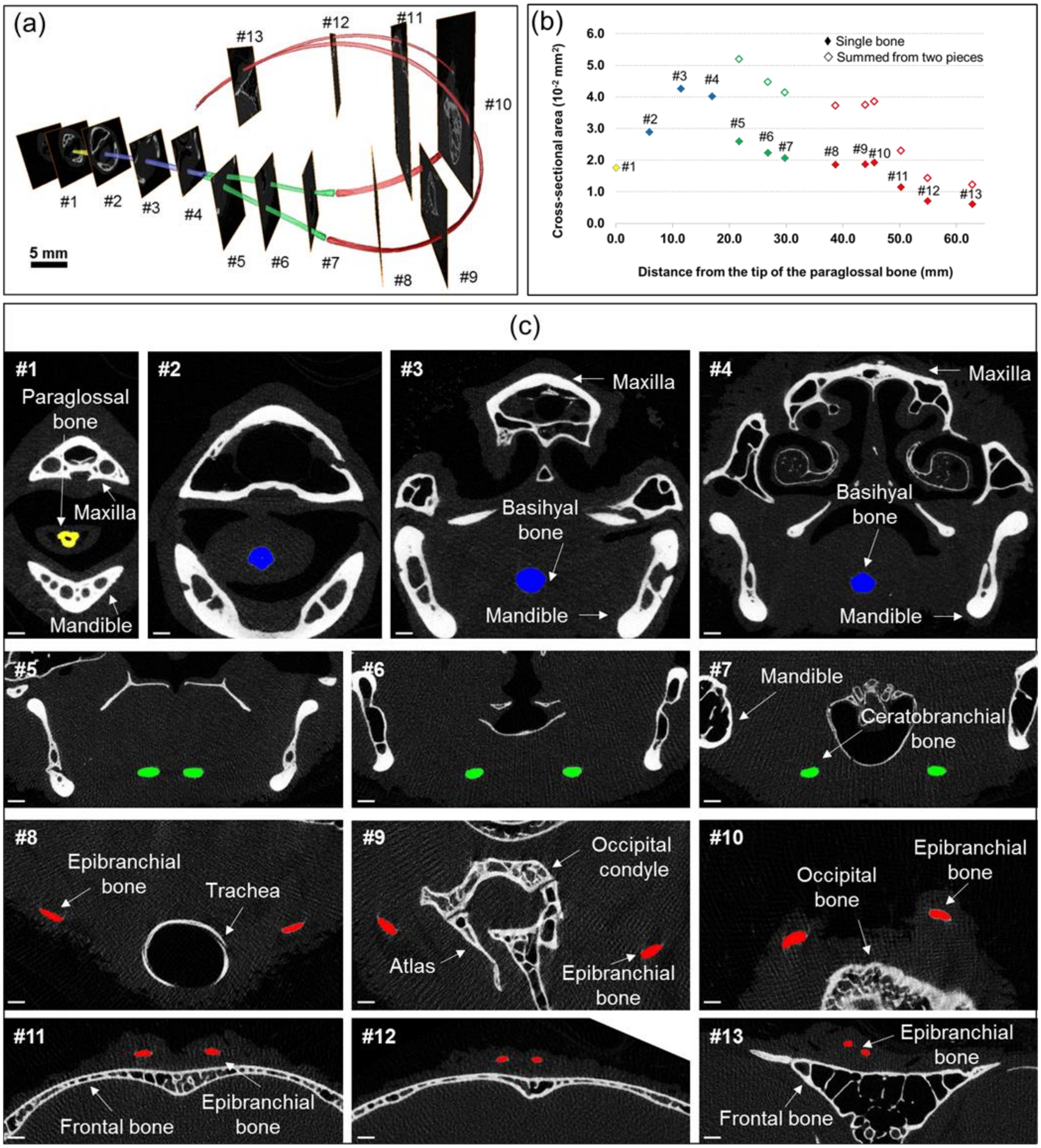

Figure 3.5. (a) Orthoslice images of the hyoid bone with reconstructed 3D models from micro-computed tomography data. (b) Plot of the measured cross-sectional area at each location. (c) Transverse cross-sectional images at each location showing the shape of hyoid bone along its length. Scale bar: 500 μm.

summed areas (empty symbols) that incorporate both segments of the ceratobranchial and epibranchial branches. The measured cross-sectional area increases from the paraglossal bone (#1) to the basihyal bone (#2-#3), then decreases through the basihyal bone (#4), ceratobranchial (#5-#7) and epibranchial (#8-13) bones. The cross-sectional shape of the paraglossal bone (#1) is an inverted isosceles triangle (in Figure 3.5a #1, yellow) but becomes more circular in the basihyal bone (#2-#4, blue), which has largest cross-sectional area as a single bone. The ceratobranchial bone is elliptical (#5-#7) and is roughly uniform in shape and cross-sectional area along its length, with an aspect ratio of 2.50. The epibranchial bone has a flattened elliptical cross-section (#8 -#13) with an elongated length up to 28 mm (Table 3.1). The rostral end of the epibranchial bone (#8) has a larger cross-sectional area (1.87×10^{-2} mm^2 and aspect ratio 3.89) compared to the one on the superior positions of the cranium (0.62×10^{-2} mm^2 and aspect ratio 1.70) (#13). These results generally corroborate those of Bock [54] (Figure 3.1e), who found the bone gradually changes from thick and less flattened at the rostral end to thin and flattened at the caudal end; however, in the present work, the aspect ratio of the extreme end in the caudal direction (#13) is smaller than the other two locations in the epibranchial bone.

Another interesting observation is that the two neighboring bones that are linked by a joint, have similar cross-sectional areas. The caudal end of the basihyal bone (#4) and the summed area of the rostral end of the ceratobranchial bones (#5) as well as the region between the caudal end of the ceratobranchial bone (#7) and the rostral end of the epibranchial bone (#8) have similar cross-sectional areas. These results suggest that the bone mass or cross-sectional area is maintained through the joint. This is a new observation that suggests that stress discontinuities are prevented across the various joints.

Figure 3.6 shows SEM micrographs of the dorsal surface and cross-section of the lingual apex with the corresponding EDS and FTIR spectra. Figure 3.6a is a photograph of the lingual apex indicating the viewed locations in Figure 3.6b, c, e, and f. The lingual apex has barbed tips (Figure 3.6b) and at higher magnification (Figure 3.6c) a scale-like structure is observed with scale diameters between 30-40 μm (white dotted lines). The EDS spectrum (Figure 3.6d) indicates the presence of sulfur, phosphorus, and oxygen. Carbon and nitrogen peaks are not labeled and excluded for quantification results due to the relatively high intensity of the carbon peak and low intensity of the nitrogen peak compared to the other elements (S, P, O, and Ca). The chemical composition (mainly P and S) is similar to that reported for the keratin in the woodpecker's beak [110]. This, coupled with the SEM images indicates that the lingual apex has a keratin outer sheath that surrounds the paraglossal bone, as is found in other birds [141]. The cross-section of the lingual apex (Figure 3.6e and f) shows that the lingual apex has two distinct layers: a keratin sheath (K) at the surface and a central bone (PG, paraglossal bone) that has some surrounding void

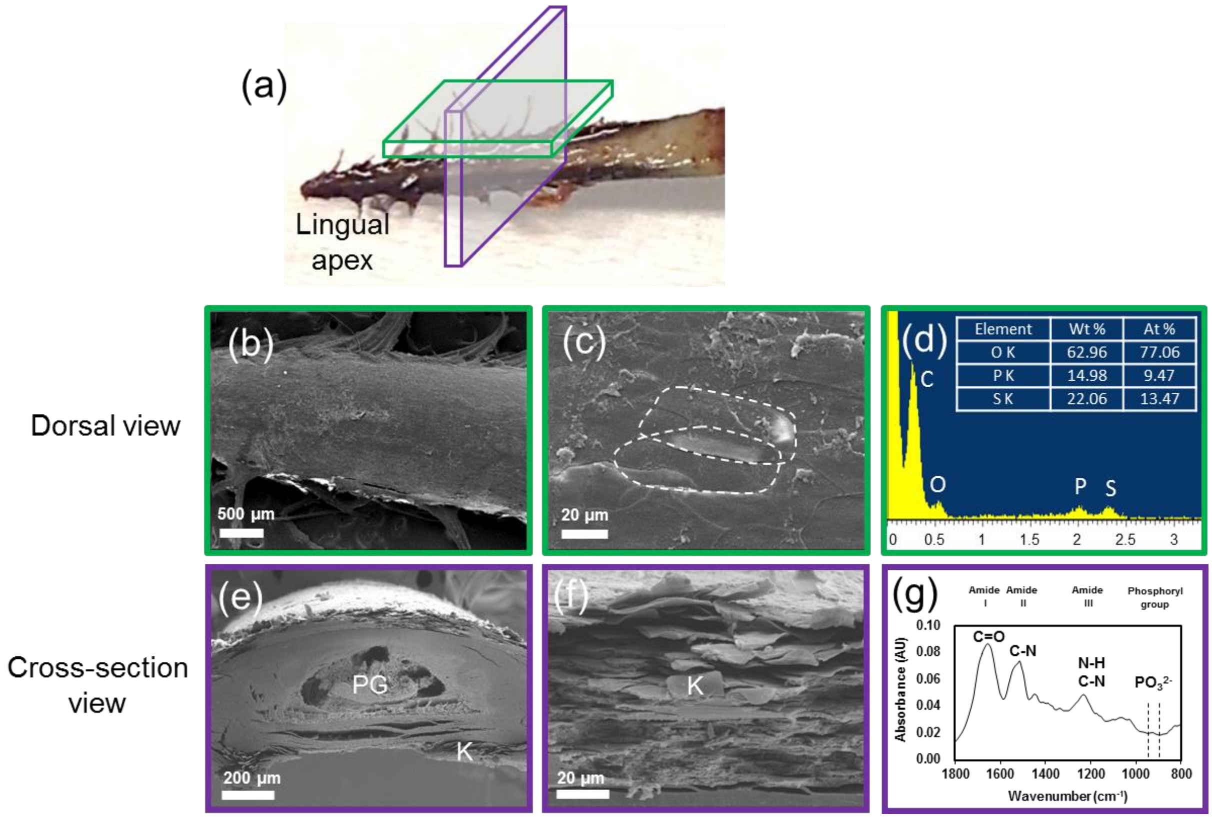

Figure 3.6. (a) Photograph of dissected hyoid apparatus highlighting the imaged locations on the lingual apex. Scanning electron micrographs on the dorsal surface, (b) low magnification and (c) high magnification with the outline of two keratin scales (white dotted lines), and (d) energy dispersive X-ray spectroscopy results. Scanning electron micrographs on the cross-section, (e) low magnification and (f) high magnification. (g) Fourier transform infrared spectrum of the polished sample near the region shown in (f). PG: paraglossal bone, K: keratin scales.

areas, likely generated by the dehydration process. The keratin sheath shows a layered structure composed of scales (Figure 3.6f). The presence of S is due to S-containing cysteine groups found in keratin. The presence of P in the keratin might be related to a strengthening effect, known as phosphorylation, of the keratin filaments at the cellular level [143]. As shown in Figure 3.6g, FTIR spectrum of the cross-section of the lingual apex exhibits a peak near 950 cm^{-1}, a known band for phosphorylated proteins [144]. Also present are the typical peaks of keratin near 1600-1700 cm^{-1} (amide I), 1550 cm^{-1} (amide II), and 1200-1300 cm^{-1} (amide III) [144].

Figure 3.7a provides an overview of observed regions in Figure 3.7b-j. In Figure 3.7b and c, a similar scale-like structure is observed on the lingual body. The EDS spectrum of the cross-section of the lingual body (Figure 3.7d) is similar to the lingual apex (Figure 3.6d), indicating that it is keratin. As shown in Figure 3.7e, the longitudinal-section image of the lingual body illustrates a similar structure to the cross-sectional structure of the lingual apex. Some bundles of fibers are observed near the center part of the basihyal bone (Figure 3.7f and g). The fibers are ~ 194 nm in diameter and > 10 μm in length, comparable to mineralized collagen fibril bundles found in the bony core of woodpecker's beak [110]. Overall, the multilayered structure of the lingual body is similar to the lingual apex. In the dorsal view, the shape and dimension of the keratin scales in both the lingual apex and body have isotropic shapes, which are comparable to the keratin scales on beaks of other birds [111, 112, 145], in contrast to the elongated scales found on woodpecker beaks [110]. Figure 3.7h shows a SEM image and Figure 3.7i (from BH, basihyal bone) and Figure 3.7j (from M, muscle tissues) show EDS spectra of the cross-sections of the lingual body. In Figure 3.7h, the outer region is covered with the dermis (D) and epidermis (ED). The ratio of calcium to phosphorus (Ca/P) is 1.56, which is lower than stoichiometric hydroxyapatite (1.67) [146]. In the central region, there are four muscle tissues, a connective tissue (CT) [141], and a bone core (BH, approximately 500 μm in diameter). The EDS spectrum of the basihyal bone (Figure 3.7i), obtained from the central region of the bone confirms the presence of calcium, phosphorus, and oxygen. The average Ca/P of all hyoid bones was 1.50 ± 0.10. In comparison, the average ratio of adult chicken cortical bone (1.73 [147]) and bovine femur (2.23-2.31 [146]) are larger than in the hyoid bones. However, the Ca/P is within the range reported for other animal bones [148]. The strength of synthetic hydroxyapatite increases with increasing Ca/P ratios up to ~ 1.67, then decreases [149], which implies that the hyoid bones may not be as strong or stiff as other skeletal bones. Because of the homogeneous distribution of the main mineral elements (Ca and P), the effect of chemical composition on the mechanical properties is suggested to be minor compared to the effect of the microstructure, such as pore size and porosity. The EDS spectrum of muscle tissues presents only phosphorus (muscles have a large amount of adenosine triphosphates), without any sulfur or oxygen, as shown in Figure 3.7j. The absence of the oxygen peak might be due to dehydration during the sample preparation. In summary, cross-sectional and longitudinal-sections of SEM micrographs and EDS analysis show a multilayer structure with a keratin sheath on the surface of the lingual apex and body and a central bony core in the lingual body that is surrounded by soft tissue. Due to the similarity of the microstructure and chemical composition between the lingual body, the lingual root and the hyoid horn, the latter two are not presented here. TGA analysis found organic to mineral ratios of 0.84:1 for the lingual apex and 1.63:1 for the lingual body, indicating a higher density structure is found within the lingual apex (where the tongue makes contact with trees and prey) as compared to the lingual body.

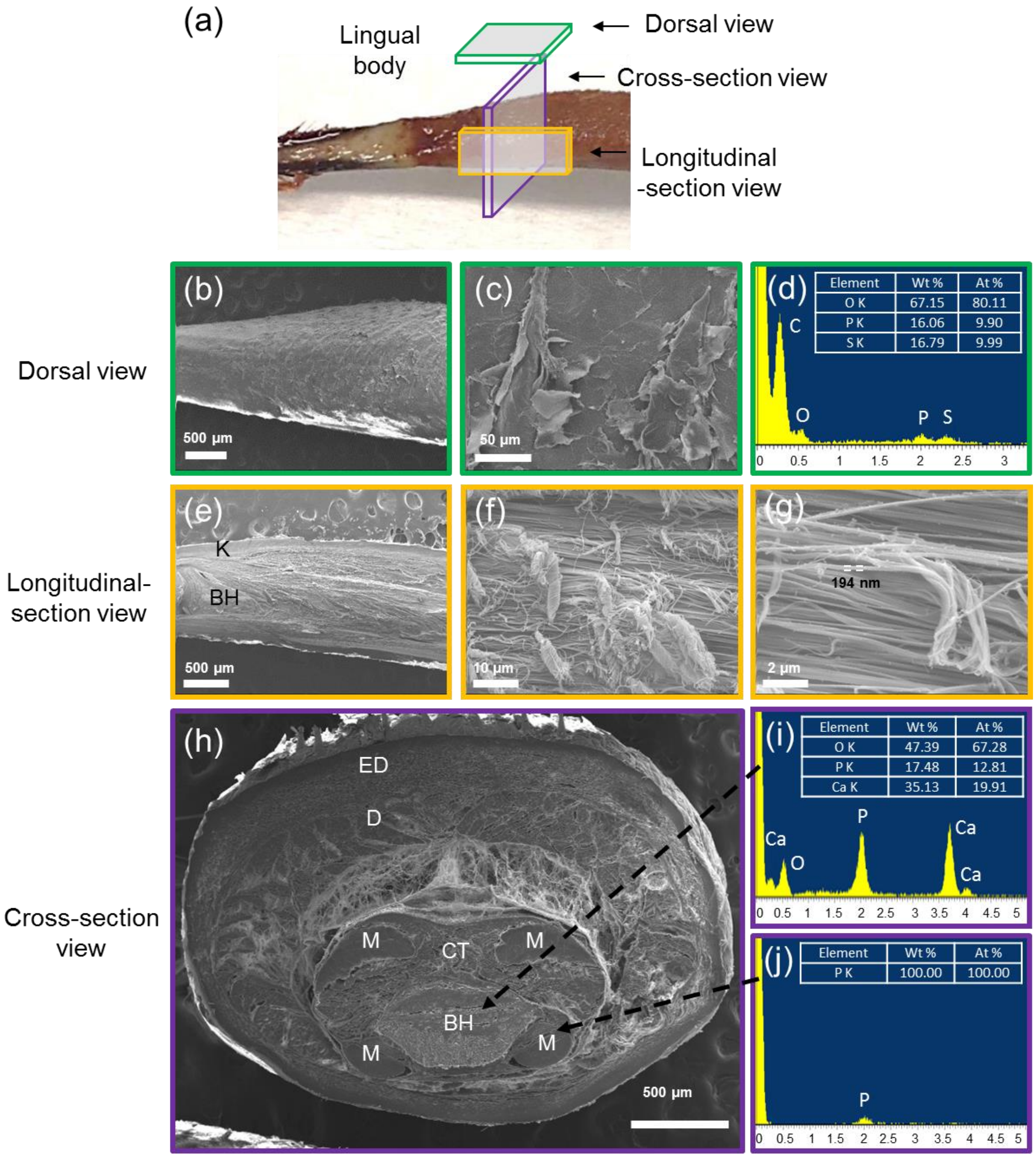

Figure 3.7. (a) Photograph of dissected hyoid apparatus highlighting the imaged locations on the lingual body. (b-c) Scanning electron micrographs and (d) energy dispersive X-ray spectroscopy results of the dorsal surface. Scanning electron micrographs (e-g) on the longitudinal-section and (h) on the cross-section displaying four different muscles (M) surrounding the basihyal bone (BH). (i-j) Energy dispersive X-ray spectroscopy results of the center of BH and the muscles, respectively. CT: connective tissue, D: dermis.

3.3.3 **Nanoindentation**

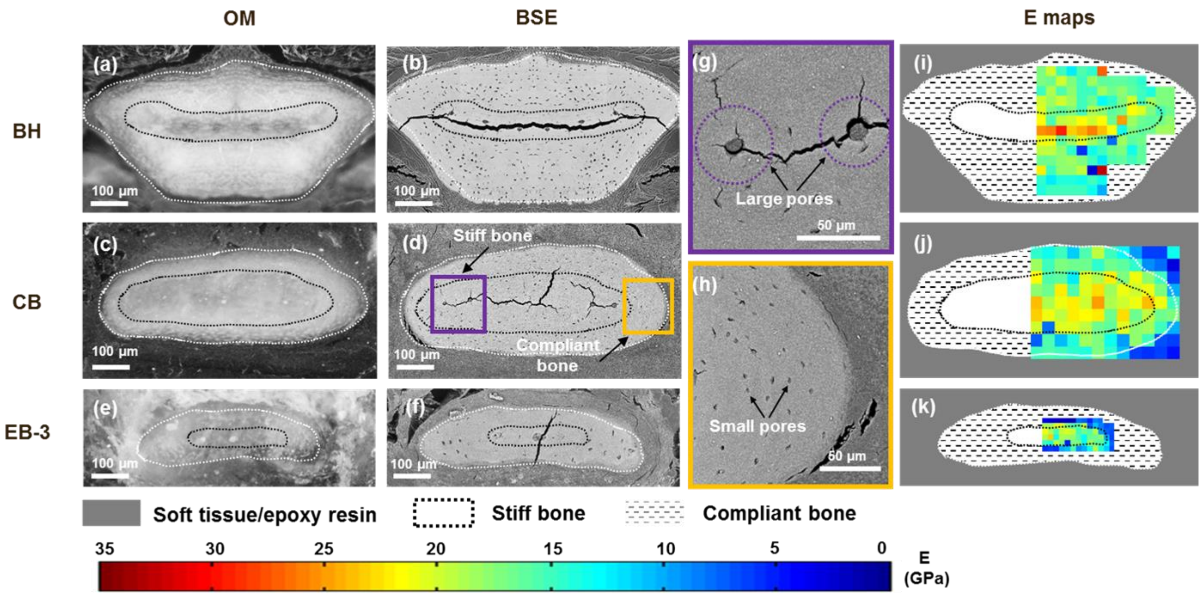

Figure 3.8. Cross-sectional images of the basihyal (BH), ceratobranchial (CB), epibranchial (EB) bones: (a, c, e) Optical micrographs (OM) of each bone, (b, d, f) back-scattered electron (BSE) micrographs with (g,h) the magnified images of the CB bone, and (i, j, k), nanoindentation (modulus) maps overlaid on schematic illustrations of bone regions. The indentation sites for each hyoid bone are shown in Figure 3.5a (BH: #4, CB: #6, and EB: #12). A color scale shows the gradient in *E* from the highest value (35 GPa) in red to the lowest value in blue (0 GPa). In the schematic illustrations (i, j, k), grey denotes the area of soft tissue/epoxy resin, white regions are the more stiff bone and the dash-filled regions are the more compliant bone. The optical micrographs were acquired prior to nanoindentation tests while the BSE micrographs (b, d, f) were obtained after the indentation tests. Note that BSE micrographs are not sensitive enough to image small nanoindentation topography features (~ 400 nm). The cracks appeared under the high vacuum condition in the scanning electron microscope and were not present during nanoindentation.

The mechanical properties of different regions of bones were determined using nanoindentation mapping (Figure 3.8, Figure 3.9, and Table 3.1). Optical micrographs of cross-sections of the basihyal, ceratobranchial and epibranchial bones (Figure 3.8a, c and e) highlight two different bony regions. In Figure 3.8, the paraglossal bone has a triangle shape and large void area in the center, which interfere the continuous nanoindentation mapping. We had to select and discretize different areas to carry out the mapping and the *E* maps did not provide enough data compared to the other samples shown in Figure 3.8. Therefore, we made a decision to exclude the paraglossal bone and focus on the most representative results. The outer region between the white-dotted and black-dotted lines has a brighter contrast than the inner region enclosed in the black-dotted line. BSE micrographs (Figure 3.8b, d and f) taken after nanoindentation and subsequent dehydration show different microstructures in two regions in the magnified micrographs (Figure 3.8g and h). The outer regions have a higher density of elliptically shaped pores (3~9%) than the inner region,

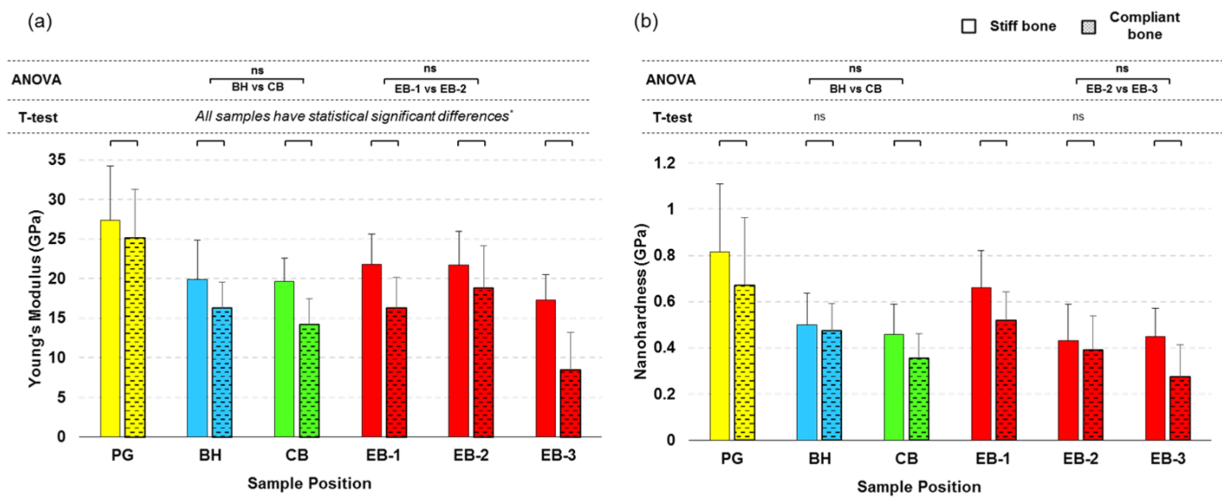

Figure 3.9. Bar charts of (a) the Young's modulus and (b) hardness of each bone. The solid-filled bars represent the average value of the stiff bone region and the dash-filled bars represent the average value of the compliant bone region. PG: paraglossal bone (yellow). BH: basihyal bone (blue). CB: ceratobranchial bone (green). EB-1 to EB-3: epibranchial bone (red). The indentation sites for each hyoid bone are shown in Figure 3.5a (PG: #1, BH: #4, CB: #6, EB-1: #8, EB-2: #10, and EB-3: #12). For both the one-way ANOVA and t-tests, comparisons where no statistically significant difference was found are marked with an "ns" symbol.

each with a major axis ~7.50 μm and a minor axis ~2.30 μm. The cracks in the BSE micrographs were generated during dehydration in the vacuum chamber and are mainly distributed within the inner/stiff bone.

Based on the contrast difference, schematic illustrations are shown with three simplified features (Figure 3.8i, j and k): soft tissue/epoxy resin (gray), the light region between the black-dotted outline and the white-dotted outline (black dashed) and the dark region inside of the black-dotted outline (white). Nanoindentation mapping results distinguish two bone regions (termed "stiff" and "compliant"), which are overlaid on the illustrations. The cross-sectional areas for indentation (basihyal, #4; ceratobranchial, #6; epibranchial, #12) are indicated in Figure 3.5a. The small pores (Figure 3.8h) have similar dimensions as osteocyte lacuna found in skeletal bird bones (~ 10 μm) [150, 151]. The inner regions are populated with larger, circular pores with diameters of 8-20 μm (Figure 3.8g). The larger pores have similar dimensions to vascular channels found in skeletal bird bones (~ 25 μm) [150, 151] but it is unclear if vascularization is present. When considering energy absorbance, this porous and compliant bone can be considered to be a cellular structural design element, which are found throughout nature and are known to be effective at increasing energy absorbance [5].

The average E and H values, the standard deviation, and the number of indentation tests for each specimen are listed in Table 3.1. The average E (and H) of each hyoid bone ranged from ~17 to 27 GPa (0.4 to 0.8 GPa) for the inner bone and from ~9 to 25 GPa (0.3 to 0.7 GPa) for the outer bone (Figure 3.9a and b), indicating the bones consist of an outer, more compliant region and an inner, more stiff region. According to statistical analyses using a t-test between the stiff and compliant bones, the E values of the inner region are significantly higher ($p < 0.05$, Figure 3.9a) than the outer region in all of the bones. The stiffer bone always has a higher average E when compared to the compliant bone, ranging from a slight increase in the paraglossal bone to a twofold increase in the epibranchial bone. Unlike E, a few of the comparisons between the stiff and compliant bone for H were found to exhibit no statistically significant differences. However, these cases (BH and EB-2) can be explained by the fact that H is dependent upon not only elastic deformation (as is the case for E), but also plastic deformation, which is generally considered to be more variable. These bone structures are unlike most other bone, where a dense outer sheath surrounds a less dense core, such as with mammalian skeletal bones. It is unclear what, if any, mechanical advantage this arrangement has in the hyoid bones. However, it can be speculated that a more compliant shell could protect the stiffer, more brittle core.

From Figure 3.8b, d and f, the average pore size (major axis, *a*, and minor axis, *b*) in the compliant bone is larger in the epibranchial ($a \approx 7.50$ μm and $b \approx 2.30$ μm) compared to the basihyal ($a \approx 6.30$ μm and $b \approx 2.90$ μm) or ceratobranchial ($a \approx 5.50$ μm and $b \approx 2.00$ μm) bones, which reduces the average *E*. Among the hyoid bones, the paraglossal bone had the highest *E* and *H* values, up to three times greater than the epibranchial bone for both the stiff and compliant regions, which corroborates the μ-CT results in Figure 3.3 that show a higher mineral density at the rostral position. The *E* values of the basihyal and ceratobranchial bones as well as the rostral end (EB-1) and midsection (EB-2) of the epibranchial bones are not significantly different (labeled as 'ns' in Figure 3.9a) for both stiff and compliant regions. In the epibranchial bone, EB-3 has a significantly lower *E* value than EB-1 and EB-2, as well as the other bones.

Previously reported values of Young's modulus obtained from tensile tests of the hyoid apparatus near the first joint were 1.3 GPa [117], which show a large deviation from the present result on the basihyal bone. The main reason for this discrepancy is that, in the previous work, tests were conducted on specimens that included the joints (with soft tissues), which would significantly reduce the measured modulus. Other test locations on the two positions of the epibranchial bone ($E \sim 1.7$ to 3.7 GPa) [117], showed a similar discrepancy in *E* to the present study. This discrepancy might be due to the difference in testing methods (tensile test, indentation test), the proportion of hard and soft tissues as well as different levels of hydration in specimens. It is well known that nanoindentation results on dehydrated samples may result in an increase of up to 20% of Young's modulus and hardness when compared to hydrated samples [152]. To perform nanoindentation, however, the samples must be polished to a mirror finish, therefore they must be dehydrated first. Nanoindentation on dehydrated samples is a common technique to investigate the mechanical properties of bone [153, 154] and biological materials [50].

For comparison (Table 3.1), *E* and *H* values for bovine femur cortical bone measured by nanoindentation methods are 24.4 GPa and 0.68 GPa, respectively [152]. The *E* and *H* of bird wing bones are 27.8 GPa (bending and tension) [155] and 0.55 GPa (Vickers hardness) [151], respectively. The *E* and *H* of beak bones from a woodpecker are 30.2 GPa and 1.16 GPa (nanoindentation), respectively [110]. In comparison with the above, the *E* and *H* of the hyoid bones are close to the values of the bird skeletal bones. The *E* and *H* values depend on structural features, such as porosity and proportion of organic materials [118, 156]. Since there are no reported mechanical properties for the other bird hyoid bones, further comparative analysis cannot be made.

3.4 Structure-Mechanical Properties Relationship

Structural shape is an important factor in the bending resistance, *EI*, where *I* is the second moment of area [110, 157]. Along the length of the hyoid bones, the term (*I*) changes along with the observed shapes: triangular, to circular, and finally to elliptical:

$$I_{\text{triangle}} = \frac{1}{36} a_t b_t^3 \tag{3.5}$$

$$I_{\text{circle}} = \frac{\pi}{4} a_c^4 \tag{3.6}$$

$$I_{\text{ellipse}} = \frac{\pi}{4} a_e b_e^3 \tag{3.7}$$

where a_t = base and b_t = height for the triangle, a_c = radius for the circle and a_e = major axis and b_e = minor axis for the ellipse. From Eqns. (3.5)-(3.7), *I* varies along the length, from the triangular paraglossal (3.19 x 10^{-3} mm^4) through the circular basihyal (14.7 x 10^{-3} mm^4) to the elliptical ceratobranchial (0.75 x 10^{-3} mm^4) and epibranchial (0.01 – 0.50 x 10^{-3} mm^4) bones (Table 3.1).

Because the bones consist of two regions with different Young's moduli, a volume fraction rule-of-mixtures was used to calculate the bending resistance of each bone (stiff and compliant regions) [158]. For simplicity, it was assumed that the diameter of each bone was the same along its length, so the area fraction (*A*) was used instead of the volume fraction. The area fractions of the stiff (A_{stiff}) and compliant ($A_{\text{compliant}}$) bone regions were measured from the cross-sectional images of optical micrographs (Table 3.1). A_{stiff} is ~0.2 in the paraglossal and basihyal bones, ~0.5 in the ceratobranchial bone and 0.2-0.3 in the epibranchial bones. The composite Young's modulus (E_c) is given as:

$$E_c = E_{\text{stiff}} A_{\text{stiff}} + E_{\text{compliant}} A_{\text{compliant}} \tag{3.8}$$

As shown in Table 3.1, the bending resistance of the composite bone (E_cI) increases from the paraglossal bone to a maximum in the basihyal bone (25.12×10^{-8} N m^2). It then greatly decreases through the ceratobranchial to a minimum at the caudal end of the epibranchial bones (0.01×10^{-8} N m^2). The hyoid bones can be modeled as a flat spiral spring, where the angular deflection is proportional to $(E_cI)^{-1}$. This indicates that the epibranchial bones can undergo substantial deflection compared to the paraglossal and basihyal bones; the latter need sufficient stiffness for excavating insects from trees. Since the flat spiral spring is used to store elastic energy [159], this shape is possibly related to previous statements of Oda *et al*. [132] and Zhou *et al*. [117] that the hyoid bones play a role as a shock-absorber or a damper during pecking.

Table 3.1. Dimension, shape, and mechanical properties of each of the hyoid bones. See Figure 3.5a for bone locations.

Bone	Cross-sectional shape (scheme)	Cross-section (μCT, L: left, R: right)	Dimensions (mm) and second moment of area (I) (x 10^{-3} mm^4)	Bone type	Number of nanoindentation tests (n)	Young's modulus E (GPa)	Nanohardness H (GPa)	Area fraction	Bending resistance E_cI (x 10^{-8} N·m^2)
Paraglossal (#1)	Triangular 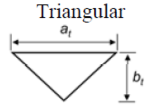 $I_{triangle} = \frac{1}{36} a_t b_t^3$		Length: 5.6 a_t = 1.04 b_t = 0.48 I: 3.19	Stiff	78	27.4 ± 6.8	0.81 ± 0.29	0.17	8.14
				Compliant	170	25.1± 6.1	0.67 ± 0.29	0.83	
Basihyal (#4)	Circular 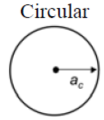 $I_{circle} = \frac{\pi}{4} a_c^4$	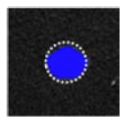	Length: 14 a_c = 0.37 I: 14.7	Stiff	35	19.9 ± 5.0	0.49 ± 0.14	0.22	25.12
				Compliant	132	16.3 ± 3.3	0.47 ± 0.12	0.78	
Ceratobranchial (#6)	Elliptical 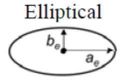 $I_{ellipse} = \frac{\pi}{4} a_e b_e^3$	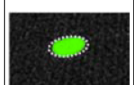	Length: 14 a_e = 0.35 b_e = 0.14 I: 0.75	Stiff	49	19.6 ± 3.0	0.46 ± 0.13	0.49	1.27
				Compliant	50	14.2 ± 3.3	0.36 ± 0.10	0.51	
Epibranchial 1 (#8)	Elliptical 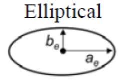 $I_{\text{ellipse}} = \frac{\pi}{4} a_e b_e^3$		Total length: 28 a_e = 0.37 b_e = 0.12 I: 0.50	Stiff	105	21.8 ± 3.8	0.66 ± 0.16	0.32	0.91
				Compliant	122	16.3 ± 3.9	0.51 ± 0.12	0.68	
Epibranchial 2 (#10)			a_e = 0.45 b_e = 0.06 I: 0.08	Stiff	112	21.7 ± 4.3	0.43 ± 0.16	0.30	0.15
				Compliant	83	18.8± 5.4	0.39 ± 0.15	0.70	
Epibranchial 3 (#12)		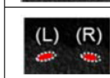	a_e = 0.22 b_e = 0.04 I: 0.01	Stiff	68	17.3 ± 3.2	0.45 ± 0.27	0.20	0.01
				Compliant	60	8.5 ± 4.7	0.27 ± 0.14	0.80	
Bovine femur cortical [33]	-	-	-	Cortical bone	30	24.4 ± 2.2	0.68 ± 0.10	-	-
Bird wing (humerus and ulna)	-	-	-	Cortical bone	-	27.8 [37]	0.55 ± 0.15 (microhardness [38])	-	-
Woodpecker (beak bones) [11]	-	-	-	Trabecular-like inner bone layer	-	30.2 ± 3.6	1.16 ± 0.19	-	-
Great spotted woodpecker [6, 50]	-	-	-	Cranial bone	-	0.3 ± 0.02 [6, 50]	-	-	-

3.5 **Conclusions**

Macro- and micro-structural analysis of acorn woodpecker's (*Melanerpes formicivorus*) hyoid apparatus and hyoid bones were investigated by a multiscale structural analysis and mechanical property evaluation. The main findings are:

- The first hyoid bone/joint 3D model was successfully developed using micro-computed tomography image analysis and used for quantitative analysis of cross-sectional area and shape change of the hyoid bones along their lengths.
- Scanning electron microscopy and energy dispersive X-ray spectroscopy on the lingual apex and body reveal a multilayered structure with a keratin sheath on the lingual apex and body and a central bony core in the lingual body.
- Electron energy dispersive X-ray analysis showed that Ca/P ratio of all hyoid bones averaged 1.5, a slightly lower ratio than for skeletal bird bones (1.7) [147].
- Nanoindentation results show that all hyoid bone cross-sections consist of a dense/stiff interior region surrounded by a porous/compliant region. This compliant region may be effective at dissipating energy in the hyoid bones during pecking.
- For the Young's modulus, the paraglossal bone has the highest value, comparable to the inner bony part of the beak. The basihyal and ceratobranchial bones have similar values, but are lower compared to the paraglossal bone. The epibranchial bone exhibited properties that varied from the highest at the rostral to the lowest at the caudal.

Chapter 3, in full, is a reprint of the material as it appears in Acta Biomaterilia. Jae-Young Jung, Steven Naleway, Nicholas Yaraghi, Steven Hererra, Vincent Sherman, Eric Bushong, Mark Ellisman, David Kisailus, and Joanna McKittrick, 2016. The dissertation author was the primary investigator and author of this paper.

CHAPTER 4: A COMPARATIVE ANALYSIS OF THE AVIAN SKULL: WOODPECKERS AND CHICKENS

4.1 Introduction

Woodpeckers use their beaks as a hammering tool without sustaining any reported traumatic brain injury or concussion during pecking [30, 129]. The hammering rates are up to 20 Hz with impact speeds ranging from 1 to 7 m/s, and deceleration up to 1,200 ***g*** [30]. There have been several attempts to reveal the key elements of the successful utilization of their beaks and heads as excavating tools. It has been pointed out that woodpeckers have strong neck muscles [129], zygodactyl feet (two toes pointing forwards and two pointing backwards) [30, 160], a large portion of spongy bone on the skull with relatively little cerebrospinal fluid [129], and the hyoid apparatus and its internal bone (hyoid bone) [54, 116, 117, 119, 132, 133], identified as a highly-elongated and unusual structure only found in woodpeckers and hummingbirds. In contrast, chickens do not hammer against trees to sustain their diet; they use their upper and lower beaks to pick up food from the ground [110], and possess a short hyoid apparatus [125]. A study conducted by Mehdizadeh *et al.* [161] evaluated the biomechanics of the head and beak motion of broiler chickens (*Gallus gallus domesticus*) during feeding; an image analysis was used to identify head's movement and concluded that chickens do not peck against the ground or other heavy objects in the way that woodpeckers do. Given these diverging pecking habits, a comparative study of the heads of woodpeckers and chickens can be an insightful approach towards identifying the anatomical features that provide woodpecker's remarkable resistance to dynamic impacts.

To better explain the concept of energy dissipation in the woodpecker's head during hammering, the head's anatomy and mechanical properties need to be understood in detail. Lee *et al.* [110] reported a reduced elastic modulus of 8.7 GPa for the lower rhamphotheca (a keratinized outer sheath mainly composed of β-keratin [45]) of a red-bellied woodpecker (*Melanerpes carolinus*) obtained from nanoindentation tests. Wang *et al.* [119] reported, using a 3D finite element analysis, that woodpeckers have a longer lower beak bone (1.2 mm difference) than the upper one, so that the first impact occurs at the lower beak bone. Zhu *et al.* [162] reported that the Young's moduli in the skull showed a lower value (4 ~ 9 GPa) than those of beak bones (~ 30 GPa [110]). The aforementioned datasets of the woodpecker skull bones are valuable resources to investigate and mimic the impact-resistant structures/materials found in nature and can be used as a template for a biomimic approach to develop new materials. However, the previous data were collected from only two species (i.e., a red-bellied woodpecker and a great-spotted woodpecker), and showed a broad range of the Young's moduli from 0.31 GPa [114, 119, 130] to 6.6 GPa [123]. Another dataset from a different species (an acorn woodpecker in this manuscript) can be a valuable addition to the field of biomechanics. Other factors, such as chemical composition, degree of mineralization or calcification and porosity, have not been discussed in detail. Such variations in terms of mechanical properties highlight the necessity to expand our knowledge of the woodpecker's head anatomical features at different length scales. The head of a chicken provides a good reference to study the woodpecker head, the anatomy of the head of chickens has been well studied; there are many sources of scientific papers about its anatomy [163, 164] and open-source electronic 2D/3D imaging data [165]. In addition, the biomechanics of the pecking behavior of the chicken has been well studied [161, 166, 167] compared to other birds. In order to find food, both species peck, but against the different substrates (i.e., trees vs. dirt on ground), implying their structural designs and materials can be altered. This biomechanical data is useful to our biomechanics approach as it provides a direct comparison with respect to the shape of the bills, the structural components of the head, and pecking motion. Finally, the microstructural features and chemical composition of the chicken skeleton can be found in the literature. Structural properties of the head (beak bone, skull bone) have been reported by Lee *et al.* [110], who determined that the chicken beak bone had a porosity of ~42%, while the beak bone of woodpeckers had a porosity of ~10%, which is comparable to other structural biological materials, such as non-mineralized materials (i.e., a 3 % of porosity in horse hoof and a 6% in rhino horn) and mineralized materials (i.e., a 5% of porosity in compact bovine femur bone and a 12% in human dentin) [4]. Thus, chickens provide a reasonable control based on extensive microstructural data, biomechanical analyses of their pecking habits, and material characterization data of the head.

We hypothesize that the differences in pecking behavior can be seen in the anatomy and mechanics of these two species. To confirm the proposed hypothesis, this study aims to identify the anatomical structure, as well as the mechanical/chemical properties of woodpecker skull bones. As a control group of non-pecking avian species, a domestic chicken was chosen and compared to highlight anatomical differences with woodpeckers. Characterization of mechanical and chemical properties of the skull bone for both species intends to further define the structure-properties relationships in avian bones and the effects that pecking behavior has on these relationships.

4.2 Materials and Methods

4.2.1 Sample collection and preparation

This study was conducted under the approval of an animal care and use program by the Institutional Animal Care and Use Committee (IACUC) at the University of California, San Diego (Tissue Permit Number: T14068).

An adult acorn woodpecker (*Melanerpes formicivorus*) was donated after death from a Northern California ranch. The bird was immediately frozen in a freezer at -20˚C, and kept as such during transport to the lab. The woodpecker specimen, stored at -20˚C, was gradually thawed at room temperature for 30 min prior to testing. All tests were performed under ambient conditions (25˚C, 60% relative humidity). Additionally, a dried chicken skull (*Gallus gallus*), prepared for taxidermy purposes (using *Dermestidae*, known as flesh eating beetles) without whitening and de-greasing [168], was purchased from an online vendor (Atlantic Coral Enterprise, Inc.). There were no chemical and heat treatments on the sample prior to our study.

4.2.2 **Micro-computed tomography (μ-CT)**

The acorn woodpecker was scanned by μ-CT (SkyScan 1076, Bruker microCT, Kontich, Belgium) with a rotation step of 0.7º, a 100 kV acceleration voltage, and an isotropic voxel size of 9.06 µm. Raw data of a domestic chicken were obtained from digimorph.org [165], operated by the High-Resolution X-ray CT Facility at the University of Texas, Austin. The chicken skull was scanned at 200 kV with an isotropic voxel size of 77.6 µm. Each skull bone was visualized and analyzed using Amira software (FEI Visualization Sciences Group, Burlington, MA) for visualization and a 3D rendering with mineral density color scaling.

μ-CT scans of the chicken and woodpecker were analyzed to compare the average thicknesses of cortical (T_c) and trabecular (T_b) bones. ImageJ software (National Institutes of Health, Bethesda, MD) and its open source plugin, BoneJ [169], were used for 2D bone morphometric analysis.

CTan software (Bruker MicroCT, Kontich, Belgium) was used for 2D and 3D bone morphometric analysis to select the range of the start and end slices based on the 3D image to include only the skull bone part. A series of binarized images with a certain range of threshold values was reconstructed and saved prior to the bone morphometric analysis [170]. The segmented images corresponding to the skull region were isolated to estimate the total volume of the skull bone (V_s) and brain (V_b), the whole head volume ($V_w = V_s + V_b$), the ratio of the skull bone volume to the whole head volume (V_s/V_w), and the ratio of the average cortical thickness to the whole head volume (T_c/V_w). For a simplified comparative analysis, the effects of other soft tissues, such as muscles, cerebrospinal fluids, and eyes, were not considered in this analysis.

To calculate porosity in a specific volume of interest (VOI), the standardized terminology was adapted from the American Society for Bone and Mineral Research (ASBMR) for bone histomorphometry [171]. Specifically, the tissue volume (TV) is defined as the volume of selected VOI, and is the sum of the bone tissue (bone volume) and void volume area (pores) [171]. The bone volume (BV) is defined as the volume of binarized objects within the VOI, where is a bright contrast region of the bone tissue [171]. The ratio of the bone volume to tissue volume (BV/TV) is derived from above two definitions. Then, the closed, open, and total porosities were calculated in the same VOI. Here, a closed pore in 3D is defined as a connected assemblage of space (black) voxels that is fully surrounded on all sides in 3D by solid (white) voxels in a segmented binary image, while an open pore is defined as any space located within a solid object or between solid objects, which has any connection in 3D to the space outside the object [69, 170-172]. A benefit of binarized 3D image morphometric analysis is that the software successfully recognized the closed and open cells, unlike the 2D image analysis, which cannot distinguish between closed and open cells because of limited geometrical information.

4.2.3 **Microstructure and chemical composition**

The chicken and woodpecker skulls were analyzed by scanning electron microscopy (SEM) and X-ray energy dispersive spectroscopy (EDS) to characterize the microstructural features and chemical composition. Although the EDS analysis has some limitations based on its low spatial/volumetric accuracy compared to other surface characterization techniques (e.g., X-ray photoelectron spectroscopy or inductively coupled plasma with mass spectroscopy and/or atomic emission spectroscopy), it provides site-specific elemental composition at the micron scale, which cannot be obtained by the latter techniques. A typical X-ray interaction volume provided by EDS is on the order of a few cubic microns while the length scale of microstructures investigated in this manuscript ranged over at least 50~100 μm, and the accuracy of 1 μm as the spatial resolution is small enough. Regarding the energy resolution, another set of EDS data for the chicken and woodpecker skull bones were previously reported (i.e., Lee et al. [110] by using the same technique.

To obtain accurate characterization data and remove artifacts generated by surface topology, an identical sample preparation procedure was used as in our previous study [173]; Here, embedded samples in epoxy were cut into smaller pieces along the transverse cross-section (which exposes both rostral and caudal sides at the body center) and subsequently polished on one side initially using a set of SiC abrasive papers followed by a 50 nm alumina slurry.

4.2.4 **Mechanical characterization by nanoindentation**

Elastic moduli were acquired by nanoindentation (TI 950 TriboIndenter, Hysitron, Minneapolis, MN) with a diamond cube corner tip on polished transverse cross-sectional pieces of a chicken and an acorn woodpecker skull bone. Multiple indentations (N=10 at each location) were carried out with displacement controlled indents to a maximum depth of a 500 nm. The detailed procedure is identical to our previous study [173]. A paired sample t-test was used to compare statistically significant differences of the Young’s moduli between the two different bone regions for each skull bone. The criterion for statistical significance was chosen as $p < 0.05$.

4.3 **Results and Discussions**

4.3.1 **Macroscale structure**

The lateral view μ-CT image of the woodpecker head structure is presented in Figure 4.1a. The upper and lower beaks of rhamphotheca are illustrated with a gray contrast while the upper and lower beak bones are visualized with a bright white contrast. This indicates the difference of X-ray intensities between the two materials. The hyoid bone and skull bones were observed with a white contrast. For a better visualization, a magnified and transparent 3D μ-CT image of the upper and lower beaks (shown in a white dot box in Figure 4.1a, including both the rhamphotheca and bones) is reconstructed, as shown in Figure 4.1b. The difference in length between the upper beak rhamphotheca (light blue) and the lower beak rhamphotheca (yellow) is 0.5 mm (shorter than the previous report by Wang *et al.* [119]). The bones of the upper beak (red) and the lower beak (green) are also shown. The beak rhamphotheca sheath fully covers the upper and lower beak bones, and the upper beak bone is directly connected to the skull bone (as indicated by the yellow arrow, Figure 4.1a). These two different materials/structures and the link between the upper beak bone and the skull bone are critical for initial energy dissipation with subsequent residual stress propagated to the skull bone.

Figure 4.2 shows the anatomies of the skull bone structures for a chicken and an acorn woodpecker based on reconstructions from micro-computed tomography. Figure 4.2a shows the structure of a domestic chicken including the upper and lower beak, frontal, parietal, and jugal bones. The color scale represents the gradation of mineral density (i.e., blue (low density) to red (high density). In general, the lower beak bone of avian species is separated from other bones in the skull, it is only connected to the skull by ligament tissues, as described earlier [174]. The mineral density distribution of the chicken skull bone is quite interesting: the upper and lower beak bones generally have a higher mineral density than the skull; however, the density of the parietal bone seems to be particularly dense, higher or similar to that of the upper and lower beak bones (as shown in Figure 4.2a). Other skull bones (the entire frontal bone and some parts of the parietal bone) appear to have a lower density based on the μ-CT scan data. Because the X-ray intensity

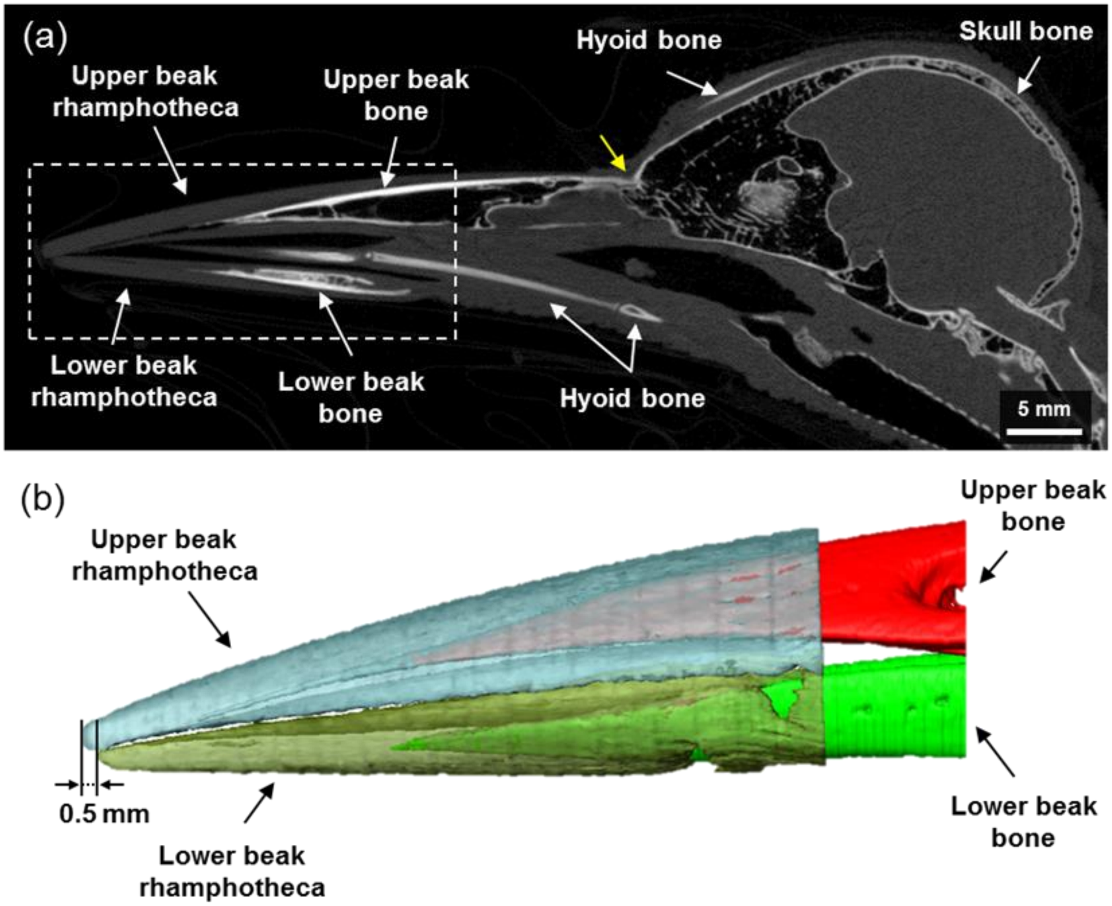

Figure 4.1. Head anatomy of an acorn woodpecker (*Melanerpes formicivorus*) from micro-computed tomography. (a) Sagittal-section view and (b) a transparent three-dimensional reconstructed image of the upper and lower beaks (light blue: the upper beak rhamphotheca, yellow: the lower beak rhamphotheca, red: the upper beak bone, and green: the lower beak bone).

scale of Figure 4.2a and b cannot be normalized due to the lack of use of a standardized material (i.e., imaging phantom) during scanning, only the relative comparison of mineral distribution between the two models is possible. From Figure 4.2, we can estimate which regions may have more mineralized or denser regions, in advance, before selecting the ones that need to be investigated and cut as representative units. Using this insight from the CT-scans, we chose and measured mechanical properties at each selected region. Therefore, the different color distribution

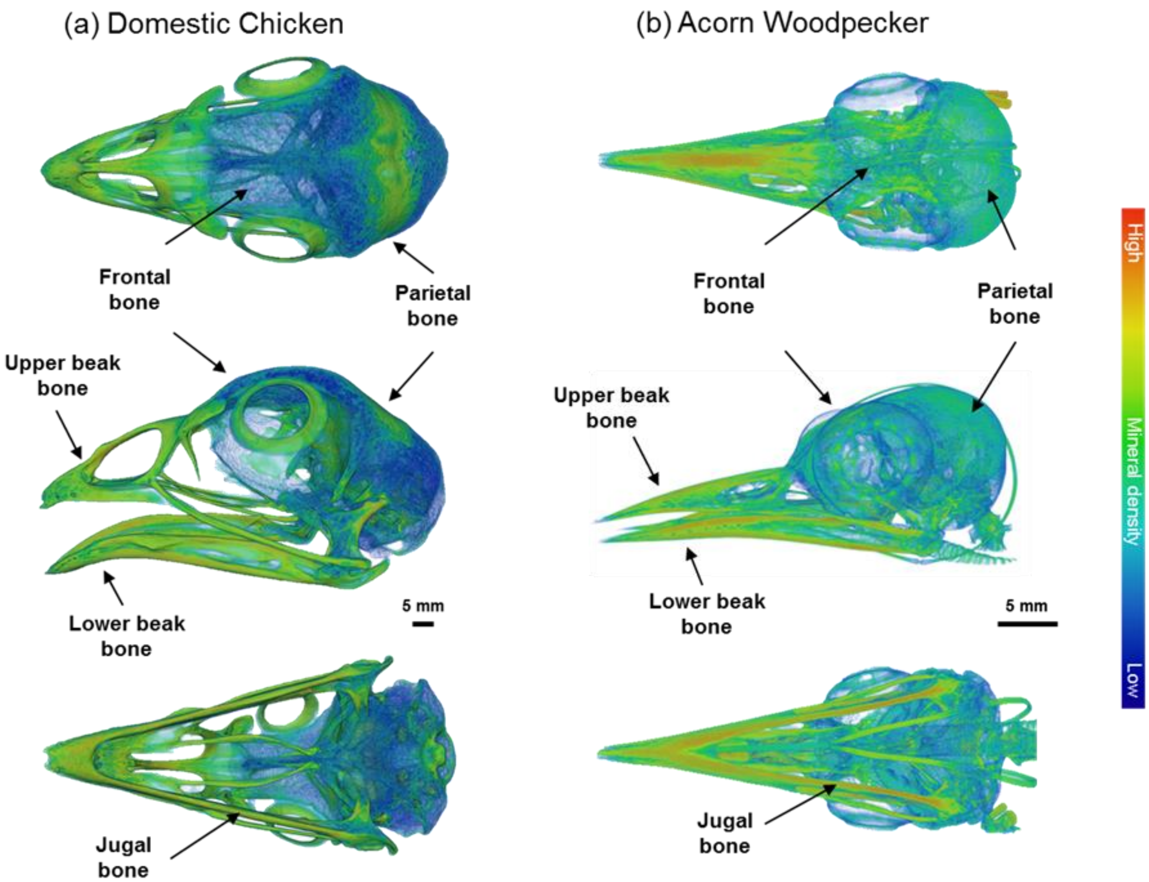

Figure 4.2. Skull bone structures in (a) domestic chicken (*Gallus gallus*) adapted from [165] and (b) acorn woodpecker (*Melanerpes formicivorus*) adapted from [173]. A dorsal (top), lateral (middle), and ventral (bottom) view reconstructed from micro-computed tomography. Note that X-ray intensity scale is not same between (a) and (b) because of the different scanning conditions, therefore, only a qualitative comparison in each species is possible.

for each species (Figure 4.2) is a good indication of different mechanical properties or structural properties as a non-destructive selection tool.

Generally, the anatomy of the woodpecker skull bone is rather similar to that of the chicken but the mineral density distribution is distinct from the chicken skull; the density is relatively homogeneous on the entire skull bone in the lateral view of μ-CT image (as shown in Figure 4.2b, the dorsal view (the middle) image shows no color variation on the skull bone) and is much lower than the upper and lower beak bone densities, as reported by our previous study [173].

4.3.2 **Microscale structure**

Figure 4.3 shows a comparison of transverse cross-sections of a chicken and an acorn woodpecker on the frontal and the parietal bones. In Figure 4.3a, the frontal bone of the chicken presents a rounded T-shape for the cortical bone with a large portion of trabecular bone inside. The parietal bone shows bold lines of cortical bone at the edge, and a large portion of trabecular bone inside the cortical bone. Compared with the chicken frontal bone, the cross-sectional view of the woodpecker (Figure 4.3b) has a sharp, triangular shape, and shows much smaller trabecular and cortical bone thicknesses. Table 4.1 summarizes the μ-CT analytical data for each skull bone. Gibson [121] discussed the scaling effect since woodpeckers have smaller brains than humans, with the smaller brain being advantageous. The chicken showed a larger (76%) total volume of the skull bone (V_s) than the woodpecker. The ratio of the skull bone volume to the head volume (V_s/V_w) of the chicken was 42% larger (0.75) compared to the woodpecker (0.57), indicating that the skull bone volume might be minimized to reduce mass in the latter.

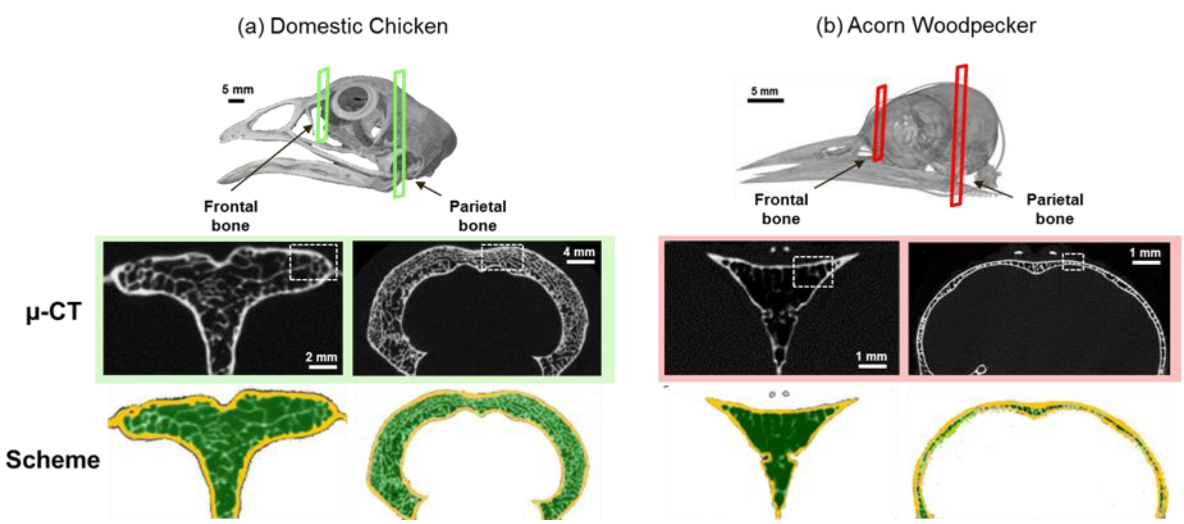

Figure 4.3. comparison of transverse-cross section view of the skull bone structures in (a) domestic chicken and (b) acorn woodpecker. The frontal bone (left) and the parietal bone (right). The bone morphometry quantification data is given in Table 4.1. The quantification was done at the indicated white rectangle regions on each image. In the scheme, yellow lines represent the region of cortical thickness calculation, while green area represents the region of trabecular thickness calculation.

The average trabecular thickness (T_b) of the chicken frontal and parietal bone was larger than the woodpecker due to not only the general scaling effect but also to its lack of flight. The difference in T_b between the frontal and parietal bones is small for both species, indicating the trabecular structure remained: 1) as thin as possible close to minimize the weight even in the non-flying species, and 2) thick enough to support the surrounding cortical bones to act as a structural reinforcement. The average cortical thickness (T_c) shows that the chicken frontal and parietal bones are much thicker than the woodpecker; however, the ratio of the average cortical thickness to the whole head volume (T_c/V_w) of the woodpecker was 57 ~ 64 % higher than the chicken. Compared to trabecular bone, cortical bone consists of a dense and highly mineralized material (i.e., an organic template of collagen mixed with hydroxyapatite, an inorganic mineral) with a multiscale hierarchical structure (i.e., osteon) [4, 13]. Despite its high stiffness, it can also have a good toughness (energy dissipation) thanks to multiple crack-arresting mechanisms [13, 69, 175]. This indicates that the woodpecker skull bones have relatively larger portions of cortical bone than the chicken, which might be helpful to prevent severe damage from impact, providing additional stiffness and energy dissipation.

A bone morphometric analysis was performed to calculate the closed porosity, the tissue volume (TV) and the bone volume (BV). The ratio of the bone volume and tissue volume (BV/TV) of the chicken is two times higher than that for the woodpecker. The calculated porosity varied for each bone, as shown in Table 4.1. The total porosity can be expressed by [176]:

$$\frac{\rho_p}{\rho_d} = (1 - \varphi) \tag{4.1}$$

where φ is a total porosity (volume fraction), ρ_p and ρ_d are the density of the porous and dense material, respectively. If the relative density (ρ_p/ρ_d) in the cellular structures is < 0.3, it can be considered as an open cell structure with the definition of the relative stiffness (or relative modulus) [33]:

$$\frac{E_p}{E_d} \approx \left(\frac{\rho_p}{\rho_d}\right)^n \tag{4.2}$$

where n is a power exponent ranging from 1 to 3 (related to the stiffness of the material; close to 1 for non-mineralized materials and 3 for highly mineralized materials), while E_p and E_d are the Young's moduli of the porous and dense material. If the relative density is > 0.3, it can be described as a closed-cell structure and the relative stiffness can be defined by the following equation [176]:

$$\frac{E_p}{E_d} = \gamma^2 \left(\frac{\rho_p}{\rho_d}\right)^n + \frac{(1-\gamma)\rho_p}{\rho_d} + \frac{P_0\left(1-2v_p\right)}{E_d\left(1-\frac{\rho_p}{\rho_d}\right)} \tag{4.3}$$

where γ is the fraction of solid in the closed cell edges, v_p is the measured Poisson's ratio and P_0 is the gas pressure in the closed pores. The relative densities of the frontal and parietal bones of the chicken and woodpecker are measured following Eqn. (4.1) and the results are summarized in Table 4.1. According to Eqn. (4.1), the frontal bones of both species are considered as closed-cell, and therefore follow Eqn. (4.3), while the parietal bones of both species can be considered as open-cell and follow Eqn. (4.2). According to Eqn. (4.3), a higher closed porosity causes an increased relative modulus due to the cellular densification as a combination effect of cell-wall bending (resulting in enhanced cell-wall stiffness due to their connectivity) and cell-wall buckling/fracture (resulting in edge contraction and membrane stretching as well as enclosed gas pressure) [176, 177]. This increased modulus can be applied to the chicken and woodpecker frontal bones; however, the closed porosity of the woodpecker frontal bone (~21%) is much higher than the chicken (~5%). Thus, the relative modulus of the woodpecker frontal bone is more affected by the amount of the closed pores than the chicken frontal bone because numerous enveloped chambers in the closed pores play a role as pressure vessels. In contrast, for the open-cell of the parietal bones , the degree of mineralization and the total (open) porosity are the only dominant variables to determine its relative stiffness because the relative modulus of the open cell is not affected by other variables [176], implying chemical composition as followed by the degree of mineralization plays more important role in the open-cell foam structure.

4.3.3 Microstructure and chemical composition

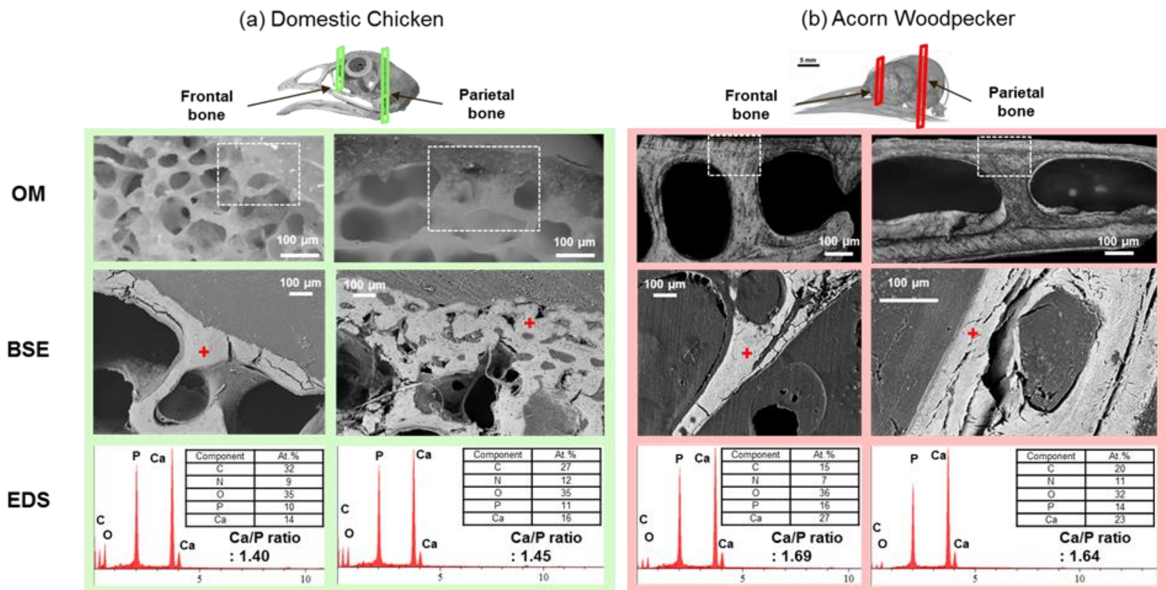

Figure 4.4. Optical and back-scattered scanning electron micrographs of transverse-cross section view of the skull bone structure in (a) domestic chicken and (b) acorn woodpecker. The white rectangles represent the area of higher magnification micrographs of back-scattered scanning electron micrographs. The red cross-hairs represents where the energy-dispersive X-ray spectra were obtained and analyzed.

Zhu *et al.* [162] reported that the Young's moduli of woodpecker skull bones ranged from 4 to 9 GPa and varied according to location. This is likely to be due to underlying chemical and structural differences in specific regions of the skull bone, involving different calcium contents or varying degrees of mineralization within each region. To confirm this, optical and scanning electron micrographs were used to show the bone structure in both chickens and woodpeckers (Figure 4.4). For the chicken frontal bone, an optical micrograph in Figure 4.4a shows the white colored trabecular bone inside. The upper right part of the image shows the cortical bone and the rectangle box indicates the area of higher magnification of a BSE micrograph. For the chicken parietal bone, an optical micrograph shows similar structure to the frontal bone but the higher magnification BSE image (white rectangle box area in the OM image) shows numerous small pores (~ 35 µm in diameter) in the trabecular network. These small pores corroborate the previous μ-CT results that the parietal bone of chickens shows the highest closed porosity. The frontal and parietal bone of the woodpecker show much fewer closed pore spaces, as shown Figure 4.4b. An optical micrograph shows two circular, large spaces (dark contrast), which are surrounded by the cortical and trabecular bone (gray). It appears that closed pore spaces in 2D but the pores are categorized as open because of their connectivity in the 3D analysis. The higher magnification BSE micrograph also shows several larger and smaller circular spaces around the bones. Each cross-section shows the location where the EDS spectrum was acquired. EDS quantification shows differences in mineral content: calcium to phosphorus ratios (Ca/P ratio) of the chicken are 1.40 in the frontal bone and 1.45 in the parietal bone (Ca/P for hydroxyapatite is 1.67), whereas the Ca/P ratios of the woodpecker are higher: 1.69 in the frontal bone and 1.64 in the parietal bone. The semi-quantified values of nitrogen (N) contents, which usually come from organic materials, show relatively higher values (9~12 At. %) in the chicken skull bone than in the woodpecker skull bone (7~11 At. %). Conversely, larger gaps in both calcium (Ca, 14~16 At. % in chickens and 23~27 At. % in woodpeckers) and carbon content (C, 15~20 At. % in woodpeckers and 27~32 At. % in chickens) are found between the two species. The levels of oxygen (O, 32~36 At. %) and phosphorus (P, 10~14 At. %) content remain consistent overall. The presence of carbon is likely from either carbonated calcium phosphate or organic materials. Although the apatitic bones of mammals can be substituted with carbonate ions, it is minimal [13]. Thus, those higher C contents in chickens are more likely due to the higher content of organic materials (i.e., collagen type 1 or other proteins). This implies that the woodpecker skull bone has a higher Ca/P ratio and possibly higher stiffness, when compared to the chicken. The higher Ca/P in the woodpecker might affect the work of fracture and/or toughness; however, the correlation between the microstructure and chemical composition implies that there is a tradeoff: the chicken has a large difference in the amount of closed porosity between the frontal and parietal bone, while woodpeckers show similar level of closed porosity for both bones. To confirm this interpretation, the mechanical properties need to be evaluated at the same locations.

4.3.4 **Mechanical properties**

As shown in Figure 4.2, the discrepancy of the X-ray contrast of the skull bone between chickens and woodpeckers might imply a difference of the mechanical properties for each location. The Young's moduli of the transverse cross-sections of the chicken and the woodpecker skull bones were measured by a nanoindentation method; results are presented in Figure 4.5. In the chicken, the frontal bone (7.3 GPa) has a slightly lower Young's modulus than the parietal bone (9.7 GPa) but this difference is not statistically significant ($p = 0.21$). The woodpecker has a higher modulus in the frontal bone (11.0 GPa) compared to the parietal bone (8.3 GPa) ($p < 0.002$). The frontal bone of the woodpecker has a higher Young's modulus than that of the chicken ($p < 0.020$) and the parietal bone of the chickens has a higher Young's modulus than that of the woodpecker ($p < 0.026$).

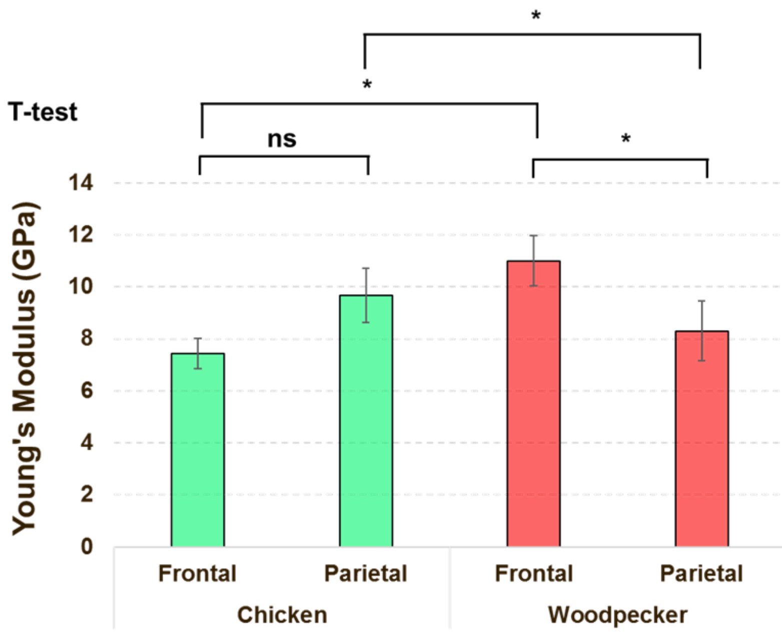

Figure 4.5. Young's moduli from nanoindentation testing of the skull bone in domestic chicken (green) and acorn woodpecker (red). Comparisons where no statistically significant difference was observed are marked with an "ns" symbol. Otherwise, asterisk (*) symbols are marked when $p < 0.05$.

For the woodpecker, the higher modulus of the frontal bone, compared to parietal bone, might be due to a higher Ca/P ratio, which affects the density of the calcium phosphate mineral compounds (i.e., monobasic calcium phosphate monohydrate shows a 0.5 molar ratio of Ca/P and 2.22 g/cm^3 of density, while a 1.67 of Ca/P ratio and a 3.155 g/cm^3 of density for hydroxyapatite) [178]. For the chicken, the parietal bone showed a higher Ca/P than the frontal bone, resulting in a higher elastic modulus. However, the measured elastic modulus is not statistically different; therefore, the effect of the mechanical property mismatch is not significant in the chicken skull bones. In contrast, the measured Young's moduli of the frontal bone of woodpeckers are statistically larger than the parietal bone; thus, indicating that the frontal bone of woodpeckers has adapted with a stiffer and thicker cortical bone, while the parietal bone shows a more compliant and thinner cortical bone. This mismatch of the Young's moduli between the frontal and parietal bones is beneficial to mitigate the propagated impact force/pressure through the skull bone.

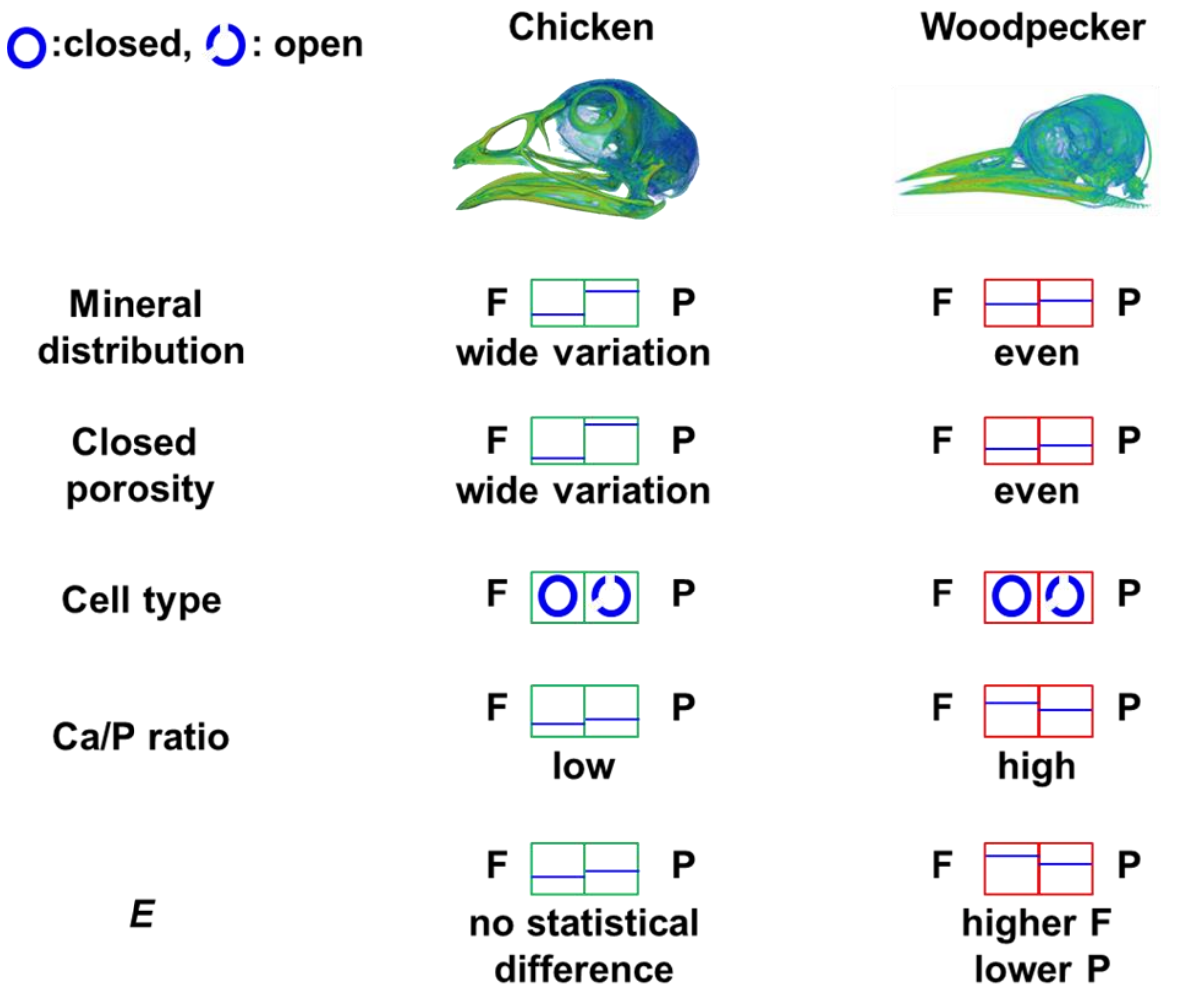

Figure 4.6. Schematic diagram of the summarized main findings. Note that F and P are the frontal and parietal bone, respectively. *E* is the Young's modulus. Blue lines represent relative values of each bone. Blue circles represent the simplified shape of cell type; a closed circle for closed cell, an opened circle for an open cell. Green and red boxes represent the chicken and woodpecker skull bone, respectively. The relative values are rough visual estimations without the upper and lower ends.

4.4 **Conclusions**

This study provides structural, chemical, and mechanical properties towards understanding the impact-resistance of the woodpecker skull. The differences between the skull bones of a chicken and an acorn woodpecker were evaluated. Characterization of structural and chemical properties was performed using optical microscopy, scanning electron microscopy with energy dispersive X-ray spectroscopy, and micro-computed tomography (μ-CT). A bone morphometric analysis was carried out to obtain a relative size of the whole head and brain volume with its ratio, a tissue and bone volume and its ratio, and a closed porosity in the selected volume of interest. Mechanical properties of the frontal and parietal bone were obtained from nanoindentation in both species. The main findings are summarized in Figure 4.6 and described as below:

- The general anatomy of the skull between the chicken and woodpecker is similar but the mineral density distribution is different: the woodpecker shows an even distribution, while the chicken shows variation.
- Variations of mechanical/chemical/structural differences between the frontal and parietal bone are observed. Compared to the chicken, the woodpecker shows:
    - a uniform level of closed porosity (20 ~ 27%), which affects the relative moduli mainly governed by the closed-cell foam structure,
    - the same solid cell type: a closed-cell type in the frontal bone and an open-cell type in the parietal bone,
    - a higher Ca/P ratio (1.64 ~ 1.69),
    - a higher Young's modulus (8.3 ~ 11.0 GPa) than the ones determined for chicken (7.3 ~ 9.7 GPa), based on the experimental nanoindentation measurements.

- For the chicken, the mismatch of cell type between the frontal bone as a closed-cell and the parietal bone as an open-cell results in minimizing the relative modulus in both bones, implying the chicken is not as specialized as the woodpecker skull bone.
- These experimental findings will be useful for further dynamic mechanical simulation or mechanical analyses.

Chapter 4, in full, is a reprint of the material as it appears in Journal of the Mechanical Behavior of Biomedical Materials. Jae-Young Jung, Andrei Pissarenko, Nicholas Yaraghi, Steven Naleway, David Kisailus, Marc Meyers, and Joanna McKittrick, 2018. The dissertation author was the primary investigator and author of this paper.

Table 4.1. Two- and three- dimensional bone morphometry results in a chicken and woodpecker. Note that the brain weight is the median value of its average range taken from [179]. The measured values were presented as the mean with a standard deviation (S.D.).

Parameter	**Chicken**		**Woodpecker**	
Location	**Frontal bone**	**Parietal bone**	**Frontal bone**	**Parietal bone**
Total volume of the skull bone in 3D model (V_s)	13,527 mm^3		3,230 mm^3	
Brain volume (V_b) in 3D, based on the density of the human brain (1,040 kg/m^3 [132])	4,567 mm^3 (or 4.75 g) (*Galliformes* [179])		2,403 mm^3 (or 2.5 g) (*Piciformes* [179])	
Whole head volume in 3D ($V_w = V_s + V_b$)	18,094 mm^3		5,633 mm^3	
Ratio of the skull bone volume to the whole head volume in 3D (V_s/V_w)	0.75		0.57	
Average trabecular thickness in 2D (T_b, μm) (S.D.)	95 (± 27)	82 (± 20)	51 (± 7)	54 (± 5)
Average cortical thickness in 2D (T_c, μm) (S.D.)	166 (± 5)	76 (± 3)	81 (± 2)	41 (± 1)
Ratio of the average cortical thickness to the whole head volume (T_c/V_w, x 10^{-5} mm^{-2})	0.92	0.42	1.43	0.73
Tissue volume (TV, x 10^{12} $μm^3$)	8.73		3.60	
Bone volume (BV, x 10^{12} $μm^3$)	2.50		0.52	
Bone volume / tissue volume (BV/TV, %)	28.6		14.4	
Closed porosity (%) in 3D	4.9	77.1	20.5	27.2
Open porosity (%) in 2D	57.5	3.0	61.3	87.5
Total porosity (%) in 2D	59.6	77.8	69.3	90.9
Relative density	0.404	0.222	0.307	0.091
Solid cell type [176]	Closed	Open	Closed	Open

CHAPTER 5: A NATURAL STRESS DEFLECTOR ON THE HEAD? MECHANICAL AND FUNCTIONAL EVALUATION OF THE WOODPECKER SKULL BONES

5.1 Introduction

Concussion is a form of mild traumatic brain injury (mTBI) caused by external mechanical forces. It is a common occurrence and happens frequently during contact sports (e.g. football, hockey) or from direct or sheer trauma that can occur during vehicle accidents, for example [180]. Repeated exposure to mTBI eventually causes chronic traumatic encephalopathy, a progressive degenerative disorder, resulting in symptoms such as memory loss, decline of executive function, depression, impulsivity, aggressiveness, and suicidal behavior [181].

Woodpeckers peck at trees every day throughout their 15-year life span; however, amazingly, no evidence has been found of chronic TBI or concussion in their brains. Materials scientists and mechanical engineers have attempted to understand and identify key elements of the woodpecker's shock tolerance in terms of biomechanics. With impact conditions reaching decelerations up to 1,200 g, 7 m/s of impact speed, and pecking rates around 20 Hz [30, 129], there are hypotheses stating that woodpeckers have evolved and adapted to absorb the impact energy at the moment of impact [129, 174].

In terms of adaptation and evolution, Bock [174] pointed out that an adaptive beak shape and cranial kinesis (relative movement between the upper jaw and the skull) can explain the shock-absorbing mechanism. The author's hypothesis was inspired by an earlier finding made by Burt [182] that some woodpeckers that hammer more frequently than others present an anatomical adaptation on their skull bone, called the frontal overhang (shown in Figure 5.1a with red arrows). This finding was based on the foraging behavior associated with the main food sources as well as the development of birds (shown in Figure 5.1a and b), and this was the first report regarding a structural specialization on the skull bone [183]. Some suggested other features (e.g., a relatively short leg length and the variation of size of rib bones [108, 184]) that might be related to pecking habits and are described in detail in the Supplementary Materials (5.7.1).

Several researchers have collected data on the mechanical properties of the heads, and more particularly for the skull and beak bones. Gibson [121] described an allometry effect (implying that physical parameters, generally size and mass, scale with certain properties or features) between the human and woodpecker heads in terms of a concussion limit and concluded that this scaling effect enables woodpeckers to avoid brain injury due to the relatively smaller size, the short duration of impact, and large contact area between the brain and the skull bone. This is the first comparative analysis considering the relative size of human and woodpeckers but the interspecies variation was not fully considered (e.g. the body masses of an ivory-billed woodpecker and a golden-fronted woodpecker are up to ~ 570 g and ~ 90 g, respectively). Other mechanical analyses based on computational and experimental results are described in more detail in the Supplementary Materials (5.7.2) including: a simplified two-dimensional finite elemental analysis (FEA) of the whole head impact [132], the mechanical properties of the woodpecker hyoid bone [117], some three-dimensional FEA studies [116, 119, 162, 185], and biomimicking protection devices for microelectronics [133].

Recently, a comparative analysis of the skull bones of woodpeckers and chickens was reported [186], illustrating that the skull bone of woodpeckers showed structural differences such as a relatively small but uniform level of closed porosity, a higher degree of mineralization, and a higher cortical to skull bone ratio than those of chickens. Consequently, it was found that woodpeckers have stiffer bones than chickens, but also that the mechanical properties gradually decrease as one moves from the beak towards the skull, in a gradient fashion.

Regarding the relationship between the pecking habits and anatomical features, here it is hypothesized that the frontal overhang, as observed by Bock [54] and Burt [182], is an evolutionary adaptation among certain species of woodpeckers that is directly correlated with their pecking habits. Therefore, we adopted a strategy to perform a comparative study based on function and morphology. According to Smith [187], this approach includes the following steps: 1) an analysis of shape and behavior about a key element on the structural function and role in the natural environment of animals (shown in Figure 5.1a and b), 2) a phylogenetic analysis from the morphology (shown in Figure 5.1a and Figure 5.5), 3) a selection of a valid model of function (Figure 5.1c), 4) building hypotheses about the relationship between function and structure, 5) expectations for morphological variance in terms of the model of function compared to knowledge of animal's behavioral differences, and 6) performing a test to validate the hypotheses with comparative analysis (across Figure 5.2 and Figure 5.3).

Following the hypothesis formulated above, this study aims to confirm whether anatomical differences on the frontal bone in some species of woodpeckers present any mechanical advantage in relation to their reported behavioral/food habits.

A morphological comparative analysis (as shown in Figure 5.1c) shows different skull bone structures between two woodpeckers: a white-headed woodpecker (more frequent pecking) and a golden-fronted woodpecker (less pecking). In Figure 5.1c, each bone is shown with a different color. Note that the nasal-frontal hinge (yellow color) is generally a movable joint at the interface between the upper beak bone and the frontal bone, for common avian species, but most woodpeckers show prokinesis, meaning that the hinge is located between the frontal and nasal bones [54, 174]. Based on the micro-computed tomography (μ-CT) results reported by Jung et al., [186] as well as shown in Figure 5.1c in this paper, this hinge structure was completely fused to the frontal bone (in a male, adult specimen). Therefore, the nasal-frontal hinge, including the frontal overhang (yellow in Figure 5.1c) was not considered as a movable joint in our further mechanical analysis. A sagittal-section view of two woodpeckers showed an emphasis on the overhang structure by having a different angle between the frontal bone and the upper beak bone. The dotted lines with a red color were drawn along the upper edge of the upper beak bone and the frontal bone to represent the angle (α in Figure 5.1c) and shape in two dimensions. Those lines were copied and re-drawn in two-dimensional (2D) scheme images, where red represents the upper beak bone and yellow represents the frontal bone. The results show that for the white- headed woodpecker, the hinge on the upper beak bone does not intersect with the upper beak bone, and the hinge opening angle (α) is smaller than 90˚, as shown by the two lines on Figure 5.1c. On the other hand, the upper beak bone and the frontal bone of the golden-fronted woodpecker intersect each other without any gap in between, this time with a larger hinge opening angle ($\alpha > 90°$), as illustrated by the single red line. When reconstructed and visualized in three-dimensions (3D), the differences become clearer: there is a shaded region near the interface between the upper beak bone and the frontal bone on the white-headed woodpecker, whereas the golden-fronted woodpecker has a smooth interface in the same region. From the μ-CT scan results (shown in Figure 5.1c, right), it is confirmed that there are structural differences of the skull bone of woodpeckers among different species, which can potentially be related to pecking habits and food sources (presented in Figure 5.5). Based on the findings that some woodpeckers indeed possess a frontal overhang structure while others do not, a further identification of the structural role of the frontal overhang needs to be performed.

5.2 Experimental and computational approach

Micro-computed tomography (μ-CT): An acorn woodpecker (*Melanerpes formicivorus*) was scanned by micro-computed tomography (μ-CT, SkyScan 1076, Bruker microCT, Kontich, Belgium) in our previous paper [173]. Raw data of three others woodpeckers, an ivory-billed woodpecker (*Campephilus principalis*), a white-headed woodpecker (*Picoides albolarvatus*) and a golden-fronted woodpecker (*Melanerpes aurifrons*) were obtained from digimorph.org operated by High-Resolution X-ray CT Facility at the University of Texas, Austin. Each skull bone was visualized and analyzed using Amira software (FEI Visualization Sciences Group, Burlington, MA). After verifying the 3D volume rendering models for each skull, an image segmentation process was carried out based on X-ray intensity to generate a 3D mesh model of the skull bone.

Mesh model generation for simulation and 3D printing: GeoMagic (3D Systems, Morrisville, NC) and GMSH software [188] were used to fix triangulation errors obtained from the initial reconstruction with Amira and to generate the solid finite element (FE) meshes.

3D printing of skull models and impact testing: The woodpecker skull models were printed out using a 3D printer (Object 350 connex3, Stratasys, Eden Prairie, MN). A VeroClear material (Young's modulus: 2 ~ 3 GPa, density: 1.20 ~ 1.30 g cm^{-3}, transparent material) was used to print the skull bone models. A custom-built drop weight test tower was used to simulate the impact of the beak and skull bones, a detail description of dimensions and specifications can be found in our previous work [104].

Dynamic finite element analysis (FEA): Dynamic FEA of an impact event between the woodpecker skull and a rigid solid plate was carried out on a commercially available software (Abaqus/Explicit). The skull was slightly rotated to align the main axis of the beak, calculated by finding the best fitting plane of symmetry, with the direction of pecking.

Frequency modal analysis: Frequency modal analyses of the two models were performed to identify the natural modes of vibration, and to evaluate the effects of the added mass and volume on the natural frequencies of the woodpecker skull due to the added overhang. Subsequently, dynamic impact cases with a Ricker Pulse input, along the direction of pecking at the tip of the beak, were simulated. The Ricker pulse produces an impact with a known spectrum, and results in a clearer acceleration profile of the structure in the frequency domain.

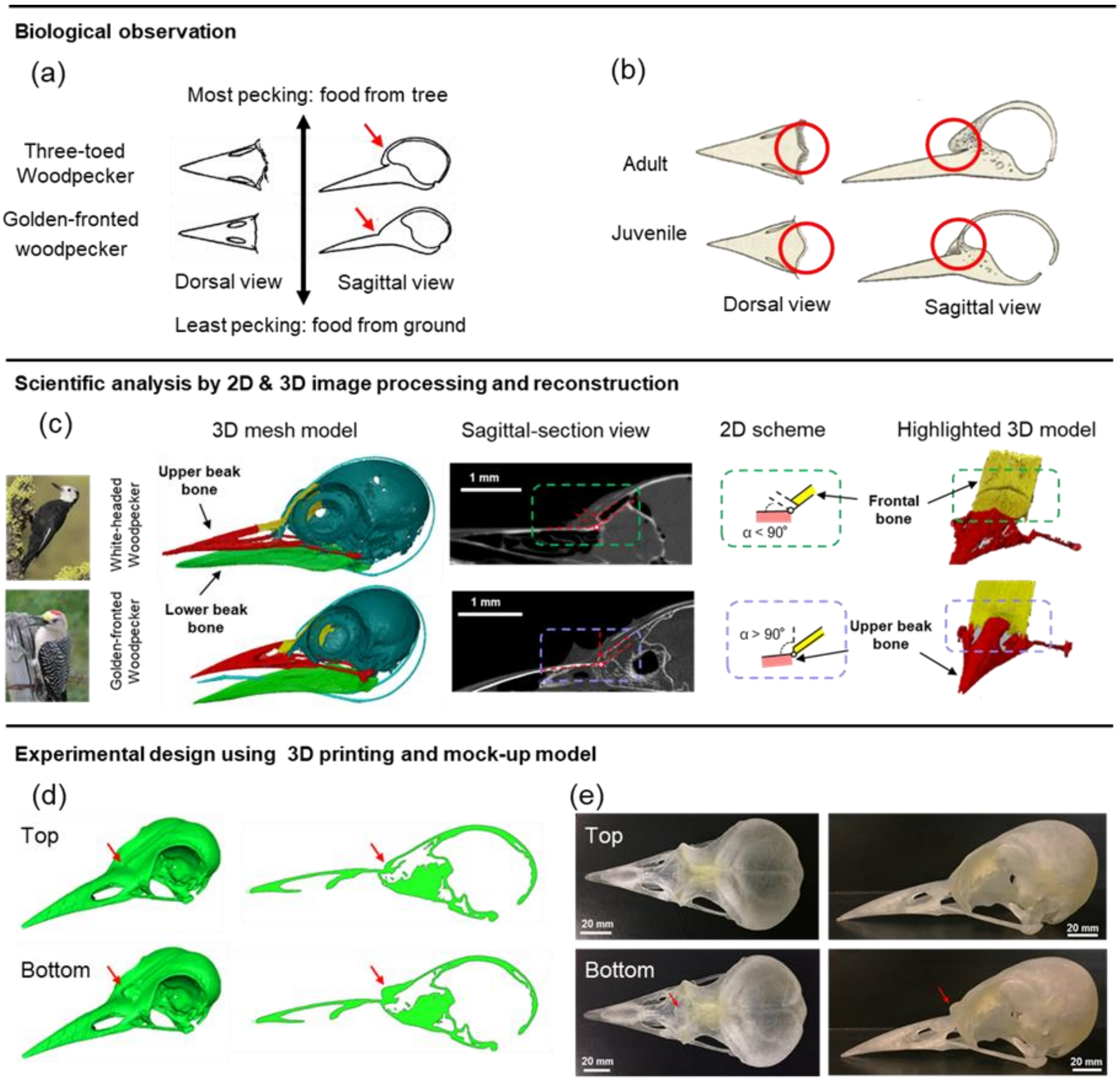

Figure 5.1. An example of how a biological observation becomes a scientific design and experiment. A representative anatomical adaption of the skull bone based on the relationship between food source and pecking behavior in woodpeckers, showing (a) two representative species chosen from nine different woodpecker species reported by Burt [182] and highlighted by Bock [189] and (b) the differences of the skull bone between the adult and juvenile birds. (c) A comparison of different skull bone structures between a white-headed woodpecker and a golden-fronted woodpecker: (left to right) photographs of two woodpeckers, its three-dimensional reconstructed model of the skull and beak bones from micro-computed tomography, two-dimensional images of sagittal-section views, and simplified schemes of two adjacent bones (the frontal bone and upper beak bone), and highlighted 3D models. (d) Two models of the skull bone for dynamic finite element analysis and frequency modal analysis: (top) the reconstructed original model, mimicking a golden-fronted woodpecker, and (bottom) the model with the artificial overhang, mimicking a white-headed woodpecker. The images on the right side are the view-cut sections along the sagittal plane. (e) 3D printed skull models using a transparent material (the same dimensional order as Figure 5.1d).

To simplify and facilitate the comparison between the overhang and non-overhang species, 3D models of solely the golden-fronted woodpecker were generated from the μ-CT scans, as shown in Figure 5.1d (top). On one model, an artificial overhang was added with an increased volume on the frontal bone, mimicking the frontal overhang structure found in the white-headed woodpecker (shown in Figure 5.1d, bottom). View-cut sections were made at the centroid and the pseudo-symmetry plane to highlight the morphological changes between the two models. Then, 3D printed skull models (scaled up by a factor of three to facilitate experimental procedures) were obtained as shown in Figure 5.1e (top: a no overhang model, bottom: an overhang model).

To test our hypothesis that the skull bone of woodpeckers has adapted to avoid brain injury, impact testing of the 3D printed skull models was implemented so as to best reproduce the pecking conditions of woodpeckers. A wooden plate was first considered for a realistic pecking condition with an impact speed of 7 m/s. However, the plates would absorb most of the impact energy showing dents on their surface while the 3D skull models would not show any sign of failure or damage. In contrast, a worst-case scenario was implemented by impacting against a metal plate. An experimental setup to obtain the accelerations of the skull bone near the brain in three axes using a customized drop-weight test tower is presented in Figure 5.2a. A maximum impact speed of 3.3 m/s was achieved from the maximum height with a customized, 3D printed impact guide, adjusting and holding the angle of impact of the woodpecker skull (Figure 5.2b and c). A three-axis accelerometer was attached to the skull model to measure the accelerations at the moment of impact (Figure 5.2b, right).

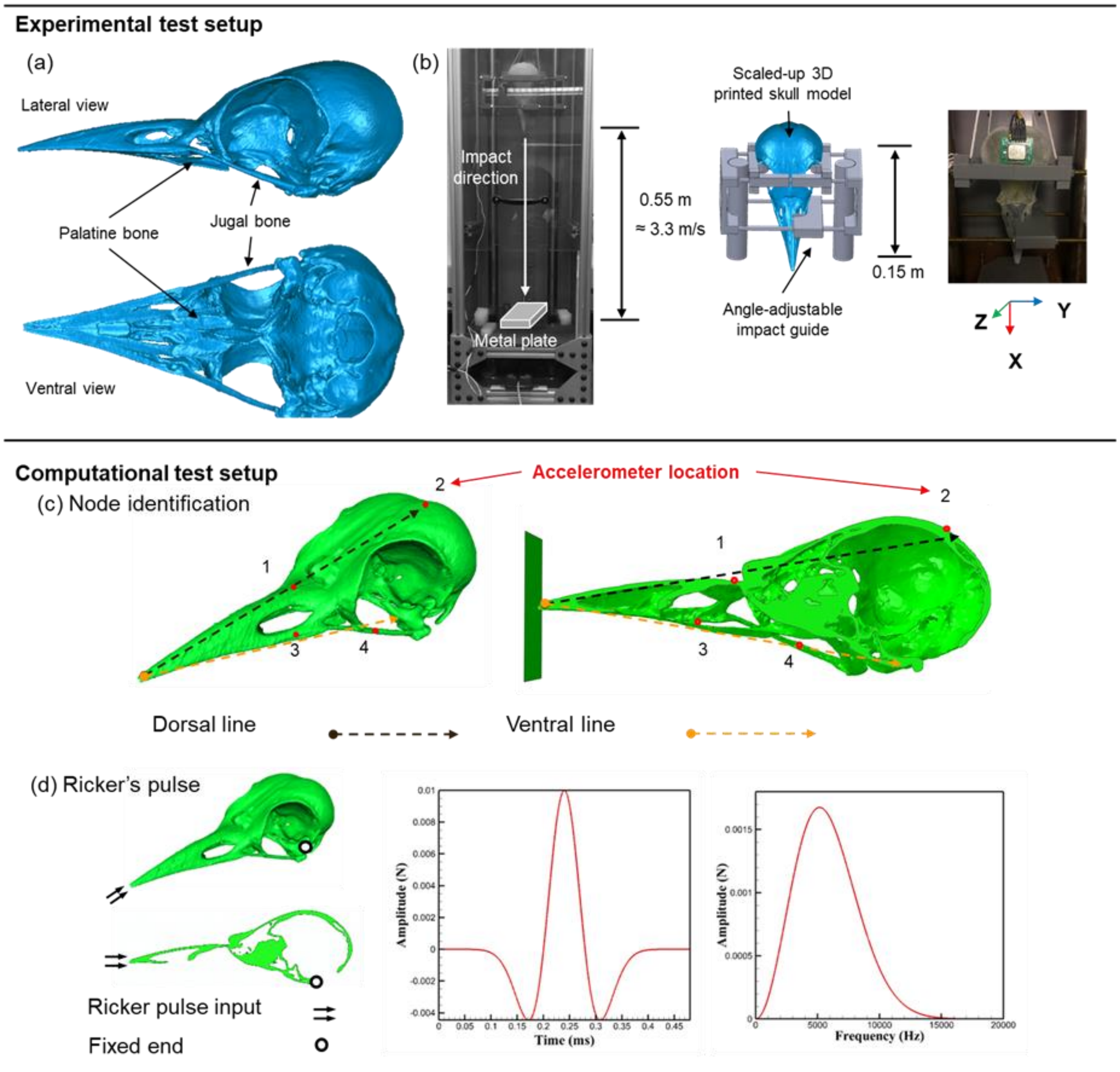

Figure 5.2. An illustration of experimental and computational test design of an impact test using 3D printed woodpecker skull models. (a) Lateral (top) and ventral (bottom) views of the 3D reconstructed skull models with its anatomy. Each arrow indicates the palatine and jugal bone, respectively. (b) A photo of an impact test drop tower (left), a CAD design of a custom-built 3D printed impact guide (middle), and a photo of 3D printed skull loaded on the tower with an impact guide with an attached accelerometer (right). The maximum drop height and impact speed was adjusted due to the height of the impact guide. (c) Node identification of each region of interest, 1: the caudal end of the upper beak bone, 2: on the parietal bone near the brain (the accelerometer attached location), 3: on the palatine bone, and 4: on the jugal bone. (d) Schematic illustration of the Ricker's pulse input and the fixed end location considered in the frequency modal analysis (left), in time (middle), and frequency domain (right).

A modal analysis was performed in on Abaqus/Standard to characterize the frequency response of the wood pecker under free vibration response. Some representative nodes on the main pathway of stress waves are identified as shown in Figure 5.2c: two points along the dorsal line (node 1 and node 2) as well as two other points along the ventral line (node 3 and node 4). Note that the node 2 is at the identical location where the accelerometer was attached on the 3D printed skull model. Then, further validation of the modal analysis was performed using Abaqus/Explicit where a Ricker's pulse input, allowing a correlation between the propagation of stress waves in a time domain space and the principal frequencies that are excited during impact events in the woodpecker's skull. Ricker wavelets are widely used in seismic and vibrational studies because these can be uniquely specified with only a single parameter that corresponds to its peak frequency on the wavelet's frequency spectrum [190-192].

5.3 **Results and Discussions**

From the experimental results, accelerations were measured in all three axes of the no overhang model at an impact speed of 3 m/s (Figure 5.3a). Note that the main impact direction is along the X-axis (red arrow). The first peak of the measured acceleration over time in the X-axis showed the highest value of acceleration (max 529 *g*) compared with other axes. The impact duration, corresponding to the width of the first peak, is approximately 1 ms. After a few minor fluctuations, the accelerations were dampened by less than a half at the second peak in the X-axis (190 *g*). For the Y-axis, which is an indication of the lateral movement of the skull model (left and right motion of the 3D printed model in Figure 5.3a), the acceleration peaks were much smaller than the X-axis. It means that the lateral displacement (and/or vibration) of the skull model is much smaller than the X-axis at the moment of impact. The maximum intensity of accelerations on the Z-axis was between those of the X-axis and Y-axis, the maximum peak was found at a 400 *g*. The relatively lower peaks were observed until 5 ms in the Y-axis. Displacement in the Z-axis can be explained by the dorsoventral motion of the skull, corresponding to up-and-down oscillations with respect to the Z-direction. This motion in the Z-axis is initiated after the first peak in the X-axis, i.e. after release of the impact. Movements in each of the three-axes can contribute to processes of impact energy dissipation by dampening specific oscillations that could potentially be harmful to the brain.

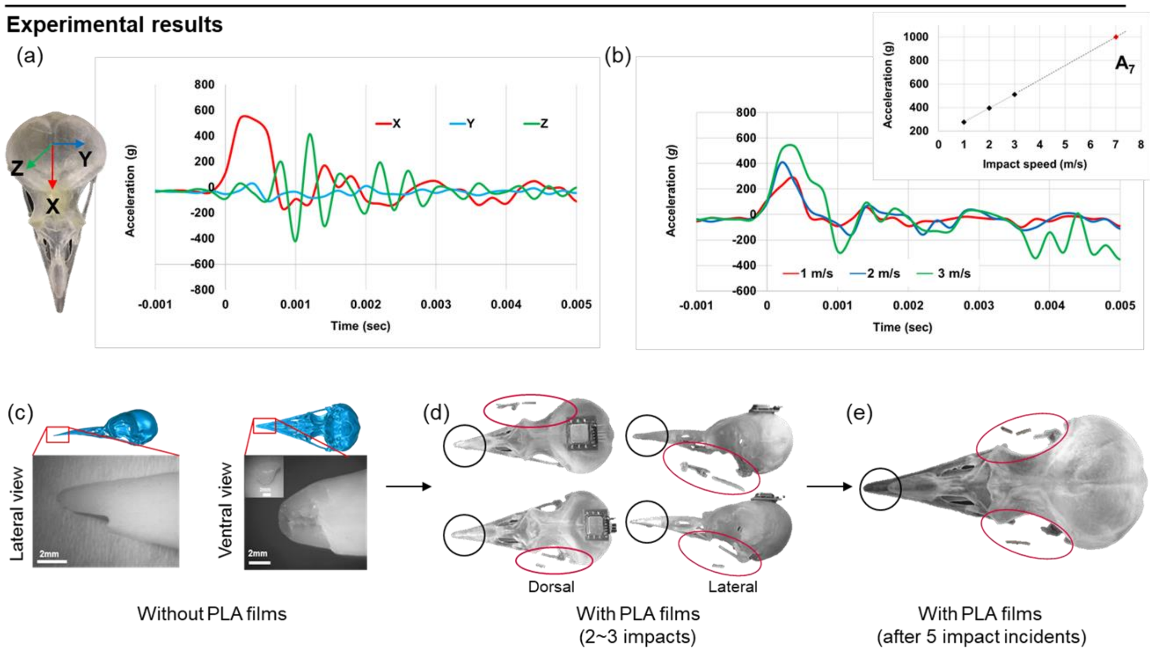

Figure 5.3. Experimental results of the impact testing with 3D printed skull models. (a) Measured acceleration on the skull bone near the brain in an impact speed of 3 m/s for three-axes. (b) The effect of different impact speeds at 1, 2, and 3 m/s on the accelerations at the X-axis. Note that an inset plot shows the linear regression line of acceleration at a 7 ms^{-1} (A_7). (c) Photos of damaged skull models without the beak cover. (d) After using a PLA wrap (black circles) to mimic the keratinized sheath in the beaks, the damages of the skull models were mainly found on the jugal bone after 2~3 times of impacts. (e) After 5 times of impact incidents: only the jugal bones were damaged. Note that other structures were remained intact.

The effect of the impact speeds in the X-axis at a 1 m/s, 2 m/s, and 3 m/s on the acceleration profile were studied; results are shown in Figure 5.3b and Figure 5.6 (see detail in Supporting information, 5.7.3). Due to technical limitations of the experimental setup, a 7 m/s impact speed was not tested directly. The results showed that the peak amplitude of acceleration linearly increases with higher impact speed. The pattern of the acceleration profile remains similar among the three tested speeds, while the impact duration remains unchanged. Based on the results, we can estimate the amplitude of accelerations at the impact speed of 7 m/s, which is the maximum value that has been recorded for woodpeckers. From a simple linear regression, the peak acceleration of 7 m/s can be estimated at 1,000 *g*. By scaling it down to the real size of a woodpecker skull, we find that acceleration would reach about 6,800 *g* for the real case (for calculation see Supplementary Materials 5.7.6) which shows a good agreement with other reported pecking conditions (1,200 *g* in the original scale in a real bird) [30, 129], meaning that our experimental impact testing with 3D printed skull models can serve as a basis for comparative analyses with real life cases.

Analysis of failure of the skull models after impact testing can serve as valuable information, because in vivo testing that resulted in damage to the skull bones of living woodpeckers would not be possible without sacrificing a bird. In addition, because the 3D printed skull and beak have essentially the same material properties unlike the real bird, it allows to analyze the sole effect of the structure specifically. Note that the black circles in Figure 5.3d-e indicate the tip of the beak, which was wrapped with a polylactic acid (PLA) shrinkable film to protect it from breakage during impact testing, after several trials and errors. Before wrapping with the PLA film, the printed skull models would sustain damage at the tip of the beak as shown in Figure 5.3c. After several tests, the same type of damage at the tip of the beak was observed repeatedly; we therefore utilized the PLA film to wrap around the tip of the beak to protect this part from breakage. By protecting the beak tip, we can observe if other structures can be damaged after impact. Breakage was mostly found to happen at the jugal bone, generally after two or three impact tests, as shown in Figure 5.3d. The jugal bones were the only damaged structures we found on both no overhang (top) and overhang models (bottom) highlighted with red ellipses. By performing the same test on the same sample at 5 times, both sides of the jugal bones would completely break, while other structures would still remain intact, as shown in Figure 5.3e. The failure analysis of the 3D printed skull models implies that the impact energy may be dissipated at the tip of the beak and the jugal bones. The other parts of the internal skull bones were examined but remained intact after five impact incidents. In nature, the tip of the beak bone is protected by the keratinized sheath (called the rhamphotheca [186]), and jugal bones, as well as other parts of the skull, are mainly surrounded by soft tissue. Nonetheless, the failure analysis allows one to identify areas that are the most sensitive to breakage in the skull.

Frequency modal analyses of the 3D printed skull model were performed to evaluate the natural frequencies of the skull bone structure. According to Laksari et al., [193] repeated low-acceleration head impacts may cause mild brain trauma in humans, therefore, understanding the skull-brain dynamics is important. The authors reported that a low-frequency resonance between the skull and the brain in humans occurred at ~ 15 Hz in an under-damped system (the system oscillates with decreasing amplitude to a convergent point) and more commonly at < 20 Hz in other contact sports. This resonance can amplify the relative brain-skull motion, which is more likely to cause brain damage. In primates and humans, low-range natural frequencies (5-10 Hz) were observed for rotational brain motion [194]. However, the resonance frequencies of the skull were reported around 1,000 Hz in humans during head impacts. As a boundary condition, we fixed the models at the point where the skull meets the neck and calculated the first five modes of natural frequency. The five calculated modes are presented in Figure 5.4a, showing the five (possible) structural free oscillations, which depend of the stiffness of the structure k (and henceforth its Young's modulus E (GPa), density ρ (Kg m^{-3}), and effective length L (m)) and its mass m (g), as indicated by the following relationship:

$$f_n = \frac{\alpha_n}{2\pi}\sqrt{\frac{k}{m}} = \frac{\alpha_n}{2\pi}\sqrt{\frac{EI}{A\rho L^4}} \tag{5.1}$$

where f_n is natural frequency in hertz (cycles/second), I is the second area moment of inertia (kg·m^2), A is the equivalent cross-sectional area (m^2), L is the effective length (m), and α_n is a parameter that depends on the boundary conditions and the vibration mode.

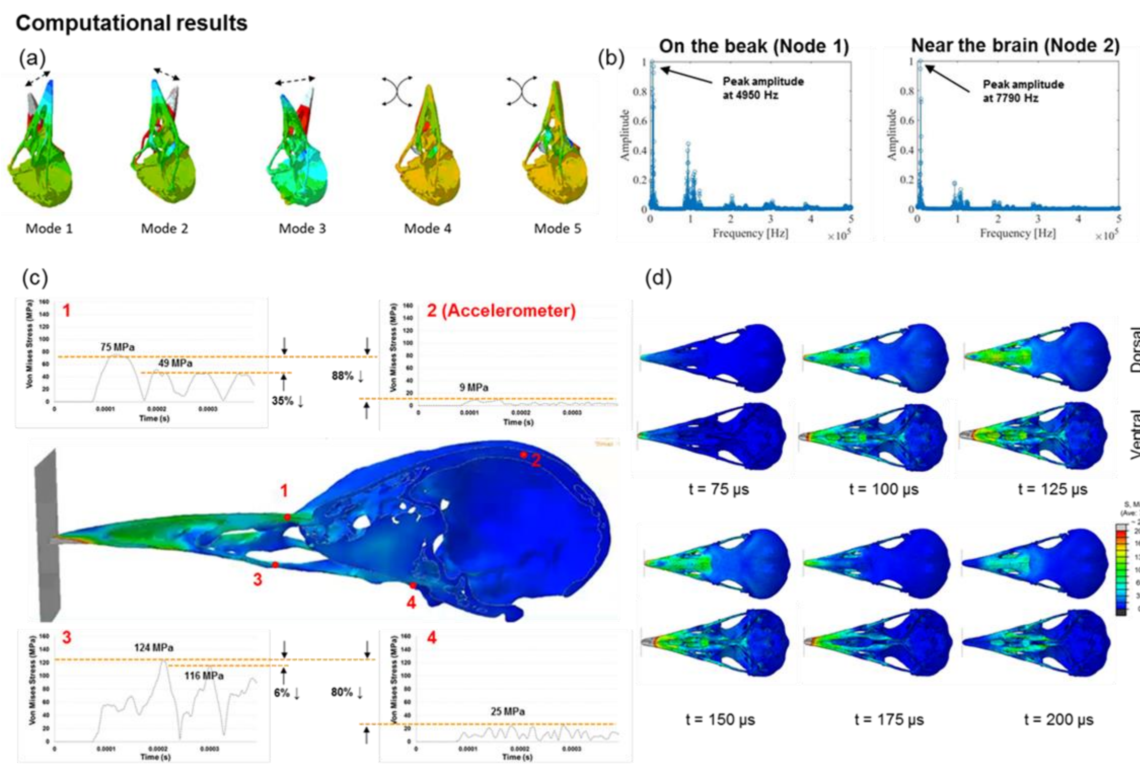

Figure 5.4. Computational results of the impact testing with 3D meshed skull models. (a) Five natural frequency modes associated with the vibration of the skull. (b) A representative result of Ricker's pulse analyses at node 1 and 2. (c) The sagittal-section view of the skull model and the plots of von Mises stress at four nodes. 1: On the upper beak bone prior to the interface between the upper beak and the frontal bone. 2: On the parietal bone near the brain (where an accelerometer was attached in the experimental setup). 3: On the palatine bone. 4: On the jugal bone. (d) Time-lapse images of von Mises stress distribution on the skull bone models during the woodpecker's pecking at a 7 m/s of impact speed.

Each mode corresponds to a specific motion at a certain excited frequency: up and down (along the z axis) bending motion of the skull bone for modes 1 (4,790 Hz), 2 (7,026 Hz), and 3 (7,458 Hz) and twisted torsional motion between the palatine and jugal bones for mode 4 (8,146

Hz) and 5 (10,024 Hz). The average frequency of the sideways motion of the 3D printed skull model, recorded with the high-speed camera, was found to be 629 Hz (see the detail in Supplementary Materials, 5.7.4 and Figure 5.7). This value, when taking into account the model relative size and the material stiffness compared to the real skull, is equivalent to 4,257 Hz (see the detail in Supplementary Materials, 5.7.4 and 5.7.6) a result that can be assimilated to the first natural frequency (4,790 Hz). Considering the size of the skull and brain of woodpeckers, the traumatic resonance in woodpeckers might occur at a much higher frequency range than for humans (due to a smaller mass, following the allometric relationship in equation (5.1)). However, the mechanical properties of the brain of woodpeckers (for example, stiffness (k) in equation (5.1)) have never been reported; hence, an accurate calculation of the natural frequency of the woodpecker brain and followed with an assessment of the resonance frequency between the skull and the brain of woodpeckers are impossible at this time. However, we can expect that the natural frequency of the woodpecker brain should remain low (below 4,000 Hz) to avoid synchronized resonance with the skull bone. This is nevertheless an interesting subject for future work, that could extend Gibson's allometry analysis [121].

Ricker's pulse simulations and the associated frequency spectrum analyses were performed to obtain a clear visualization of excited frequencies after impact, contrary to the case of a direct impact input that can result in noisy data. As shown in Figure 5.4b, the dominant frequencies of the skull bone at the node 1 and node 2 appear to be around 4,950 Hz and 7,790 Hz, respectively. No frequencies < 4,000 Hz are observed. For a comparison between two nodes on the skull bone model without the overhang, node 2 shows a peak amplitude at a higher frequency than node 1 (on the beak), implying that the structure of the skull bone is designed to be isolated from the vibration from the beak. The effect of body mass/volume on the frontal bone between two models (with and without the overhang) does not seem to show any difference in terms of calculated natural frequencies and the distribution of peak amplitude at these frequencies (Figure 5.4b) which seems to imply that there is no discernable effect of the frontal overhang in exciting different vibrational frequencies.

To analyze the stress wave pathway during pecking in the normal direction, a dynamic impact analysis was conducted with a 7 m/s of speed. The evolution of the von Mises stress over time after impact for the skull model is plotted in Figure 5.4c. The values are taken at the four specific nodes described on Figure 5.2c. Along the dorsal line (through nodes 1 and 2), node 1, located ahead of the frontal overhang showed the highest stress level (max peak ~75 MPa), and then, the value dropped by 35% at the second peak. The maximum stress level decreased significantly at node 2, with a peak value 88% lower (max ~ 9 MPa) than at node 1. Along the ventral line, a similar pattern can be observed; node 3 shows a higher stress level (max ~ 124 MPa right after impact, then a second peak at ~ 116 MPa) than node 4 (max ~ 25 MPa). See the detail in Supplementary Materials, 5.7.5 and Figure 5.8). Among all these nodes, node 3 is the one undergoing the highest stress level, implying that the four main oscillation cycles are observed at every location correspond to the dorso-ventral motion of the upper beak after impact, as discussed above. Note that the general trend on the dorsal and ventral line between the two models is almost the same, the addition of body mass (in the model) does not seem to affect the stress levels on the skull bones. However, a higher stress level was observed along the ventral line, which indicates that the pathway of the stress propagation comes from the upper beak bone to the bottom of the skull bone and the neck and eventually to the rest of body. The variation of the stress on the dorsal line seems not related to the frontal overhang sizes, but a higher level of stress on the ventral line may suggest that the morphology of the skull bone structure is beneficial to deflect the main stress wave toward the bottom part of the skull bones, rather than towards the brain. In addition, the highest stress level was found to be reached at the beak tip (grey color in Figure 5.4c, with values above 200 MPa), which shows a good agreement with the failure analysis of the damaged 3D printed skull models, as shown in Figure 5.3c.

A time-history of the stress distribution shows how the stress wave propagates through the skull bone at each time step, as shown in Figure 5.4d. The first impact occurrs around 75 µs, when the tip of the upper beak bone shows a change of stress level. Around 100 µs, the first stress wave reaches the caudal end of the upper beak bone and the rostral end of the frontal bone. The highest stress level in this region was observed around 125 µs, after which the stresses decrease down to zero around 200 µs. The first stress wave fully propagated along the dorsal line around 200 µs, after which a second wavefront traverses the dorsal line. On the other hand, along the ventral line, the first stress wave reaches its peak at node 3 at 100 µs and at node 4 at 150 µs, respectively. Overall, a notable fact is that the stresses remain at a relatively lower level (~ 9 MPa, as shown in Figure 5.4c(2) and d) near the braincase during the propagation of the first shockwave, i.e. until 200 µs. As a result of the stress analysis, it is found that there are no notable differences between the two skull models, either with or without a frontal overhang. This implies that the natural structure of woodpecker's skull bone was designed to minimize the stress propagation from the upper beak to the brain-case, which can intrinsically serve as a mechanism to protect its brain.

5.4 Conclusions

To confirm the structural differences on the skull bone structure in woodpeckers, micro-computed tomography was utilized to investigate three-dimensional shape between two species: white-headed and golden-fronted woodpeckers. Based on the biologist's observation according to Smith, we hypothesized that the anatomical differences on the skull bone can be affected by the different food sources and the different pecking habits, so as to have a better mechanical function against mechanical impact or shock. To test this hypothesis, a three-dimensional mesh model of a golden-fronted woodpecker was developed and an artificial overhang feature was added on the model, mimicking the white-headed woodpecker skull bone, to assess its potential benefit in brain protection. An experimental test with a customized drop weight impact testing tower with 3D printed plastic skulls, as well as dynamic finite element analyses, were conducted for each model to obtain acceleration vs. time curves, observe failure modes of impacted 3D printed skull models, identify natural frequencies, and record the free vibrations of the structures after impact with frequency spectral analyses, and determine von Mises stress levels at each pre-defined node. The main findings are:

- A drop tower impact testing setup using 3D printed skull models showed the peak accelerations in the X-axis as the main impact direction. A vibrational motion along the Z-axis was found, indicating a dorsoventral motion of the whole skull model.

- From the 3D printed skull models, failure analysis showed that the beak tip and the jugal bones are the mainly damaged structures during dynamic impact.

- Natural frequency and Ricker's pulse analysis showed that the five representative natural frequency modes correspond to two different vibrational motions: the dorsoventral motion of the skull bone and the twisted torsional motion between the palatine and jugal bones.

After pulsed impact, a higher resonance frequency was found on the skull bone near the brain than on the beak bone. This results can be applied to materials development for frequency control. While using frequency mismatch is a common practice in structural engineering, this result is a good example of bioinspired frequency control attained through the modification of only geometrical parameters and can be applied to a design strategy for protective head gears in contact sports. Further characterization of other anatomical features and their contribution with impact mitigation may also help deepen understanding of this bioinspired approach.

- von Mises stress analysis showed that the main stress wavefront from the impact at the beak tip propagated through the ventral line (the jugal bones) of the head towards the neck/spine. The von Mises stress level near the brain remained at a significantly lower level than the rest of the skull bone structure.

- Without sacrificing a living animal, we were able to test our hypothesis and answer the question: what is the structural role and benefit from the frontal overhang on the skull bone woodpeckers. Although the effect of the frontal overhang on vibrational motion was negligible, we found that, more importantly, the skull bone is naturally designed to limit the stress wavefront towards the body rather than the braincase during pecking.

- Both 3D printed skulls and computational models developed in this study can be used to further identify and assess a dynamic interaction between the skull and brain (i.e., using a gel-like brain surrogate material) in woodpeckers to represent a non-traumatic brain injury animal model, as a future direction of this study.

5.5 Future work

- Through this manuscript, an isotropic, continuous, and homogeneous 3D printed model was implemented, which provides a better, simpler understanding of the isolated anatomical features solely. However, a natural bone has a hierarchical structure with different materials forming an organic-inorganic composite; the energy absorption mechanism is thus different from our 3D printed beak-skull models. In order to mimic the natural bone and analyze the impact resistance of the real beak-skull bones, a composite structure combined with organic and inorganic materials can be printed out together through an advanced 3D printing technique as one of our future goals.

- In addition, we have performed a failure analysis of the 3D printed skull models in micro scale, but a micro scale damage analysis is worth investigating when considering some printing conditions, such as a curing, orientation of material stacking, and adhesion/tearing forces between two materials if we can print multiple materials simultaneously. This work can be our next step in failure analysis using different 3D printing configurations against mechanical impact, as we are also attempting to avoid testing on actual biological samples.

- The effect of a hinge opening angle (α) between the frontal bone and the beak bone (earlier mentioned in Introduction) was found to be negligible. The relationship between the hinge opening angle and the level of stress propagated through the beak and skull bone models in relation to reported pecking habits will be an interesting topic to examine, although the angle was only used to quantify the main structural difference between two woodpecker species to focus on whether the presence of the frontal overhang or not in this manuscript.

- Our approach to build two comparative skull models is started as we add up the artificial frontal overhang on the skull of the non-overhang species (acorn woodpecker); however, the alternative method to artificially remove the frontal overhang structure on the skull of the overhang species (white-headed woodpecker) can be an interesting approach for comparison.

5.6 **Experimental Section**

Micro-computed tomography (μ-CT): An acorn woodpecker (*Melanerpes formicivorus*) was scanned by micro-computed tomography (μ-CT, SkyScan 1076, Bruker microCT, Kontich, Belgium) in our previous paper [173]. Raw data of three others woodpeckers, an ivory-billed woodpecker (*Campephilus principalis*), a white-headed woodpecker (*Picoides albolarvatus*) and a golden-fronted woodpecker (*Melanerpes aurifrons*) were obtained from digimorph.org operated by High-Resolution X-ray CT Facility at the University of Texas, Austin. Each skull bone was visualized and analyzed using Amira software (FEI Visualization Sciences Group, Burlington, MA). After verifying the 3D volume rendering models for each skull, an image segmentation process was carried out based on X-ray intensity to generate a 3D mesh model of the skull bone.

Mesh model generation for simulation and 3D printing: GeoMagic (3D Systems, Morrisville, NC) and GMSH software [188] were used to fix triangulation errors obtained from the initial reconstruction with Amira and to generate the solid finite element (FE) meshes.

3D printing of skull models and impact testing: The woodpecker skull models were printed out using a 3D printer (Object 350 connex3, Stratasys, Eden Prairie, MN). A VeroClear material (Young's modulus: 2 ~ 3 GPa, density: 1.20 ~ 1.30 g cm^{-3}, transparent material) was used to print the skull bone models. A custom-built drop weight test tower was used to simulate the impact of the beak and skull bones, a detail description of dimensions and specifications can be found in our previous work [104].

Dynamic finite element analysis (FEA): Dynamic FEA of an impact event between the woodpecker skull and a rigid solid plate was carried out on a commercially available software (Abaqus/Explicit). The skull was slightly rotated to align the main axis of the beak, calculated by finding the best fitting plane of symmetry, with the direction of pecking.

Frequency modal analysis: Frequency modal analyses of the two models were performed to identify the natural modes of vibration, and to evaluate the effects of the added mass and volume on the natural frequencies of the woodpecker skull due to the added overhang. Subsequently, dynamic impact cases with a Ricker Pulse input, along the direction of pecking at the tip of the beak, were simulated. The Ricker pulse produces an impact with a known spectrum, and results in a clearer acceleration profile of the structure in the frequency domain.

Chapter 5, in full, is a reprint of the material as it appears in Advanced Theory and Simulation. Jae-Young Jung, Andrei Pissarenko, Adwait Trikanad, David Restrepo, Frances Su, Andrew Marquez, Damian Gonzalez, Steven Naleway, Pablo Zavattieri, and Joanna McKittrick, 2019. The dissertation author was the primary investigator and author of this paper.

5.7 **Supporting Information**

5.7.1 **Some suggested evolutionized structural and skeletal features on woodpeckers**

In the manuscript, a few studies were introduced to illustrate other scientific efforts to better understand woodpecker's remarkable impact-resistance without brain injury. Here are more detailed examples to corroborate Burt's findings; Spring [195] also described pecking and climbing adaptations of woodpeckers are related to their food habits, and found that shorter legs in some woodpeckers would be advantageous for forceful and hard impact. An identical but extended rationale based on the concept of the relationship between the food habits and the pecking behavior among 61 different species of woodpeckers was adopted and thoroughly investigated by Kirby [184]. The author mainly compared the size of the rib bones, and reported that the pattern of increasing rib cage size ratios follows the one of the increasing skull specialization in the same species that were reported by Burt. In one genus of woodpeckers, *Melanerpes*, Leonard *et al*. [108] identified the relationship between morphology and foraging strategies along with their anatomical structure and divided them into two groups: the flycatchers (Red-headed, Acorn, and Lewis's woodpeckers) and the excavators (or a non-flycatcher, including Red-bellied, Gila, and Golden-fronted woodpeckers). The author specifically concluded that the inter-nasal width on the skull bone and the sites of muscle attachment were particularly distinct between these two groups: flycatchers showed wider intra-nasal distance and smaller muscle attachment sites, whereas excavators showed narrower intra-nasal distance and larger muscle attachment sites. The latest comparative analysis of cranial osteology of woodpeckers was performed by Donatelli [196], where seven distinct features on the skull bone in some woodpeckers (*Picus*) were identified, including the presence of a frontal overhang, when compared with other woodpeckers in the same family (*Pinici*). In general, it is considered that morphology and anatomical structures are affected by (or related to) the foraging behavior and the food source.

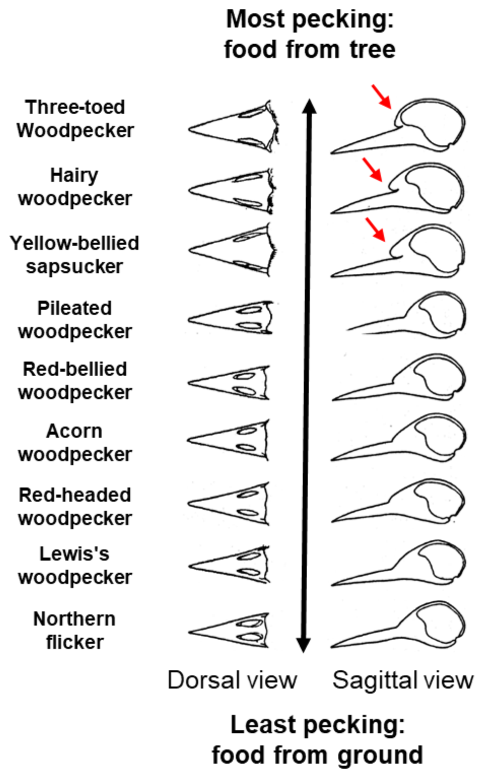

Figure 5.5. Nine different woodpeckers reported by Burt [182] and highlighted by Bock [54], showing different anatomical adaptation on the skull bone based on the relationship between food source and pecking behavior. Note that the upper most species, three-toed woodpecker, showed a portion of food in its stomach over 83% from tree larvae; while the lower most species, northern flicker, showed over 79% from ants and fruit. Red arrows indicate the frontal overhang structure.

5.7.2 **Previous studies of biomechanical analysis of the woodpecker's pecking**

Oda *et al*. [132] presented the first simplified two-dimensional finite element analysis (FEA), claiming that the structure of the skull bone combined with the hyoid bone plays a role as an impact-proof system to maintain low stress levels on the brain. Zhou *et al*. [117] reported the mechanical properties of the tongue of a gray-faced woodpecker (*Picus canus*) obtained from tensile tests to provide the first physical values from the real tissues. They found values of 1.28~3.72 GPa for the Young's modulus and 22~131 MPa for the tensile strength along three different locations over the whole hyoid apparatus. Wang *et al*. [119] compared pecking performances between a great-spotted woodpecker (*Dendrocopos major*) and a Eurasian hoopoe (*Upupa epops*) by observing pecking trajectories, quantifying skull bone quality via a bone morphometry analysis and finally three-dimensional (3D) FEA models. The effect of the beak lengths as well as the length difference between the upper beak and lower beak bone, and also the presence of the hyoid bone, were assessed in the aforementioned models. The authors mentioned an important point that the longer beak in the FE model would always carry the primary impact forces; even though the upper beak has a shorter beak bone than the lower beak, the total length of the upper beak becomes longer if one takes into account the surrounding tissues. This suggests that the longer upper beak would experience the primary impact force, rather than the lower beak. Yoon *et al*. [133] focused on the high acceleration/deceleration forces of a woodpecker's head during hammering and its corresponding effects on vibration. The authors represented the mechanical elements of the head using a mass-spring-damper model and subsequently developed a bio-inspired shock-absorbing packing system to protect micro-machined devices. They achieved very low failure rates (~1%) at 60,000 ***g***, while the commercially available hard-resin methods displayed a failure rate of 26%. This result was a quite impressive achievement attained by mimicking the woodpecker's anatomy. Zhu *et al*. [185] tried a whole body FEA and reported that the impact energy is mostly converted into strain energy and then transferred and dissipated in the body. In another study, the same authors also carried out nanoindentation mapping of a whole skull bone of a green woodpecker (the species was not specified) in the midsagittal-section as well as a frequency analysis by a FEA model [162], reporting that a large gap among the working, natural, and stress response frequencies prevent brain injury. The latest analysis of a woodpecker's head during pecking using FEA modeling was done by Liu *et al*. [116], where the effect of the hyoid bone and muscle as a constraining element on the cervical vertebra to limit the neck motion was concluded. Because of the complexity of structures in the head, with different materials and compositions, understanding the effect of each individual anatomical part on energy dissipation remains a challenge. In addition, by nature of bioexploration, which consists of observing a living animal's motions and habits, very limited experimental designs can be achieved using our bioinspiration design approach [197, 198]. Therefore, a simplified model with a single material, structure, and composition without making sacrificing or injuring any living animal can be a reasonable scientific approach to understand the impact-resistant mechanism of woodpeckers.

5.7.3 The effect of the frontal overhang on vibration from the impact testing

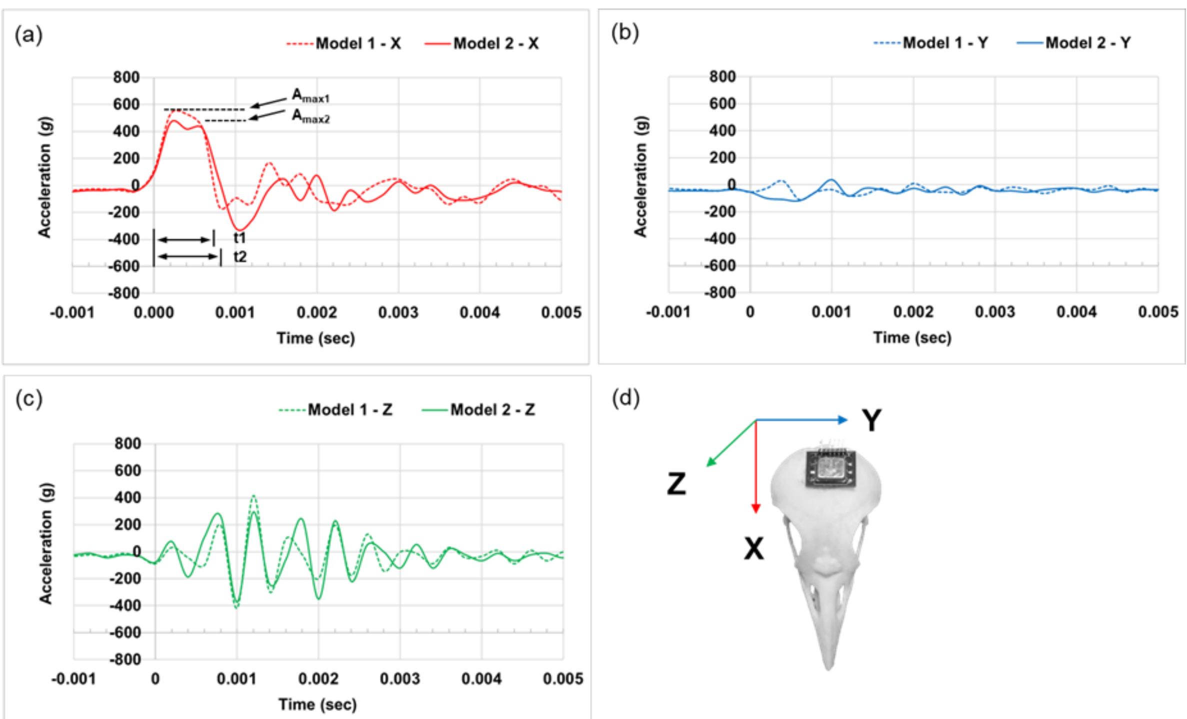

Figure 5.6. Measured acceleration on the skull bone near the brain in an impact speed of 3 m/s. (a) X-axis, (b) Y-axis, (c) Z-axis, and (d) indication of each direction with a photograph of accelerometer attached skull model. Note that the t_1 is the time duration of the first peak on the Model 1 (no overhang) and t_2 is on the Model 2 (with overhang).

Impact testing with the 3D printed woodpecker skull models was performed to obtain the accelerations of the skull bone near the brain using a drop-weight test tower as shown in Figure

5.6. Measured accelerations in all three axes of both skull models to investigate the effect of the frontal overhang structure on the vibration. Note that the main impact direction is along the X-axis as shown in Figure 5.6a and d. The first peak of measured acceleration over time in the X-axis on the Model 2 (overhang model) showed a relatively lower (max 464 g) and first drop around 0.814 ms (t_2), while the Model 1 (no overhang) showed a relatively higher peak acceleration (max 529 g) and a peak drop, which lasts until 0.729 ms (t_1). The impact duration of the Model 1 is shorter than the Model 2. In general, the differences in acceleration between the two models are not distinct: the patterns and values of peak accelerations are similar; therefore, the vibration is probably not affected by the presence of the frontal overhang structure.

5.7.4 A time-lapse high-speed camera analysis of impact testing and natural frequency calculation

A high-speed camera (Phantom V12, Vision Research Inc., Wayne, NJ) was used to get a set of high-frame rate time-step images up to 5,000 frames per second with a 200 μs of exposure time at a spatial resolution of 640*480. The deformation and vibrational motion of the 3D printed skull models at the moment of impact were recorded up to 3 seconds. The trigger for recording was manually operated. Deformation and displacement were recorded and analyzed only at the tip of the beak on the 3D printed skull models, due to the limited spatial resolution. ImageJ software was used to track the motion of the tip of the beak. The peak fitting was performed using Matlab software (The MathWorks, Inc., Natick, MA). With a single sine function, an average oscillation frequency of $f_{exp} = 629\ Hz$ was calculated. Assuming that this corresponds to a natural frequency of the 3D printed skull, associated with a sideways motion of the beak, the following scaling equation is introduced to compare this result with the natural modes of the real skull:

$$f_{skull} = f_{exp} \sqrt{\frac{E_{skull}}{E_{exp}} \frac{\rho_{exp}}{\rho_{skull}}} \sqrt{\frac{I_{skull}}{I_{exp}} \frac{A_{exp}}{A_{skull}} \left(\frac{L_{exp}}{L_{skull}}\right)^4} \tag{5.2}$$

Note that this equation is obtained from the definition of the natural frequency (Equation (5.1)), assuming that a simple analogy with a simple, homogenous solid can be made. By injecting all values of the material and geometric properties of the 3D printed skull and the real skull bones (see Table 5.1), we find that $f_{skull} = 4{,}263$ Hz, which we assimilate to the first natural mode of the skull (4,790 Hz), obtained for the computational model.

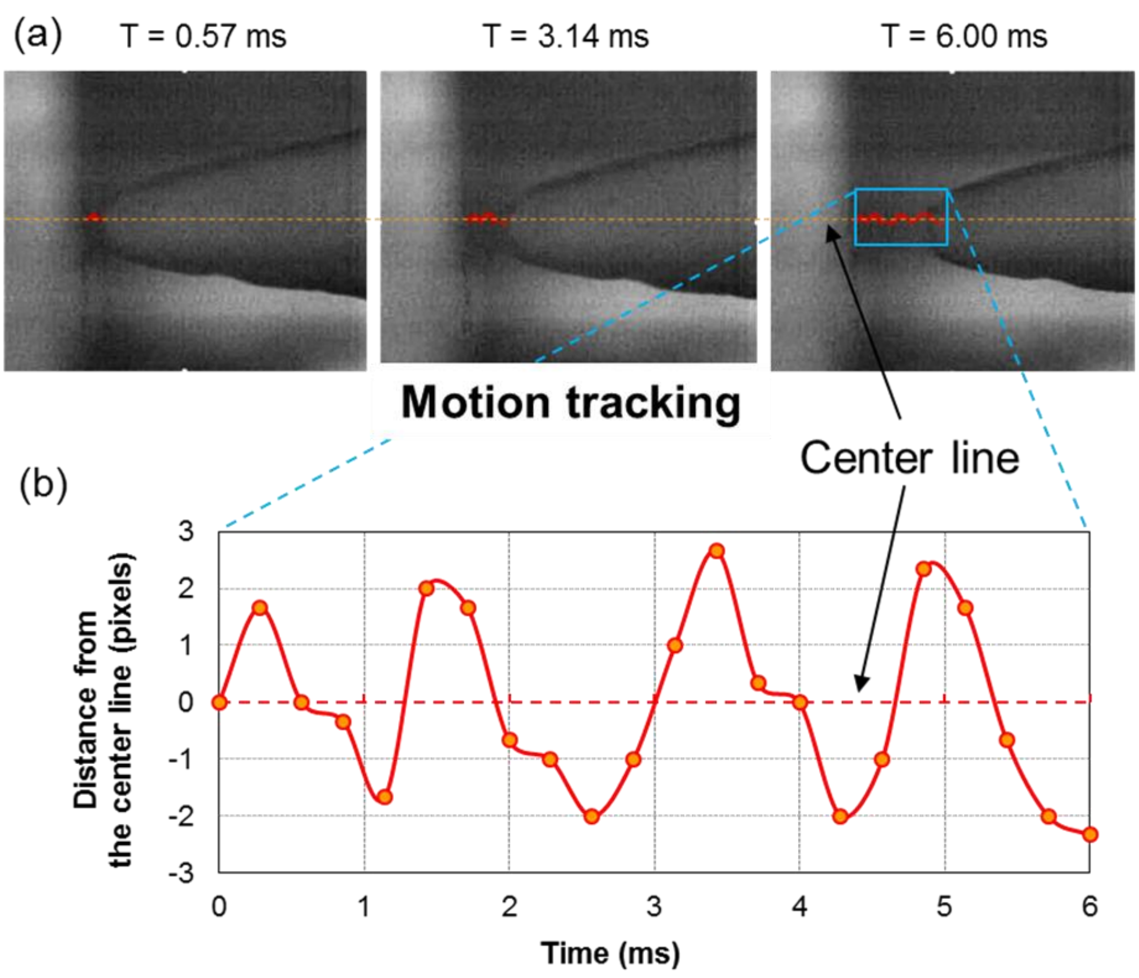

Figure 5.7. Motion tracking of the beak tip of a 3D printed skull model along the center line to find a pattern of vibration. (a) Time-lapse images captured with a high-speed camera at 0. 57 ms, 3.14 ms, and 6.00 ms, respectively. (b) A plot of the distance from the centerline of the 3D printed beak tip during impact up to 6 ms.

5.7.5 **The effect of the frontal overhang on von Mises stress and in-plane principal stress from the FEA simulation**

Figure 5.8 shows the effect of the frontal overhang between two skull models on the distributions of von Mises stress and in-plane principal stress over time through the FEA simulation. Interestingly, higher maximum stresses are mainly found on the Model 2 at node 1, 3, and 4 (through Figure 5.8a, c, d, e, g, and h); however, there is no noticeable difference at node 2 in both von Mises and in-plane principal stress (Figure 5.8b and f). A higher level of stress can be explained due to its higher mass from the added mass/volume as a form of the frontal overhang. However, the general trend found from other nodes (1,3, and 4) is not applied to node 2, no overhang model even shows a higher von Mises level and no difference of in-plane principal stress. This result could imply that the skull bone of woodpeckers is designed to be independent from the direct stress wave propagation because 1) the skull bone is far away from the beak tip, where the stress wave formed and started to propagated, and 2) the beak has enough structural components to dissipate main stress wave and to bypass the stress through the bottom of the head.

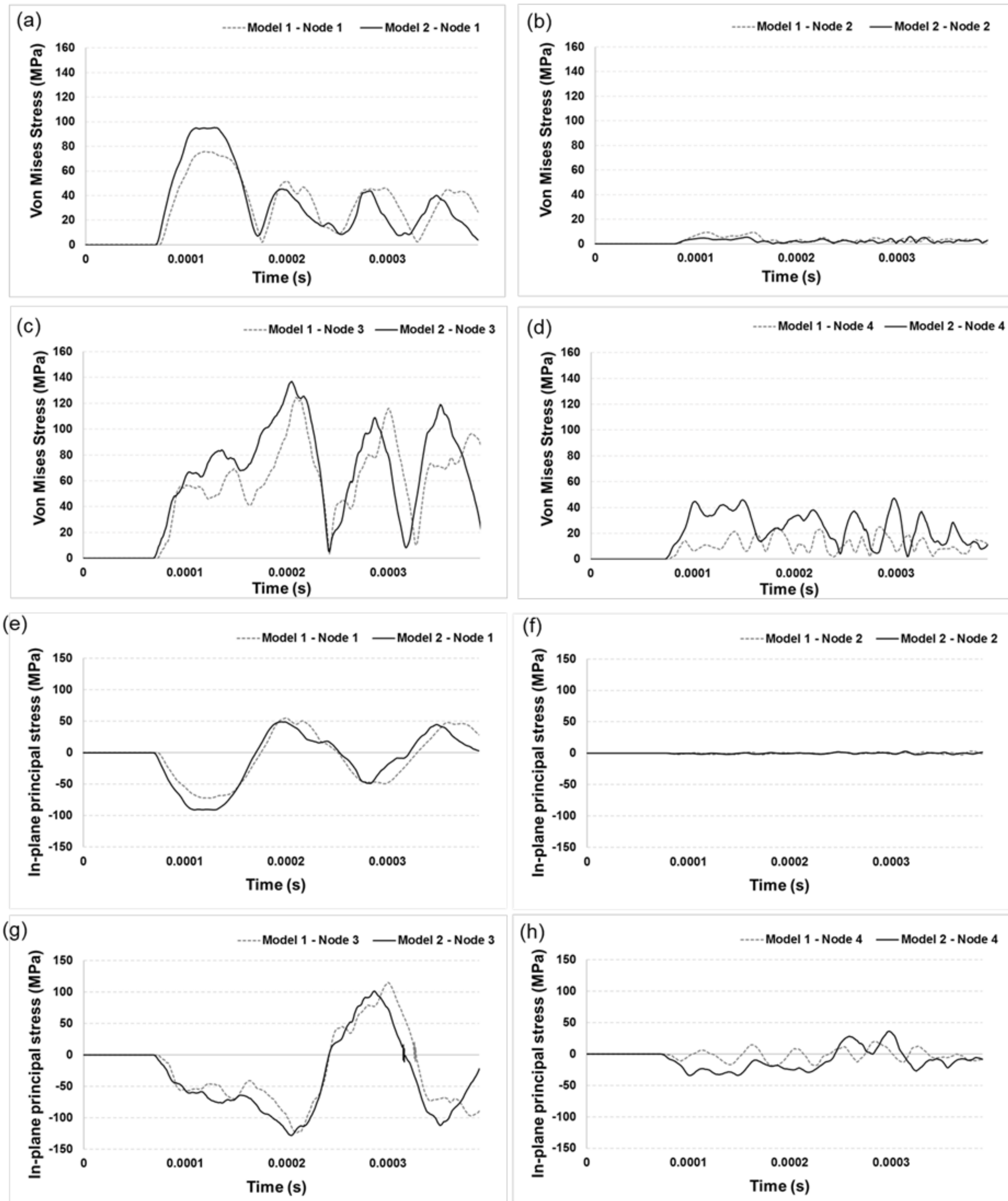

Figure 5.8. A comparison of the effect of the frontal overhang in two skull models. (a-d) von Mises stress levels over time. (e-h) In-plane principal stress over time at different locations of each model in an impact speed of 7 m/s. Model 1: No overhang model, Model 2: with overhang model. Note that node locations (1-4) are identical as in Figure 5.2c.

5.7.6 **Experimental materials and methods**

Micro-computed tomography (μ-CT): The scanning conditions are a rotation step of 0.7º, an exposure time of 1600 ms, a 100kV acceleration voltage, and an isotropic voxel size of 36.00 µm with the exception of the head that was scanned with an isotropic voxel size of 9.06 µm.
The images and three-dimensional reconstructed models were developed using the software programs CTvox and Dataviewer (Bruker microCT, Kontich, Belgium) and XMReconstructor (Xradia, Pleasanton, CA).

Mesh model generation for FE simulation and 3D printing: Triangle and tetrahedral mesh models of two woodpecker species were generated as following: first, the images obtained from the µ-CT scan were used to create a 3D triangulated surface shell (.stl file) using Amira. This shell representation of the woodpecker's skull was then treated using a GeoMagic (3D Systems, Morrisville, NC) in order to fix triangulation errors , self-intersections, highly creased edges, and undesired holes in the initial model. After obtaining a clean triangulated surface, we used GMSH software[19] to generate the solid FE meshes by filling the enclosed volumes with tetrahedral elements. Each mesh consists of approximately 250,000 linear tetrahedral elements.

Different skull models with artificial overhang: An artificial overhanging structure was added to the FEA model, at the interface between the upper beak bone and the frontal bone (anterior part of the skull bone), to mimic the structure of the frontal overhang. Specifically, using the Amira software, the artificial overhang was developed on top of the 3D model of the golden-fronted woodpecker and the acorn woodpecker, by comparing both the 3D model structure and 2D orthogonal images of a white-headed woodpecker model, which possesses this protrusion.

A drop weight test tower and impact testing: An impact speed of 3.8 m/s can be achieved at the maximum height of the tower as shown in Figure 5.2a. In addition, a customized guide

(Figure 5.2b) to hold and fix the angle of woodpecker skull models at the moment of impact was designed and used for the tests. To minimize physical friction between two steel guide rods and the 3D printed guide, the steel surface was lubricated. To present the worst-case scenario where there is no energy dissipation on the impact object (wood chips results from the pekcing activity of woodpeckers on trees disipates kinetic energy), an aluminum alloy metal plate was used in the experimental setup.

Measurement of accelerations: A triaxial ceramic piezoelectric accelerometer (Model 834M1-2000, TE connectivity Company, Hampton, VA, USA) was used to obtain the peak and average accelerations of the skull bone models over time during the impact testing. The dynamic measurement range and the maximum shock limit of the accelerometer were ± 2,000 ***g*** and 10,000 ***g***, respectively. The accelerometer was calibrated at an excitation voltage of DC 3.3 V and operated at the same condition. The dimensions of the assembled accelerometer are 25 × 20 × 12 mm. The weight of the original and assembled accelerometer with a printed circuit board were 2.6 g and 5.3 g, which represents less than 10% of the total weight of the 3D printed skulls (60.5 ~ 60.9 g). Therefore, the increased weight of the sensor on the skull models can be negligible. The accelerometer was attached on top of the parietal bone near the brain, so that the X-axis is parallel to the impact direction. The Y direction corresponds to a lateral motion (left and right along the impact direction) of the skull model, while the Z direction corresponds a dorsoventral motion (up and down motion along the impact direction). A 4-channel analog oscilloscope (DSO6014A, Agilent technologies, Colorado Springs, CO) was used to measure the accelerations in the X-, Y-, and Z-directions. The acceleration over time was plotted and presented, then, the spectra were converted using fast-Fourier transform (FFT) method to represent characteristic spectral patterns in a frequency vs. amplitude.

3D printed skull models for model validation: The size of the original 3D model was too small to perform any experimental test on it, thus, the 3D printed models were scaled up by a ratio of three to show better deformation and vibration, as well as to secure a large enough attachment site for the acceleration sensor, without generating a significant increase in total mass. The measured volume of the scaled up models were 42,160 mm^3 for the Model 1 (no overhang) and 42,636 mm^3 for the Model 2 (with overhang), respectively. In the printing process, a dissolvable support material (SUP706, Stratasys, Eden Prairie, MN) was used for an easy-removal and eventually removed by performing three washing steps, 1) physical scrubbing for the exterior and 2) submerging into 2% sodium hydroxide solution (NaOH) with 1% sodium metasilicate (Na_2SiO_3) as manufacturer indicated, and 3) finally shooting water-jet toward the surface and inside of the printed skull. After drying process for 24 hours at ambient temperature, the measured weight of the skull was 60.58 g for the Model 1 and 60.91 g for the Model 2, respectively. The increased weight for the Model 2 was 0.5% compared to the Model 1. From our preliminary tests, the tip of the beak can be easily broken because of the sharp shape and high compressive stress on the tip. To avoid this type of physical damage, and therefore undesired dissipation of energy, the tip of the beak was covered using a heat-shrinkable polylactic acid film (SPLI6-66, WestRock, Croydon, PA). In this case, better repeatability is achieved in terms of dynamic responses (i.e., vibration and acceleration). After covering the tip area with a cellophane tape, the models were store at 50℃ for 30 minutes until the film was fully contracted, and then, the tape was removed.

Table 5.1. Main variables for mechanical and materials properties, and finite element analysis parameters used in the dynamic impact simulation.

Parameter		Previous study	Present study			
			Experimental (3D printing)	FEM I	FEM II	FEM III
Material (or bone) density (kg m^{-3})		1,456 [116, 133]	1,200 ~ 1,300	1,250	1,456	
Poisson's ratio		0.3-0.4 [133, 185, 199]	0.33	0.33	0.33	
Young's modulus of the skull bone (GPa, scale to the woodpecker)		6-12 [162, 185]	2.0 ~ 3.0 (1:6)	2.5 (1:6)	15 (1:1)	
Young's modulus of the beak bone (GPa, scale to the woodpecker)		27-30 [110]	2.0 ~ 3.0 (1:6)	2.5 (1:6)	15 (1:1)	
A total volume of the whole skull (mm^3, the scale to the woodpecker)	No overhang - Model 1	-	42,160 (3:1)	42,160 (3:1)	1,561 (1:1)	
	Overhang - Model 2		42,636 (3:1)	42,636 (3:1)	1,579 (1:1)	
A total mass of the whole skull bone (g)	No overhang - Model 1	-	60.5	60.5	2.2	
	Overhang - Model 2		60.9	60.9	2.2	
Impact speed (m/s)		up to 7 [30]	3	3	3	7
Total impact energy (mJ)		-	274.5	274.5	10.1	55.1

Dynamic finite element analysis (FEA): Assigned mechanical properties – as well as other model parameters – are listed in Table 5.1. A first approximation was to consider the whole model as composed of one identical material with averaged values taken for bone density, Young's modulus and Poisson ratio. Although, in reality, these parameters vary in space, the idea here was mainly to observe the influence of structural elements rather than changes in material properties. An initial velocity of 3 m/s and 7 m/s is conferred to the skull and the contact between the skull and the plate is defined by a "hard" contact in the normal direction, and a frictionless tangential contact. It should also be noted that, in reality, the successful pecking of woodpeckers results in a large part from the fact that their kinetic energy is being dissipated by damaging the tree bark. As a result, lower stresses would be applied to the actual skull bone. However, the particular case of a skull impacting against an undeformable rigid plate is showcased here to highlight the skull resistance to extreme pecking conditions. Modeling an impact surface equivalent to a tree would introduce a lot of variability within the simulation. With a rigid plate, there is no or little influence on the plate geometry and the initial kinetic energy is only dissipated by friction, the rest being fully restituted to the skull. In this regard, many cases were actually observed where a woodpecker would peck at a metal pole without showing any sign of concussion while repeatedly pecking [133, 200]. Hence, a metal pole can be regarded as an undeformable rigid plate and our finite element analysis model defines this extreme case. Four representative nodes were selected as main regions of interests based on a preliminary data, as shown in Figure 5.2c. Each node is located at 1: the caudal end of the upper beak bone, 2: on the parietal bone near the brain, 3: on the palatine bone, and 4: on the jugal bone. Nodes 1 and 2 represent a dorsal line of stress wave propagation, while nodes 3 and 4 illustrate a ventral line of stress wave propagation. At each node, von Mises stress, in-plane principal stress, and acceleration will be obtained and compared in a dynamic impact condition.

Ricker's wavelet analysis: In the time domain, the wavelet is represented by a central peak with two smaller side lobes. The amplitude, $A(t)$, of a Ricker wavelet with peak frequency, f_M, at time t is given by:

$$A(t) = [1 - 2(\pi f_M t)^2] e^{-(\pi f_M t)^2} \tag{5.3}$$

The amplitude of the Ricker pulse was scaled to 0.01N and centered on a peak frequency of 4,790 Hz, which is in the general region of the first mode of natural vibration of each model. Simulations were run for up to 4 ms (4,000 μs) and the accelerations in X, Y and Z directions were recorded at nodes 1,2,3, and 4. The FFT was used to convert the time domain acceleration information obtained in each point into the frequency domain. This allows us to discern the dominant frequencies present at those points, and a comparison of two models (with and without the overhang) give us an idea of the effect of the frontal overhang on vibrational excitation or absorption at a certain frequency.

Scaling effect: The impact speed of 7 m/s of woodpecker's pecking is hard to archive in the laboratory setting because it requires falling height of 2.5 m regardless of the mass of object. Due to the limited height (maximum 55 cm including the skull length) of the impact tower, as shown in Figure 5.2a, only a maximum impact speed of 3.3 m/s can be achieved in our custom-built drop weight tower test, as described by the equations below:

$$Kinetic\ Energy\ (KE) = \frac{1}{2}mv^2 = mgh \tag{5.4}$$

$$v^2 = 2gh \tag{5.5}$$

$$v = \sqrt{2gh} \tag{5.6}$$

Where m is the mass of the falling object (kg), g is the gravitational acceleration (m s^{-2}), h is height (m), and v is the final velocity (m/s) at the moment of impact. Therefore, the drop height of the woodpecker skull samples from the tip of the beak to the impact plate was set to 0.46 m. Since we used scaled up models, with differences both in size and constituent materials, it is important to evaluate how the acceleration is affected by these changes. The equilibrium of a falling object of stiffness k (N/m), impacting a rigid surface at a velocity v, and deforming with a displacement x (m), can be expressed as follows:

$$ma = kx \tag{5.7}$$

Where a is the acceleration of the object (m/s^2). Conservation of energy at the moment of impact yields:

$$v = \sqrt{2ax} \tag{5.8}$$

By inserting Equation (5.8) into Equation (5.7):

$$a = v\sqrt{\frac{k}{2m}} \tag{5.9}$$

Assuming a simple homogenous solid with constant material properties, Equation (5.9) further develops into:

$$a = v\sqrt{\frac{EI}{2\rho A L^4}} \tag{5.10}$$

Where E is the Young's modulus (Pa), I is the second area moment of inertia (m^4), ρ is the material density (kg/m^3), A is the equivalent cross-sectional area (m^2), and L is the effective length (m). This equation further leads to a scaling law that is similar to Equation (5.2). Thus, for an impact speed of 7 m/s, we predicted a peak acceleration of 1,000 g. Assuming a similar impact speed for the real skull, and using the values provided in Table 5.1, we find that the acceleration of the real skull would reach ~6,800 g. For an impact duration of ~1 ms, this result approaches the limit of acceleration that is tolerable for woodpeckers, as predicted by Gibson [121].

CHAPTER 6: SUMMARY

6.1 Motivation and hypothesis

The main motivation of this entire thesis work is originated from two main scientific questions: 1) how woodpeckers avoid brain injury and 2) how the relationship between structure and property of the woodpecker head can be connected to the specific function (to be protective to the brain or impact-resistant). If these two questions can be fully answered in a scientific way, the results can lead to develop a practical protective device for human brain safety as well as a remarkable tool to deeply understand why many people get brain injury at a certain condition. This dissertation aims to provide great details to understand how woodpecker avoid brain injury. Main underlying hypotheses in this dissertation are:

- The woodpecker heads have evolved to protect the brain against the physical impact
- The hyoid bone of woodpeckers shows an unusual shape and function; it might add flexibility as well as energy absorbent capacity for impact-resistance on the head.
- The skull bone of woodpeckers has been specialized to absorb the impact-energy.
- If some woodpeckers need to peck more than other woodpeckers due to the food source, how this different pecking habit affects to the skull bone structure and what is the functional result of that change.

6.2 Summary

First of all, the objective of the first research paper on the hyoid bone in Chapter 3 is to specifically analyze the morphological and structural features and associated mechanical properties of the hyoid bones of acorn woodpeckers (*Melanerpes formicivorus*) to examine the structure/mechanical property relationships that allow it to avoid failure during the extreme conditions of pecking. The anatomical structure and compositional constituents of the hyoid apparatus was examined to determine its possible role in energy absorption. High-resolution micro-computed tomography and scanning electron microscopy with energy dispersive X-ray spectroscopy were performed and correlated with nanoindentation mapping. The hyoid apparatus has four distinct bone sections, with three joints between these sections. Nanoindentation results on cross-sectional regions of each bone reveal a previously unreported structure consisting of a stiff core and outer, more compliant shell with moduli of up to 27.4 GPa and 8.5 GPa, respectively. The bending resistance is low at the posterior section of the hyoid bones, indicating that this region has a high degree of flexibility to absorb impact. These new experimental results reveal possible energy dissipating features within the macro/micro structure of the hyoid bone. Therefore, it can be applied to further studies on the energy dissipation assessment of the woodpecker during drumming against trees and may have implications for the design of engineered impact-absorbing structures.

Second, the study introduced in Chapter 4 aims to examine the anatomical structure, composition, and mechanical properties of the skull to determine its potential role in energy absorption and dissipation. An acorn woodpecker and a domestic chicken are compared through micro-computed tomography to analyze and compare two- and three-dimensional bone morphometry. Optical and scanning electron microscopy with energy dispersive X-ray spectroscopy are used to identify the structural and chemical components. Nanoindentation reveals mechanical properties along the transverse cross-section, normal to the direction of impact. Results show two different strategies: the skull bone of the woodpecker shows a relatively small but uniform level of closed porosity, a higher degree of mineralization, and a higher cortical to skull bone ratio. Conversely, the chicken skull bone shows a wide range of both open and closed porosity (volume fraction), a lower degree of mineralization, and a lower cortical to skull bone ratio. This structural difference affects the mechanical properties: the skull bones of woodpeckers are slightly stiffer than those of chickens. Furthermore, the Young's modulus of the woodpecker frontal bone is significantly higher than that of the parietal bone. These new findings may be useful to potential engineered design applications, as well as future work to understand how woodpeckers avoid brain injury.

Lastly, the research works in Chapter 5 have performed based on the fact that the brain is one of the most important and complicated organs, but it is delicate and therefore needs to be protected from external forces. This makes the pecking behavior of the woodpecker so impressive, as they are not known to sustain any brain injury due to their anatomical adaptations. However, the relationship between the morphology of the woodpecker head and its mechanical function against damage from daily pecking habits remain an open question. Aided by recent technical advancements, these questions can be explored by applying new materials science concepts of bioinspiration and bioexploration to identify adapted structures/materials in a design that results from millions years of evolution. Two main features, including the beam-like bar structure of the jugal bone acting as a main stress deflector and the high natural frequency of the skull bone of woodpeckers can teach two lessons for potential materials development as well as engineering applications: protection of a delicate internal organ occurs by redirection of the main stress pathway and a large mismatch of the natural frequencies between the skull and brain avoids resonance and reduces the overall load experienced by the brain.

CHAPTER 7: BIOINSPIRED DESIGNS AND APPLICATIONS

Mimicking natural and biological materials for engineering applications has been a common strategy in recent years to develop and modify a different function, structure, and process using different materials [13, 201-207]. In some cases, some products can be found in the market as commercialized devices to mitigate impact energy to protect human and devices. Through this chapter, some examples of bioinspired design of impact-resistant biological materials inspired by the woodpecker head will be introduced.

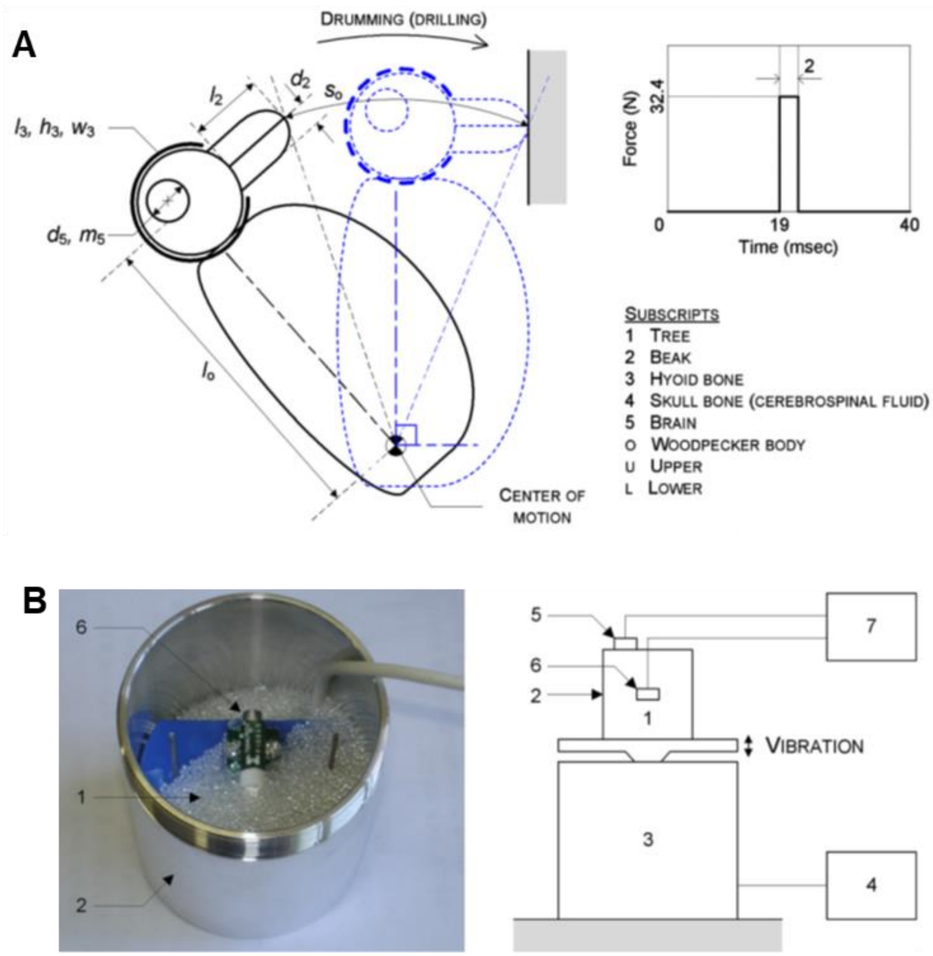

Figure 7.1. Examples of bioinspired design of the woodpecker head. (a) A simplified pecking motion of woodpeckers and (b) its empirical characterization of the sponge bone as a shock-absorbing device, adapted from [133]. Note that (1) microglasses, (2) aluminum enclosure, (3) vibration exciter, (4) power amplifier and signal generator, (5) reference accelerometer, (6) measurement accelerometer, (7) data recorder.

The first bioinspired design from the woodpecker heads was reported by Yoon et al. [133] to develop a high-shock-absorbing system for micromachined devices. The author analyzed the system of the woodpecker head as an individual component of a high-efficient shock-absorber as shown in Figure 7.1a. Using a mechanical vibration model by both kinematic model of the woodpecker's drumming motion and a mass-damper-spring model, a bioinspired shock-absorbing system was successfully performed a test at 60,000 g, showing only 0.7 % of failure rate, which is decreased from 26.4 % of a device by a conventional hard-resin method as shown in Figure 7.1b.

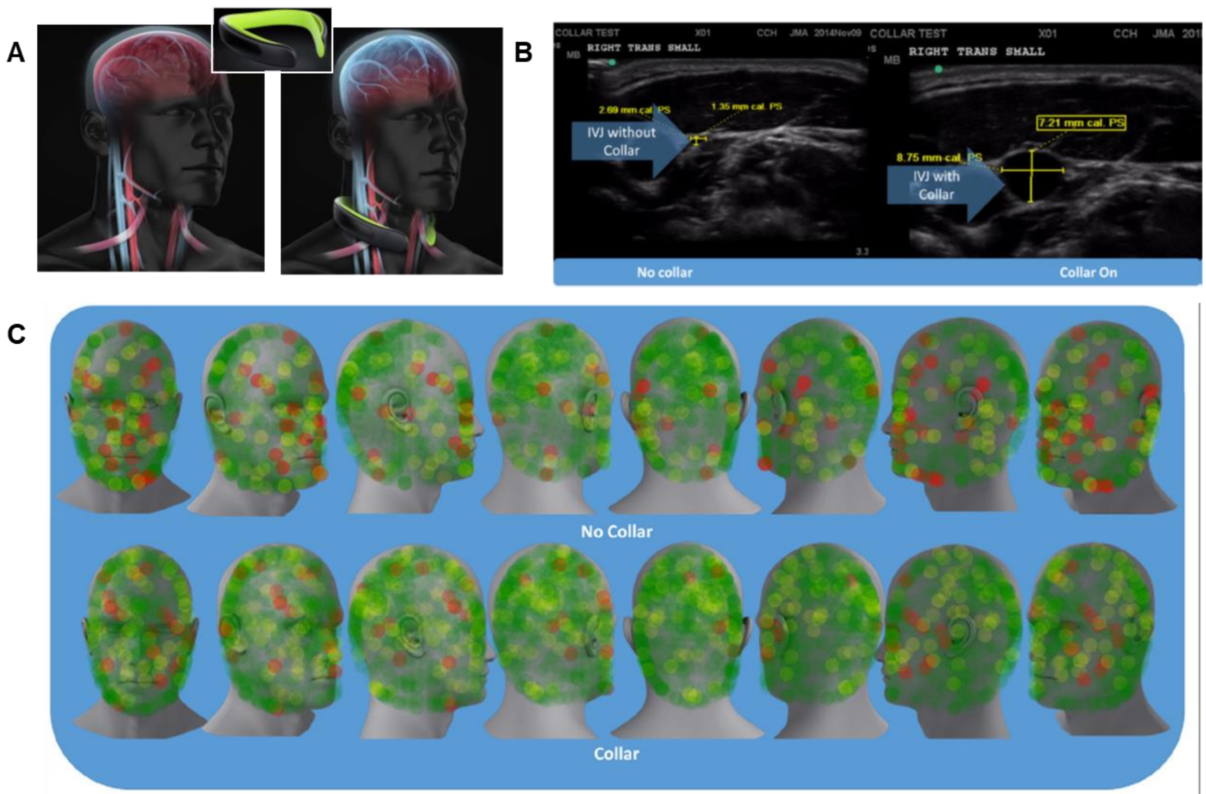

Figure 7.2. (a) A schematic representation of the jugular vein of human and its intracranial venous system with an image of the QC30 jugular vein compression device, adapted from [208]. (b) Ultrasonography images of the jugular vein without (left) and with collar (right), indicating that a significant increase in the internal jugular vein dilation after collar wearing trials, taken from [209]. (c) A representative scheme of the effect of the collar at different linear accelerations (above 20 *g* as green, 50 *g* as yellow, and 100 *g* as red) on the head impact, taken from [209].

Another example of bioinspired design of the head of woodpeckers is a jugular vein compression collar (Q30®, Q30 Innovations, LLC., Westport, CT) to prevent traumatic brain injury in the various contact sports (e.g., hockey, soccer, and football) followed by two clinical researches reported by Myer et al. [208, 209]. The author analyzed some brain injury biomarkers and head impacts of high school football and hockey players for a season, dividing into two groups as 1) a group with and 2) a group without the collar device (Figure 7.2a), reporting a significant drop of signs of brain trauma was observed. This technique is to make a bubble-wrap in the internal brain to press the jugular vein to increase the intercranial pressure as shown in Figure 7.2b. As a result, the device might restrict the motion or displacement of the whole brain at the moment of head impact (Figure 7.2c) [208, 209]. The technique and device are not directly relevant to the impact-resistant design of material/structure by absorbing impact energy but showed a potential benefit and design application of learning from the woodpecker head and its anatomical feature.

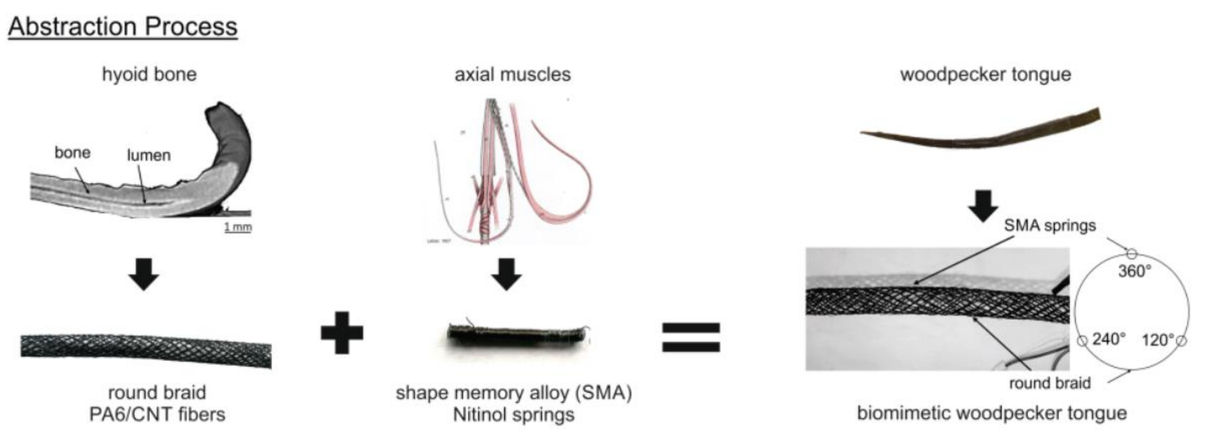

Figure 7.3. A schematic illustration of the design and development process of the woodpecker tongue inspired remote actuator made of shape memory alloy and carbon nanotube/polymer composite fibers, taken from [210].

Lastly, a light-weight biomimetic gripper inspired by a movement of the hyoid apparatus of woodpeckers was introduced by Esser et al. [210] by mimicking the muscle contraction movement to make a multi-directional bending motion as a remote actuator as shown in Figure 7.3. The author developed this actuator using a shape memory alloy and carbon nanotube/polymer composite fibers as a light-weight soft robot.

Overall, some interesting designs and devices were found inspired by the woodpecker head and its impact (and shock) absorbing ability; however, the detailed mechanisms and role of energy dissipation from individual part of the head of woodpeckers are still open questions because of its complexity.

CHAPTER 8: FUTURE DIRECTION

8.1 **As an impact-resistant material and structures**

The head of woodpeckers is a representative example of impact-resistant system and materials found in nature. However, the main difficulty of understanding its accurate energy dissipation mechanism is that they have some features as a sole but usually as a combination of two or three features (discussed through Chapter 1 and 2) among 1) multi-scale hierarchical structure from macro- to nano-scale, 2) multi-phase with a form of amorphous to crystalline, and 3) multi-property with a mechanical impedance mismatch. Again, because of its complexity, the comprehensive model needs to be further developed and investigated case-by-case, this is the main reason why the study of impact-resistant biological materials is relatively rare. This thesis work is the first step to understand impact-resistant biological materials/structures and there still are numerous considerations to combine those multi common features at each step. The combination of each component, for example, a multiscale structure with a multi-phase (i.e., the beak, skull, and hyoid bones of an acorn and red-bellied woodpecker) or a multi-scale structure with a multi-property (e.g, the gradient structure of the bone and rhamphotheca of the woodpecker beaks) is partially understood in some limited cases. Considering further details, we can find a more sophisticated and efficient structure and materials by combining the aforementioned three common features (multi-scale, multi-phase, and multi-properties) from impact-resistant biological materials found in nature. For example, the effect of the junction at the interface between the beak bone and rhamphotheca of the woodpeckers is still unknown. Moreover, the individual effect of the porous structure on the skull bone of woodpeckers is an ongoing topic in several research groups. Another example of the horns and hooves mentioned in Chapter 1, development of fiber composites with a helical and multi-scale structure can be a good example but it also needs further investigation until a commercialized product development. This will provide a better understanding of nature's ability to build a masterpiece of impact-resistant structures and materials, aiming to real life engineering products.

8.2 As a testing system on the brain injury to replace current animal injury models

Many people engaged in contact sports suffer from concussion, a type of mild TBI (mTBI), or more severely, chronic traumatic encephalopathy (CTE), which is a critical progressive degenerative disorder due to repeated exposures to mTBI [211]. Specifically, among deceased football players who donated their brains for research, a high proportion had neuropathological evidence of CTE, suggesting that CTE may be related to prior participation in football [212].

To date, many in-vitro and in-vivo TBI models have been developed; however, none has been able to fully replicate the injury event and provide a specific safety threshold limit. Woodpeckers are an interesting model organism, showing a specialized, repeated pecking habit, which imposes high deceleration forces on their head. They peck at trees every day throughout their 15-year life span; however, amazingly, no evidence has been found of chronic TBI or concussion in woodpeckers.

Thus, the brain of woodpeckers is interesting tissue to study and mimic but it never reported in scientific publications. The earlier investigations on the woodpecker's head have attempted by materials scientists and mechanical engineers to understand and identify a key element of the woodpecker's shock tolerance in terms of biomechanics of its beak and skull bone. Some anatomical features were found to be protective including the hyoid apparatus (wraps around the whole skull) [173], a keratinized beak sheath [110], and more porous and diverging skull bone structures [186]; although the woodpecker brain itself has never been comprehensively investigated.

Therefore, a cluster of related challenges as described below needs to be addressed:

1) Bird brain samples are limited and structural and mechanical characterization of the brain requires complicated interdisciplinary work. It necessitates collaboration among laboratories with widely different skills including neuroscience, molecular and biological engineering, biomedical imaging, mechanical and materials engineering.
2) Better understanding of brain injury mechanism in different animal species along its different structural and mechanical property is needed. The brain has a very complicated 3D multiscale hierarchical structure. The structural and mechanical properties vary on the species of animals, for example, the brains of birds and mammals are known to be different; therefore, the brain injury mechanisms could be different.
3) The brain is a porous, viscoelastic materials because of the complexity of the brain as a porous, viscoelastic materials, 3D modeling and finding a proper impact loading condition are extremely difficult for biologists. Comparative study of the brain among different animal species can highlight the similarities and differences of the brain, creating a novel structure-property relationship of the brains.

The bioinspiration process looks to take inspiration from the successful strategies of natural and biological materials and harness them to develop novel materials or structures that can provide a benefit to society. As the same approach, inspired by animal brains, the proposed study aims to enhance the understanding of mTBI mechanism by utilizing a novel convergent evolution model in birds and mammals. This is based on the hypothesis that the mechanisms of brain injury and its protection vary among different species; therefore, the study of structural and functional similarities and differences of the brain can give us a new insight for a common or distinct brain injury mechanism.

REFERENCES

[1] Espinosa HD, Juster AL, Latourte FJ, Loh OY, Gregoire D, Zavattieri PD. Tablet-level origin of toughening in abalone shells and translation to synthetic composite materials. Nature communications 2011;2:173.

[2] Finnemore A, Cunha P, Shean T, Vignolini S, Guldin S, Oyen M, Steiner U. Biomimetic layer-by-layer assembly of artificial nacre. Nature communications 2012;3:966.

[3] Wang J, Cheng Q, Tang Z. Layered nanocomposites inspired by the structure and mechanical properties of nacre. Chemical Society Reviews 2012;41:1111-29.

[4] McKittrick J, Chen PY, Tombolato L, Novitskaya EE, Trim MW, Hirata GA, Olevsky EA, Horstemeyer MF, Meyers MA. Energy absorbent natural materials and bioinspired design strategies: A review. Materials Science & Engineering C-Materials for Biological Applications 2010;30:331-42.

[5] Naleway SE, Porter MM, McKittrick J, Meyers MA. Structural design elements in biological materials: Application to bioinspiration. Advanced Materials 2015;27:5455-76.

[6] Tombolato L, Novitskaya EE, Chen P-Y, Sheppard FA, McKittrick J. Microstructure, elastic properties and deformation mechanisms of horn keratin. Acta Biomaterialia 2010;6:319-30.

[7] Chen P-Y, Schirer J, Simpson A, Nay R, Lin Y-S, Yang W, Lopez MI, Li J, Olevsky EA, Meyers MA. Predation versus protection: Fish teeth and scales evaluated by nanoindentation. Journal of Materials Research 2011;27:100-12.

[8] Naleway SE, Taylor JR, Porter MM, Meyers MA, McKittrick J. Structure and Mechanical Properties of Selected Protective Systems in Marine Organisms. Materials Science and Engineering: C 2016;59:1143-67.

[9] Yang W, Naleway SE, Porter MM, Meyers MA, McKittrick J. The armored carapace of the boxfish. Acta Biomaterialia 2015;23:1-10.

[10] Meyers MA. Dynamic Behavior Of Materials. Hoboken, NJ: John Wiley & Sons; 1994.

[11] Lee S, Novitskaya EE, Reynante B, Vasquez J, Urbaniak R, Takahashi T, Woolley E, Tombolato L, Chen PY, McKittrick J. Impact testing of structural biological materials. Materials Science & Engineering C-Materials for Biological Applications 2011;31:730-9.

[12] Ritchie RO, Koester KJ, Ionova S, Yao W, Lane NE, Ager JW, 3rd. Measurement of the toughness of bone: a tutorial with special reference to small animal studies. Bone 2008;43:798-812.

[13] Meyers MA, Chen PY. Biological Materials Science: Biological Materials, Bioinspired Materials, and Biomaterials: Cambridge University Press; 2014.

[14] Callister WD. Materials science and engineering-an introduction: John wiley & sons; 2007.

[15] Wegst UGK, Bai H, Saiz E, Tomsia AP, Ritchie RO. Bioinspired structural materials. Nature Materials 2015;14:23-36.

[16] Rossetto M, De Leo GA, Bevacqua D, Micheli F. Allometric scaling of mortality rates with body mass in abalones. Oecologia 2012;168:989-96.

[17] Wegst UG, Bai H, Saiz E, Tomsia AP, Ritchie RO. Bioinspired structural materials. Nature materials 2015;14:23.

[18] Wegst U, Ashby M. The mechanical efficiency of natural materials. Philosophical Magazine 2004;84:2167-86.

[19] Patek SN, Caldwell RL. Extreme impact and cavitation forces of a biological hammer: strike forces of the peacock mantis shrimp *Odontodactylus scyllarus*. Journal of Experimental Biology 2005;208:3655-64.

[20] Patek SN, Korff WL, Caldwell RL. Biomechanics: Deadly strike mechanism of a mantis shrimp. Nature 2004;428:819-20.

[21] Dubey P, Sharma N, Rathi A, Kumar A. Studies on Impact Behavior of Cortical Bone using Charpy Test and Finite Element Simulation. Proceedings of the World Congress on Engineering 2016;2.

[22] Chen P-Y, Stokes A, McKittrick J. Comparison of the structure and mechanical properties of bovine femur bone and antler of the North American elk (*Cervus elaphus canadensis*). Acta Biomaterialia 2009;5:693-706.

[23] Launey ME, Chen P-Y, McKittrick J, Ritchie R. Mechanistic aspects of the fracture toughness of elk antler bone. Acta Biomaterialia 2010;6:1505-14.

[24] Chen PY, Sheppard FA, Curiel JM, McKittrick J. Fracture mechanisms of bone: A comparative study between antler and bovine femur. MRS Proceedings 2011;1132:1132-Z01-04.

[25] Stokes AN, Hood JAA. Impact fracture characteristics of intact and crowned human central incisors. Journal of Oral Rehabilitation 1993;20:89-95.

[26] Bennett TD, Krajnovich DJ. Marangoni mechanism in pulsed laser texturing of magnetic disk substrates. Journal of Heat Transfer 1997;119:589-96.

[27] Kitchener A. An analysis of the forces of fighting of the blackbuck (*Antilope cervicapra*) and the bighorn sheep (*Ovis canadensis*) and the mechanical design of the horn of bovids. Journal of Zoology 1988;214:1-20.

[28] Warner SE, Pickering P, Panagiotopoulou O, Pfau T, Ren L, Hutchinson JR. Size-related changes in foot impact mechanics in hoofed mammals. PLoS ONE 2013;8:e54784.

[29] Bertram JEA, Gosline JM. Functional design of horse hoof keratin - the modulation of mechanical-properties through hydration effects. Journal of Experimental Biology 1987;130:121-36.

[30] May PA, Fuster JM, Haber J, Hirschman A. Woodpecker drilling behavior: An endorsement of the rotational theory of impact brain injury. Archives of Neurology 1979;36:370-3.

[31] Yaraghi NA, Guarín-Zapata N, Grunenfelder LK, Hintsala E, Bhowmick S, Hiller JM, Betts M, Principe EL, Jung J-Y, Sheppard L, Wuhrer R, McKittrick J, Zavattieri PD, Kisailus D. A sinusoidally architected helicoidal biocomposite. Advanced Materials 2016;28:6835-44.

[32] http://www.daveshowalter.com/photo/fighting-bighorn-rams/.

[33] http://www.threepullpa.com/520508-wild-horse-running.html.

[34] http://www.audubon.org/news/how-woodpecker-bangs-without-brain-damage.

[35] Crenshaw MA. Biomineralization Mechanisms. Skeletal Biomineralization: Patterns, Processes And Evolutionary Trends: American Geophysical Union; 2013. p. 1-9.

[36] Currey JD. Biomechanics of Mineralized Skeletons. Skeletal Biomineralization: Patterns, Processes and Evolutionary Trends: American Geophysical Union; 2013. p. 11-25.

[37] Feagin FF. Calcium, phosphate, and fluoride deposition on enamel surfaces. Calcified Tissue Research 1971;8:154-64.

[38] Osborn JF, Newesely H. The material science of calcium phosphate ceramics. Biomaterials 1980;1:108-11.

[39] Ma YR, Weiner S, Addadi L. Mineral deposition and crystal growth in the continuously forming teeth of sea urchins. Advanced Functional Materials 2007;17:2693-700.

[40] Killian CE, Metzler RA, Gong Y, Churchill TH, Olson IC, Trubetskoy V, Christensen MB, Fournelle JH, De Carlo F, Cohen S, Mahamid J, Scholl A, Young A, Doran A, Wilt FH, Coppersmith SN, Gilbert PUPA. Self-sharpening mechanism of the sea urchin tooth. Advanced Functional Materials 2011;21:682-90.

[41] Ma Y, Aichmayer B, Paris O, Fratzl P, Meibom A, Metzler RA, Politi Y, Addadi L, Gilbert PUPA, Weiner S. The grinding tip of the sea urchin tooth exhibits exquisite control over calcite crystal orientation and Mg distribution. Proceedings of the National Academy of Sciences 2009;106:6048-53.

[42] Shaw JA, Macey DJ, Brooker LR, Stockdale EJ, Saunders M, Clode PL. The chiton stylus canal: An element delivery pathway for tooth cusp biomineralization. Journal of Morphology 2009;270:588-600.

[43] de Obaldia EE, Jeong C, Grunenfelder LK, Kisailus D, Zavattieri P. Analysis of the mechanical response of biomimetic materials with highly oriented microstructures through 3D printing, mechanical testing and modeling. Journal of the Mechanical Behavior of Biomedical Materials 2015;48:70-85.

[44] Escobar de Obaldia E, Herrera S, Grunenfelder LK, Kisailus D, Zavattieri P. Competing mechanisms in the wear resistance behavior of biomineralized rod-like microstructures. Journal of the Mechanics and Physics of Solids 2016;96:511-34.

[45] Wang B, Yang W, McKittrick J, Meyers MA. Keratin: Structure, mechanical properties, occurrence in biological organisms, and efforts at bioinspiration. Progress in Materials Science 2016;76:229-318.

[46] Soons J, Herrel A, Genbrugge A, Adriaens D, Aerts P, Dirckx J. Multi-layered bird beaks: a finite-element approach towards the role of keratin in stress dissipation. Journal of the Royal Society Interface 2012;9:1787-96.

[47] Trim MW, Horstemeyer MF, Rhee H, El Kadiri H, Williams LN, Liao J, Walters KB, McKittrick J, Park SJ. The effects of water and microstructure on the mechanical properties of bighorn sheep (Ovis canadensis) horn keratin. Acta Biomaterialia 2011;7:1228-40.

[48] Johnson K, Trim M, Francis D, Whittington W, Miller J, Bennett C, Horstemeyer M. Moisture, anisotropy, stress state, and strain rate effects on bighorn sheep horn keratin mechanical properties. Acta Biomaterialia 2017;48:300-8.

[49] McKittrick J, Chen PY, Bodde SG, Yang W, Novitskaya EE, Meyers MA. The Structure, Functions, and Mechanical Properties of Keratin. JOM 2012;64:449-68.

[50] Weaver JC, Milliron GW, Miserez A, Evans-Lutterodt K, Herrera S, Gallana I, Mershon WJ, Swanson B, Zavattieri P, DiMasi E, Kisailus D. The stomatopod dactyl club: A formidable damage-tolerant biological hammer. Science 2012;336:1275-80.

[51] Gordon LM, Joester D. Nanoscale chemical tomography of buried organic–inorganic interfaces in the chiton tooth. Nature 2011;469:194.

[52] Sherman VR, Yang W, Meyers MA. The materials science of collagen. Journal of the Mechanical Behavior of Biomedical Materials 2015;52:22-50.

[53] Fratzl P. Collagen: Structure and Mechanics, an Introduction. In: Fratzl P, editor. Collagen: Structure and Mechanics. Boston, MA: Springer US; 2008. p. 1-13.

[54] Bock WJ. Functional and evolutionary morphology of woodpeckers. Ostrich 1999;70:23-31.

[55] Kitchener A. The effect of behaviour and body weight on the mechanical design of horns. Journal of Zoology 1985;205:191-203.

[56] Courtney M, Courtney A. Sheep collisions: The good, the bad, and the tbi. arXiv preprint arXiv:07113804 2007.

[57] Tombolato L, Novitskaya EE, Chen PY, Sheppard FA, McKittrick J. Microstructure, elastic properties and deformation mechanisms of horn keratin. Acta Biomaterialia 2010;6:319-30.

[58] Kasapi MA, Gosline JM. Micromechanics of the equine hoof wall: Optimizing crack control and material stiffness through modulation of the properties of keratin. Journal of Experimental Biology 1999;202:377-91.

[59] Wang B, Yang W, Sherman VR, Meyers MA. Pangolin armor: Overlapping, structure, and mechanical properties of the keratinous scales. Acta Biomaterialia 2016;41:60-74.

[60] Chon MJ, Daly M, Wang B, Xiao XH, Zaheri A, Meyers MA, Espinosa HD. Lamellae spatial distribution modulates fracture behavior and toughness of african pangolin scales. Journal of the mechanical behavior of biomedical materials 2017;76:30-7.

[61] Allen RD. Motility. The Journal of Cell Biology 1981;91:148s-55s.

[62] Kitchener A. Fracture toughness of horns and a reinterpretation of the horning behaviour of bovids. Journal of Zoology 1987;213:621-39.

[63] Lin AY-M, Meyers MA. Interfacial shear strength in abalone nacre. Journal of the Mechanical Behavior of Biomedical Materials 2009;2:607-12.

[64] Barthelat F, Li C-M, Comi C, Espinosa HD. Mechanical properties of nacre constituents and their impact on mechanical performance. Journal of Materials Research 2006;21:1977-86.

[65] Lin A, Meyers MA. Growth and structure in abalone shell. Materials Science and Engineering: A 2005;390:27-41.

[66] Song F, Zhang X, Bai Y. Microstructure and characteristics in the organic matrix layers of nacre. Journal of Materials Research 2002;17:1567-70.

[67] Wang R, Suo Z, Evans A, Yao N, Aksay I. Deformation mechanisms in nacre. Journal of Materials Research 2001;16:2485-93.

[68] Evans A, Suo Z, Wang R, Aksay I, He M, Hutchinson J. Model for the robust mechanical behavior of nacre. Journal of Materials Research 2001;16:2475-84.

[69] Meyers MA, McKittrick J, Chen P-Y. Structural Biological Materials: Critical Mechanics-Materials Connections. Science 2013;339:773-9.

[70] Weaver JC, Milliron GW, Miserez A, Evans-Lutterodt K, Herrera S, Gallana I, Mershon WJ, Swanson B, Zavattieri P, DiMasi E. The stomatopod dactyl club: a formidable damage-tolerant biological hammer. Science 2012;336:1275-80.

[71] Launey ME, Buehler MJ, Ritchie RO. On the mechanistic origins of toughness in bone. Annual review of materials research 2010;40:25-53.

[72] Nalla RK, Kinney J, Ritchie RO. Mechanistic fracture criteria for the failure of human cortical bone. Nature materials 2003;2:164.

[73] Koester KJ, Ager Iii J, Ritchie R. The true toughness of human cortical bone measured with realistically short cracks. Nature materials 2008;7:672.

[74] Nalla RK, Kruzic JJ, Kinney JH, Ritchie RO. Mechanistic aspects of fracture and R-curve behavior in human cortical bone. Biomaterials 2005;26:217-31.

[75] Nalla RK, Kruzic JJ, Kinney JH, Ritchie RO. Effect of aging on the toughness of human cortical bone: evaluation by R-curves. Bone 2004;35:1240-6.

[76] Wang X, Shen X, Li X, Agrawal CM. Age-related changes in the collagen network and toughness of bone. Bone 2002;31:1-7.

[77] Launey ME, Chen PY, McKittrick J, Ritchie RO. Mechanistic aspects of the fracture toughness of elk antler bone. Acta Biomaterialia 2010;6:1505-14.

[78] Adharapurapu RR, Jiang F, Vecchio KS. Dynamic fracture of bovine bone. Materials Science and Engineering: C 2006;26:1325-32.

[79] Kulin RM, Chen P-Y, Jiang F, Vecchio KS. A study of the dynamic compressive behavior of Elk antler. Materials Science and Engineering: C 2011;31:1030-41.

[80] Lawn BR, Lee JJ-W, Chai H. Teeth: Among nature's most durable biocomposites. Annual Review of Materials Research 2010;40:55-75.

[81] Meyers MA, Lin AYM, Lin YS, Olevsky EA, Georgalis S. The cutting edge: Sharp biological materials. JOM 2008;60:19-24.

[82] Imbeni V, Kruzic JJ, Marshall GW, Marshall SJ, Ritchie RO. The dentin-enamel junction and the fracture of human teeth. Nature Materials 2005;4:229-32.

[83] Lin CP, Douglas WH, Erlandsen SL. Scanning electron microscopy of type I collagen at the dentin-enamel junction of human teeth. Journal of Histochemistry & Cytochemistry 1993;41:381-8.

[84] Nalla RK, Kinney JH, Ritchie RO. Effect of orientation on the in vitro fracture toughness of dentin: the role of toughening mechanisms. Biomaterials 2003;24:3955-68.

[85] James KR, Haritos N, Ades PK. Mechanical stability of trees under dynamic loads. American Journal of Botany 2006;93:1522-30.

[86] Griffith MP, Withcer E. Palm stem shape correlates with hurricane tolerance, in a manner consistent with natural selection. Palms 2013;57:115-22.

[87] Reid SR, Peng C. Dynamic uniaxial crushing of wood. International Journal of Impact Engineering 1997;19:531-70.

[88] Gilbertson CG, Asce M, Bulleit WM. Load duration effects in wood at high strain rates. JOURNAL OF MATERIALS IN CIVIL ENGINEERING 2013;25:1647-55.

[89] Wood LW. Relation of strength of wood to duration of load. Forest Products Laboratory,Forest Service U S Department of Agriculture 1951;R1916:10.

[90] Leijten AJM. Impact crash and simulation of timber beams. Computational Engineering 2001;30:859-68.

[91] Tagarielli VL, Deshpande VS, Fleck NA, Chen C. A constitutive model for transversely isotropic foams, and its application to the indentation of balsa wood. International Journal of Mechanical Sciences 2005;47:666-86.

[92] Chen Y, Xu Z, Smith C, Sankar J. Recent advances on the development of magnesium alloys for biodegradable implants. Acta Biomaterialia 2014;10:4561-73.

[93] Wouts J, Haugou G, Oudjene M, Coutellier D, Morvan H. Strain rate effects on the compressive response of wood and energy absorption capabilities - Part A: Experimental investigations. Composite Structures 2016;149:315-28.

[94] Louisville Slugger bat. Glam Slam - Where Fashion Meets Sports; 2017.

[95] USS Constitution: The Legend Restored.

[96] Atirador. RPD-44 Russian light machine gun. 2008.

[97] Bowling alley flooring.

[98] Huang W, Zaheri A, Jung J-Y, Espinosa HD, Mckittrick J. Hierarchical structure and compressive deformation mechanisms of bighorn sheep (*Ovis canadensis*) horn. Acta Biomaterialia 2017;64:1-14.

[99] Aztec Warriors. Ancient Military; 2010.

[100] Arzt E. Biological and artificial attachment devices: Lessons for materials scientists from flies and geckos Materials Science and Engineering C 2006;26:1245-50.

[101] Shield of hoplon type. MFA for Educators; 2018.

[102] Trim MW, Horstemeyer M, Rhee H, El Kadiri H, Williams LN, Liao J, Walters KB, McKittrick J, Park S-J. The effects of water and microstructure on the mechanical properties of bighorn sheep (*Ovis canadensis*) horn keratin. Acta Biomaterialia 2011;7:1228-40.

[103] Fudge DS, Gardner KH, Forsyth VT, Riekel C, Gosline JM. The mechanical properties of hydrated intermediate filaments: Insights from hagfish slime threads. Biophysical Journal 2003;85:2015-27.

[104] Lee S, Novitskaya EE, Reynante B, Vasquez J, Urbaniak R, Takahashi T, Woolley E, Tombolato L, Chen PY, McKittrick J. Impact testing of structural biological materials. Materials Science and Engineering C: Materials for Biological Applications 2011;31:730-9.

[105] Hieronymus TL, Witmer LM, Ridgely RC. Structure of white rhinoceros (*Ceratotherium simum*) horn investigated by X‐ray computed tomography and histology with implications for growth and external form. Journal of Morphology 2006;267:1172-6.

[106] Zhang Q-b, Li C, Pan Y-t, Shan G-h, Cao P, He J, Lin Z-s, Ao N-j, Huang Y-x. Microstructure and mechanical properties of horns derived from three domestic bovines. Materials Science and Engineering: C 2013;33:5036-43.

[107] Kasapi MA, Gosline JM. Design complexity and fracture control in the equine hoof wall. Journal of Experimental Biology 1997;200:1639-59.

[108] Leonard DL, Heath JA. Foraging strategies are related to skull morphology and life history traits of Melanerpes woodpeckers. Journal of Ornithology 2010;151:771-7.

[109] Wang L, Niu X, Ni Y, Xu P, Liu X, Lu S, Zhang M, Fan Y. Effect of microstructure of spongy bone in different parts of woodpecker's skull on resistance to impact injury. Journal of Nanomaterials 2013;2013:17.

[110] Lee N, Horstemeyer MF, Rhee H, Nabors B, Liao J, Williams LN. Hierarchical multiscale structure-property relationships of the red-bellied woodpecker (*Melanerpes carolinus*) beak. Journal of the Royal Society Interface 2014;11:20140274.

[111] Seki Y, Bodde SG, Meyers MA. Toucan and hornbill beaks: A comparative study. Acta Materialia 2010;6:331-43.

[112] Seki Y, Schneider MS, Meyers MA. Structure and mechanical behavior of a toucan beak. Acta Materialia 2005;53:5281-96.

[113] Soons J, Herrel A, Aerts P, Dirckx J. Determination and validation of the elastic moduli of small and complex biological samples: bone and keratin in bird beaks. Journal of the Royal Society Interface 2012;9:1381-8.

[114] Wang L, Zhang H, Fan Y. Comparative study of the mechanical properties, micro-structure, and composition of the cranial and beak bones of the great spotted woodpecker and the lark bird. Science China Life Sciences 2011;54:1036-41.

[115] Lee N, Horstemeyer M, Prabhu R, Liao J, Rhee H, Hammi Y, Moser R, Williams L. The geometric effects of a woodpecker's hyoid apparatus for stress wave mitigation. Bioinspiration & Biomimetics 2016;11:066004.

[116] Liu Y, Qiu X, Zhang X, Yu TX. Response of woodpecker's head during pecking process simulated by material point method. PLoS ONE 2015;10:e0122677.

[117] Zhou P, Kong XQ, Wu CW, Chen Z. The novel mechanical property of tongue of a woodpecker. Journal of Bionic Engineering 2009;6:214-8.

[118] Rho J-Y, Kuhn-Spearing L, Zioupos P. Mechanical properties and the hierarchical structure of bone. Medical Engineering & Physics 1998;20:92-102.

[119] Wang L, Cheung JT-M, Pu F, Li D, Zhang M, Fan Y. Why do woodpeckers resist head impact injury: A biomechanical Investigation. PLoS ONE 2011;6:e26490.

[120] Emura S, Okumura T, Chen H. Scanning electron microscopic study of the tongue in the Japanese pygmy woodpecker (*Dendrocopos kizuki*). Okajimas Folia Anatomica Japonica 2009;86:31-5.

[121] Gibson LJ. Woodpecker pecking: how woodpeckers avoid brain injury. Journal of Zoology 2006;270:462-5.

[122] Imbeni V, Kruzic JJ, Marshall GW, Marshall SJ, Ritchie RO. The dentin-enamel junction and the fracture of human teeth. Nature Materials 2005;4:229-32.

[123] Wu CW, Zhu ZD, Zhang W. How woodpecker avoids brain injury? Journal of Physics: Conference Series 2015;628:012007.

[124] Livingston R. Some observations on the natural history of the tongue. Annals of the Royal College of Surgeons of England 1956;19:185.

[125] Homberger DG, Meyers RA. Morphology of the lingual apparatus of the domestic chicken, *Gallus gallus*, with special attention to the structure of the fasciae. American Journal of Anatomy 1989;186:217-57.

[126] Wallace RA. Aberrations in tongue structure of some malanerpine woodpeckers. Wilson Bulletin 1974;86:79-82.

[127] Homberger D. The lingual apparatus of the african grey parrot, *Psittacus erithacus* Linne (*Aves: Psittacidae*): Description and Theoretical Mechanical Analysis. The Wilson Bulletin 1987;99:738-40.

[128] Nag S, Banerjee R, Fraser HL. A novel combinatorial approach for understanding microstructural evolution and its relationship to mechanical properties in metallic biomaterials. Acta Biomaterialia 2007;3:369-76.

[129] May PA, Fuster J, Newman P, Hirschman A. Woodpeckers and head injury. The Lancet 1976;307:1347-8.

[130] Wang L, Fan Y. Role of mechanical performance of cranial bone in impact protection of woodpecker brain–a finite element study. World Congress on Medical Physics and Biomedical Engineering, IFMBE Proceedings 2013;39:165-7.

[131] Wang L, Lu S, Liu X, Niu X, Wang C, Ni Y, Zhao M, Feng C, Zhang M, Fan Y. Biomechanism of impact resistance in the woodpecker's head and its application. Science China Life Sciences 2013;56:715-9.

[132] Oda J, Sakamoto J, Sakano K. Mechanical evaluation of the skeletal structure and tissue of the woodpecker and its shock absorbing system. JSME International Journal Series A Solid Mechanics and Material Engineering 2006;49:390-6.

[133] Yoon S-H, Park S. A mechanical analysis of woodpecker drumming and its application to shock-absorbing systems. Bioinspiration & Biomimetics 2011;6:016003.

[134] Zhu ZD, Ma GJ, Wu CW, Chen Z. Numerical study of the impact response of woodpecker's head. AIP Advances 2012;2:042173.

[135] Mkukuma LD, Skakle JMS, Gibson IR, Imrie CT, Aspden RM, Hukins DWL. Effect of the proportion of organic material in bone on thermal decomposition of bone mineral: An investigation of a variety of bones from different species using thermogravimetric analysis coupled to mass spectrometry, high-temperature x-ray diffraction, and fourier transform infrared spectroscopy. Calcified tissue international 2004;75:321-8.

[136] Oliver WC, Pharr GM. An improved technique for determining hardness and elastic modulus using load and displacement sensing indentation experiments. Journal of Materials Research 1992;7:1564-83.

[137] Simmons G, Wang H. Single Crystal Elastic Constants And Calculated Aggregate Properties. Cambridge, MA: The MIT Press; 1971.

[138] Rho J-Y, Tsui TY, Pharr GM. Elastic properties of human cortical and trabecular lamellar bone measured by nanoindentation. Biomaterials 1997;18:1325-30.

[139] Hogg RV, Ledolter J. Engineering Statistics. New York, NY: Macmillan; 1987.

[140] Hochberg Y, Tamhane AC. Multiple Comparison Procedures. Hoboken, NJ: Wiley; 2009.

[141] Erdoğan S, Iwasaki S-I. Function-related morphological characteristics and specialized structures of the avian tongue. Annals of Anatomy-Anatomischer Anzeiger 2014;196:75-87.

[142] Rizzo D. Fundamentals of Anatomy And Physiology. Boston, MA: Cengage Learning; 2009.

[143] Fois G, Weimer M, Busch T, Felder ET, Oswald F, von Wichert G, Seufferlein T, Dietl P, Felder E. Effects of keratin phosphorylation on the mechanical properties of keratin filaments in living cells. The FASEB Journal 2013;27:1322-9.

[144] Socrates G. Biological Molecules - Macromolecules. Infrared and Raman Characteristic Group Frequencies: Tables and Charts. 3rd ed. Chichester, UK: John Wiley & Sons, Inc.; 2001.

[145] Seki Y, Kad B, Benson D, Meyers MA. The toucan beak: Sructure and mechanical response. Materials Science and Engineering: C 2006;26:1412-20.

[146] Ooi C, Hamdi M, Ramesh S. Properties of hydroxyapatite produced by annealing of bovine bone. Ceramics International 2007;33:1171-7.

[147] Pellegrino E, Biltz R. Mineralization in the chick embryo. Calcified Tissue Research 1972;10:128-35.

[148] Tzaphlidou M. Bone architecture: collagen structure and calcium/phosphorus maps. Journal of Biological Physics 2008;34:39-49.

[149] Shi D. Introduction to Biomaterials. Beijing, China: Tsinghua University Press; 2006.

[150] de Margerie E, Sanchez S, Cubo J, Castanet J. Torsional resistance as a principal component of the structural design of long bones: comparative multivariate evidence in birds. The Anatomical Record Part A: Discoveries in Molecular, Cellular, and Evolutionary Biology 2005;282:49-66.

[151] Novitskaya E, Vairo MSR, Kiang J, Meyers MA, McKittrick J. Reinforcing structures in avian wing bones. In: McKittrick JM, Narayan R, editors. Advances in Bioceramics and Biotechnologies II. Hoboken, NJ: John Wiley & Sons, Inc.; 2014. p. 47-56.

[152] Rho J-Y, Pharr GM. Effects of drying on the mechanical properties of bovine femur measured by nanoindentation. Journal of Materials Science: Materials in Medicine 1999;10:485-8.

[153] Bembey AK, Oyen ML, Bushby AJ, Boyde A. Viscoelastic properties of bone as a function of hydration state determined by nanoindentation. Philosophical Magazine 2006;86:5691-703.

[154] Boyde A. Scanning electron microscopy of bone. Bone Research Protocols: Springer; 2012. p. 365-400.

[155] Currey JD. The evolution of the mechanical properties of amniote bone. Journal of Biomechanics 1987;20:1035-44.

[156] Novitskaya E, Chen P-Y, Lee S, Castro-Ceseña A, Hirata G, Lubarda VA, McKittrick J. Anisotropy in the compressive mechanical properties of bovine cortical bone and the mineral and protein constituents. Acta Biomaterialia 2011;7:3170-7.

[157] Boresi AP, Schmidt RJ. Advanced Mechanics of Materials, 6th edition. Hoboken, NJ: John Wiley & Sons, Inc.; 2003.

[158] Askeland D, Wright W. The Science and Engineering of Materials. 7 ed. Boston, MA: Cengage Learning; 2015.

[159] Tang J, Wang Z, Mi Z, Yu Y. Finite element analysis of flat spiral spring on mechanical elastic energy storage technology. Research Journal of Applied Sciences, Engineering and Technology 2014;7:993-1000.

[160] Bock WJ, Miller WD. The scansorial foot of the woodpeckers, with comments on the evolution of perching and climbing feet in birds: American Museum of Natural History; 1959.

[161] Mehdizadeh SA, Neves DP, Tscharke M, Nääs IA, Banhazi TM. Image analysis method to evaluate beak and head motion of broiler chickens during feeding. Computers and Electronics in Agriculture 2015;114:88-95.

[162] Zhu Z, Wu C, Zhang W. Frequency analysis and anti-shock mechanism of woodpecker's head structure. Journal of Bionic Engineering 2014;11:282-7.

[163] Jollie MT. The head skeleton of the chicken and remarks on the anatomy of this region in other birds. Journal of Morphology 1957;100:389-436.

[164] Van Den Heuvel WF. Kinetics of the skull in the chicken (*gallus gallus domesticus*). Netherlands Journal of Zoology 1991;42:561-82.

[165] Khiem NT, Lien TV. A simplified method for natural frequency analysis of a multiple cracked beam. Journal of Sound and Vibration 2001;245:737-51.

[166] Tolman CW. The feeding behaviour of domestic chicks as a function of rate of pecking by a surrogate companion. Behaviour 1967;29:57-62.

[167] Van Den Heuvel WF, Berkhoudt H. Pecking in the chicken (*gallus gallus domesticus*): Motion analysis and stereotypy. Netherlands Journal of Zoology 1997;48:273-303.

[168] Marbury R. Taxidermy Art: A Rogue's Guide to the Work, the Culture, and How to Do It Yourself: Artisan; 2014.

[169] Doube M, Kłosowski MM, Arganda-Carreras I, Cordelières FP, Dougherty RP, Jackson JS, Schmid B, Hutchinson JR, Shefelbine SJ. BoneJ: Free and extensible bone image analysis in ImageJ. Bone 2010;47:1076-9.

[170] Bouxsein ML, Boyd SK, Christiansen BA, Guldberg RE, Jepsen KJ, Müller R. Guidelines for assessment of bone microstructure in rodents using micro–computed tomography. Journal of Bone and Mineral Research 2010;25:1468-86.

[171] Parfitt AM, Drezner MK, Glorieux FH, Kanis JA, Malluche H, Meunier PJ, Ott SM, Recker RR. Bone histomorphometry: Standardization of nomenclature, symbols, and units: Report of the asbmr histomorphometry nomenclature committee. Journal of Bone and Mineral Research 1987;2:595-610.

[172] Odgaard A, Gundersen HJG. Quantification of connectivity in cancellous bone, with special emphasis on 3-D reconstructions. Bone 1993;14:173-82.

[173] Jung J-Y, Naleway SE, Yaraghi NA, Herrera S, Sherman VR, Bushong EA, Ellisman MH, Kisailus D, McKittrick J. Structural analysis of the tongue and hyoid apparatus in a woodpecker. Acta Biomaterialia 2016;37:1-13.

[174] Bock WJ. Kinetics of the avian skull. Journal of Morphology 1964;114:1-41.

[175] Ritchie RO. The conflicts between strength and toughness. Nature Materials 2011;10:817-22.

[176] Gibson LJ, Ashby MF. Cellular solids: structure and properties: Cambridge university press; 1999.

[177] Ashby MF. The mechanical properties of cellular solids. Metallurgical Transactions A 1983;14:1755-69.

[178] Eliaz N, Metoki N. Calcium phosphate bioceramics: A review of their history, structure, properties, coating technologies and biomedical applications. Materials 2017;10:334.

[179] Bennett PM, Harvey PH. Brain size, development and metabolism in birds and mammals. Journal of Zoology 1985;207:491-509.

[180] National Center for Injury Prevention and Control. Report to congress on Mild Traumatic Brain injury in the United States: *Steps to prevent a serious public health problem*. Technical Report, Atlanta, GA: Centers for Disease Control and Prevention 2003.

[181] McKee AC, Cantu RC, Nowinski CJ, Hedley-Whyte ET, Gavett BE, Budson AE, Santini VE, Lee H-S, Kubilus CA, Stern RA. Chronic traumatic encephalopathy in athletes: Progressive tauopathy after repetitive head injury. Journal of Neuropathology & Experimental Neurology 2009;68:709-35.

[182] Burt WH. Adaptive modifications in the woodpeckers: University of California Press; 1930.

[183] Beal FEL. Food of the woodpeckers of the United States: US Dept. of Agriculture, Biological Survey; 1911.

[184] Virginia CK. An adaptive modification in the ribs of woodpeckers and piculets (*picidae*). The Auk 1980;97:521-32.

[185] Zhu Z, Zhang W, Wu C. Energy conversion in woodpecker on successive peckings and its role on anti-shock protection of brain. Science China Technological Sciences 2014;57:1269-75.

[186] Jung J-Y, Pissarenko A, Yaraghi N, Naleway S, Kisailus D, Meyers M, McKittrick J. A comparative analysis of the avian skull: Woodpeckers and chickens. Journal of the Mechanical Behavior of Biomedical Materials 2018;84:273-80.

[187] Smith KK. The Skull. In: Hanken J, Hall BK, editors. The skull. Chicago and London: University of Chicago Press; 1993. p. 150-96.

[188] Geuzaine C, Remacle J-F. Gmsh: A 3-D finite element mesh generator with built-in pre- and post-processing facilities. International Journal for Numerical Methods in Engineering 2009;79:1309-31.

[189] Bock WJ. Functional and evolutionary explanations in morphology. Netherlands Journal of Zoology 1999;49:45-65.

[190] Ryan H. Ricker, Ormsby, Klauder, Butterworth — A choice of wavelets. CEEG Recorder 1994;19:8-9.

[191] Restrepo DA. Programmable cellular materials: Purdue University; 2015.

[192] Wang Y. The Ricker wavelet and the Lambert W function. Geophysical Journal International 2015;200:111-5.

[193] Laksari K, Wu LC, Kurt M, Kuo C, Camarillo DC. Resonance of human brain under head acceleration. Journal of the Royal Society Interface 2015;12:20150331.

[194] Hirsch AE, Ommaya AK, Mahone RM. Tolerance of subhuman primate brain to cerebral concussion: Naval Ship Research and Development Center; 1968.

[195] Spring LW. Climbing and pecking adaptations in some north american woodpeckers. The Condor 1965;67:457-88.

[196] Donatelli RJ. Cranial osteology of Picini (*Aves: Piciformes: Picidae*). Acta Zoologica 2014;95:155-65.

[197] Porter MM, Adriaens D, Hatton RL, Meyers MA, McKittrick J. Why the seahorse tail is square. Science 2015;349:aaa6683.

[198] Frank MB, Naleway SE, Wirth TS, Jung J-Y, Cheung CL, Loera FB, Medina S, Sato KN, Taylor JRA, McKittrick J. A protocol for bioinspired design: A ground sampler based on sea urchin jaws. Journal of Visualized Experiments 2016:e53554.

[199] Liu H, Jiang S, Chen Z, Gan Y, Chang J, Wang Y, Tong Z. Simulation of hard-soft material interaction under impact loading employing the material point method. Science China Technological Sciences 2015;58:763-8.

[200] Slatin T. Video clip: Confused Woodpecker.

[201] Gu GX, Takaffoli M, Hsieh AJ, Buehler MJ. Biomimetic additive manufactured polymer composites for improved impact resistance. Extreme Mechanics Letters 2016;9:317-23.

[202] Deville S, Saiz E, Nalla RK, Tomsia AP. Freezing as a path to build complex composites. Science 2006;311:515-8.

[203] Deville S, Saiz E, Tomsia AP. Freeze casting of hydroxyapatite scaffolds for bone tissue engineering. Biomaterials 2006;27:5480-9.

[204] Fu Q, Rahaman MN, Dogan F, Bal BS. Freeze-cast hydroxyapatite scaffolds for bone tissue engineering applications. Biomedical Materials 2008;3:025005.

[205] Porter MM, Yeh M, Strawson J, Goehring T, Lujan S, Siripasopsotorn P, Meyers MA, McKittrick J. Magnetic freeze casting inspred by nature. Materials Science and Engineering A 2012;556:741-50.

[206] Porter MM, Imperio R, Wen M, Meyers MA, McKittrick J. Bioinspired scaffolds with varying pore architectures and mechanical properties. Advanced Functional Materials 2014;24:1978-87.

[207] Kamps T, Gralow M, Schlick G, Reinhart G. Systematic biomimetic part design for additive manufacturing. Procedia CIRP 2017;65:259-66.

[208] Myer GD, Yuan W, Barber Foss KD, Thomas S, Smith D, Leach J, Kiefer AW, Dicesare C, Adams J, Gubanich PJ, Kitchen K, Schneider DK, Braswell D, Krueger D, Altaye M. Analysis of head impact exposure and brain microstructure response in a season-long application of a jugular vein compression collar: a prospective, neuroimaging investigation in American football. British Journal of Sports Medicine 2016;50:1276-85.

[209] Myer GD, Yuan W, Barber Foss KD, Smith D, Altaye M, Reches A, Leach J, Kiefer AW, Khoury JC, Weiss M, Thomas S, Dicesare C, Adams J, Gubanich PJ, Geva A, Clark JF, Meehan WP, Mihalik JP, Krueger D. The Effects of External Jugular Compression Applied during Head Impact Exposure on Longitudinal Changes in Brain Neuroanatomical and Neurophysiological Biomarkers: A Preliminary Investigation. Frontiers in Neurology 2016;7:74.

[210] Esser F, Krieger H, Jandrey S, Scholz I, Gries T. The biomimetic woodpecker tongue : a fiber-based, lightweight biomimetic soft robot. Bionik: Patente aus der Natur. Bremen, Germany 2015. p. 198-203.

[211] McKee CT, Walz JY. Effects of added clay on the properties of freeze-casted composites of silica nanoparticles. Journal of the American Ceramic Society 2009;92:916-21.

[212] Mez J, Daneshvar DH, Kiernan PT, Abdolmohammadi B, Alvarez VE, Huber BR, Alosco ML, Solomon TM, Nowinski CJ, McHale L, Cormier KA. Clinicopathological evaluation of chronic traumatic encephalopathy in players of american football. Journal of the American Medical Association 2017;318:360-70.